POSIVA

SKB

Embedded oxide particles in Friction Stir Welds

Effect on creep and corrosion properties

Matts Björck

Claes Taxén

Taina Vuoristo

Ragna Elger

Tommy Zavalis

Leyla Wikström

Mari Sparr

Embedded oxide particles in Friction Stir Welds

Effect on creep and corrosion properties

Matts Björck, Svensk Kärnbränslehantering AB

Claes Taxén, Taina Vuoristo, Ragna Elger, Tommy Zavalis, Leyla Wikström, Mari Sparr

Swerea KIMAB

The original report, dated April 2019, was found to contain editorial errors which have been corrected in this updated version.

Abstract

Friction Stir Welding (FSW) is the selected reference method for sealing the copper canister in the KBS-3 method. If the weld is conducted in the presence of oxygen copper oxide will form on the joint surface and become embedded in the weld. Dispersed copper oxide in the welds could have negative effects on the performance of the canister as a barrier. The identified affected properties are the corrosion resistance and creep ductility.

Weld material with varying thickness of copper oxide are manufactured by oxidization of joint line segments in a laboratory oven. The thickness is controlled by varying the exposure time and temperature. The final oxide thickness is measured by using a combination of Glow Discharge Optical Emission Spectroscopy (GD-OES) and Scanning Electron Microscopy (SEM). An oxide thickness range of 0 to 8 µm was achieved.

The segments were assembled to a full ring which was welded to a lid under an argon gas atmosphere in order to not produce additional oxide thickness. The weld was cut into sections for metallographic investigations to reveal the line of oxide particles. The metallographic investigations revealed visible lines of oxides for a nominal thickness of 1 µm and above. For a nominal thickness of 0.1 µm and below no oxide line could be detected.

Tensile and creep specimens were extracted perpendicular to the oxide particle line. The test specimens were fabricated with a gauge length of 4 mm in order to measure a local response from the area around the oxide particles. Tensile tests were conducted at 75 and 175 °C, creep testing at 75 °C. All tensile and creep tests showed that for an oxide thickness of below 0.1 µm the ductility was similar to the reference material (non-welded). For samples with oxide thickness above 1 µm the ductility was reduced and oxide particles could be detected on the fracture surfaces.

The presence of oxide particles in the metal could conceivably affect the corrosion behavior of the metal. Electrochemical studies of metallic copper from the weld do not reveal any significant differences from the parent material taken from the lid of a welded object. The apparent nobility of copper is not significantly different from that of the parent material. When forced to corrode to an average depth of 0.1 mm, the morphology of the surfaces from the weld is also similar to that of the parent material.

Chemical dissolution of oxide, as copper oxide (Cu_2O), could be relatively fast provided that there is liquid water in contact with the canister. High chloride concentrations and high carbonate concentrations in the water increase the rate of dissolution. The worst case studied here, 1.0 M chloride, 10 mM carbonate at pH 7.0 with a wedge shaped continuous oxide band could perforate a 5 cm thick weld in little more than 1 000 years.

The report also discusses how the present FSW process can achieve welds that do not show any negative consequences of oxide particles based on the findings in this work.

Sammanfattning

Friktionsomrörningssvetsning (FSW, eng. Friction Stir Welding) är den valda referensmetoden för att försluta kopparkapseln i KBS-3 metoden. Om svetsningen sker i en miljö som innehåller syre kommer kopparoxid att bildas på fogytorna och följaktligen bli inbäddat i svetsen. Dessa fragmenterade kopparoxider kan vara skadliga för kopparkapselns barriärfunktion i slutförvaret. Korrosionsmotståndet och krypduktiliteten har identifierats som egenskaper som kan påverkas av dessa oxider.

Svetsat material med varierande kopparoxidtjocklek på fogytorna tillverkades genom att segment av foglinjen oxiderades i en laboratorieugn. Genom att använda en teoretisk modell fastställdes recept (tid och temperatur) för att erhålla olika oxidtjocklekar i intervallet 0 till 8 µm. Den slutgiltiga oxidtjockleken uppmättes med GD-OES (eng. of Glow Discharge Optical Emission Spectroscopy) och SEM (Svepelektronmikroskopi).

Segmenten monterades ihop till en full ring och svetsades samman med ett lock under en argon atmosfär för att inte ytterligare kopparoxid skulle bildas på ytorna. Metallografiska prov skars ut från varje segment för att undersöka förekomst av inbäddade oxider. Detta visar att synliga stråk bildades för nominella oxid tjocklekar på 1 µm och över. För nominella tjocklekar lika med och under 0,1 µm detekterades inga oxidstråk.

Drag- och krypprovstavar togs ut vinkelrätt mot oxidstråken. Provstavarna tillverkades med en mätlängd på 4 mm för att mäta den lokala responsen från området med oxidstråk. Dragprov utfördes vid 75 och 175 °C och krypprovning vid 75 °C. Alla prov för en oxid tjocklek 0,1 µm eller mindre uppvisade samma egenskaper som referensmaterial (icke svetsat material). Prov med en oxidtjocklek 1 µm eller tjockare hade en lägre duktilitet. Dessa prov uppvisade även oxidpartiklar på brottytorna.

Oxidpartiklar i metaller skulle också kunna påverka korrosionsegenskaperna hos metallen. Elektrokemiska studier av koppar av, ovan angivna, svetsat material uppvisar inga signifikanta skillnader från basmaterial taget från locket av det svetsade objektet. När proven tvingas att korrodera till ett medeldjup av 0,1 mm är också morfologin på ytorna samma som basmaterialet.

Kemisk upplösning av oxid, såsom Cu_2O, kan vara en relativt snabb process givet att vatten finns i kontakt med kapseln. Höga kloridhalter och höga karbonathalter i vattnet ökar upplösningshastigheten. Det värsta fallet studerat här, 1,0 M klorid, 10mM karbonat vid pH 7,0 med ett kilformat kontinuerligt oxidband med en tjocklek på 5 cm skulle kunna upplösas inom lite mer än 1 000 år.

Rapporten diskuterar också dessa resultats påverkan på den nuvarande svetsprocessen för att erhålla svetsar som inte uppvisar negativa effekter av oxider.

Tiivistelmä

Kitkatappihitsaus (FSW) on valittu kuparisen loppusijoituskapselin referenssimentelmäksi KBS-3 loppusijoituskonseptissa. Jos hitsaus tehdään olosuhteissa, joissa on happea, kuparioksidia muodostuu hitsin liitospintoihin ja oksidit hautautuvat hitsiin. Hitsissä olevat kuparioksidi dispersiot voivat vaikuttaa haitallisesti kapselin toimintaan päästöesteenä loppusijoituslaitoksessa. On tunnistettu, että tämä vaikuttaa korroosion kestoon ja virumissitkeyteen.

Hitsimateriaalin railopinnalle valmistettiin laboratorio uunissa segmenteittäin eri vahvuisia kuparioksidi kerroksia. Oksidin vahvuus kontrolloitiin lämpökäsittelyajalla ja lämpötilalla, jotka määriteltiin laskemalla etukäteen. Lopullinen oksidikerroksen vahvuus mitattiin GD-OES spektroskopialla (eng. Glow Discharge Optical Emission Spectroscopy) ja pyyhkäisyelektronimikroskopilla. Oksidikerroksien vahvuudet olivat $0-8$ µm.

Segmentit asennettiin kokonaisen renkaan päälle ja hitsattiin yhteen argon kaasussa siten että oksidikerrokset eivät enää kasvaneet. Hitsi paloiteltiin osiin metallurgisia tutkimuksia varten, joissa selvitettiin oksidipartikkeliviivat hitsistä. Metallurgisten tutkimusten perusteella oksidiviivat on havaittavissa kun oksidikerros on vahvempi kuin 1 µm. Alle 0,1 µm oksidivahvuuksilla ei oksidiviivoja pystytty havaitsemaan.

Veto ja virumisnäytteet irrotettiin oksidipartikkeliviivoja vastaan kohtisuorassa. Testinäytteet valmistettiin 4 mm mittapituudella, jotta voitaisi määrittää oksidipartikkelien vaikutus paikallisesti oksidipartikkelien ympäristöstä. Vetokokeet tehtiin 75 ja 175 °C, sekä virumiskokeet 75 °C lämpötiloissa. Kaikissa veto- ja virumiskokeissa sitkeys oli samalla tasolla kuin hitsaamattoman referenssimateriaalin kun oksidin vahvuus oli alle 0,1 µm. Koekappaleissa, joissa oksidivahvuus oli yli 1 µm, sitkeys oli alentunut ja oksideja havaittiin murtopinnassa.

Oksidit metallissa voi mahdollisesti vaikuttaa metallin korroosiokäyttäytymiseen. Kuparihitsin sähkökemialliset selvitykset eivät ole tuoneet esille mitään merkittäviä eroja hitsatun kannen perusaineen ja hitsimateriaalin välillä. Hitsimateriaalin jalous ei poikkea merkittävästi hitsattavan perusaineen jaloudesta. Korrosiokokeissa, joissa kupari on pakotettu korrodoitumaan keskimääräisesti 0,1 mm, hitsin pinnan morfologia vastaa perusaineen morfologiaa.

Oksidin kemiallinen liukeneminen, kuten Cu_2O:n, voi olla suhteellisen nopeaa edellyttäen että neste-mäinen vesi on kontaktissa kapselin kanssa. Korkea kloridipitoisuus ja korkea karbonaattipitoisuus vedessä lisää liukenemisnopeutta. Tässä tutkimuksessa käytetyssä pahimmassa tapauksessa, jossa kloridi pitoisuus oli 1,0 M ja karbonaattipitoisuus 10 mM happamuuden ollessa 7,0 pH, kiilanmuotoinen jatkuva oksidilinja voi syöpyä 50 mm vahvan hitsin läpi hieman yli tuhannessa vuodessa.

Raportissa käsitellään myös seurauksia nykyisen hitsausprosessin kaasusuojauksen happitasosta ja muodostuvien oksidien haitallisten ilmiöiden välttämisestä.

Contents

1 Introduction

Friction Stir Welding (FSW) is the reference method for sealing the copper canister in SKB's and Posiva's implementation of the KBS-3 system. FSW is capable to produce a joint that has properties close to hot-worked base material. There are a small number of defects that can occur during FSW (SS-EN ISO 25239:2012) and all can directly be related to process parameters that can be controlled (Cederqvist 2011). Also, tests show that FSW produces welds that fulfil the functional demands set (SKB 2010).

One imperfection that can form during FSW is that remnants in form of dirt or oxidised surfaces become embedded in the final weld. The dirt can be controlled by cleaning the surfaces prior to welding and the oxides can be avoided by producing welds under an inert gas atmosphere (Björck et al. 2017, Savolainen 2012). Previous studies (e.g., Rantala et al. 2014, Wu 2011a, b) have indicated a decrease in mechanical properties, especially creep ductility, due to embedded oxide particles in welds. However, these studies have mostly been performed at temperatures above 75 °C which is assumed to represent the conditions in the repository of spent nuclear fuel. In aluminium there have been reports that oxide particles embrittle the material (Chen et al. 2006, Zhou et al. 2006).

It can be envisaged that large amount of oxides will be detrimental also for the corrosion properties as copper oxide is not necessarily stable in the environment surrounding the canister. Previous experiments have not shown any indication that FSW produces material that is more susceptible to corrosion rates than the base material (Gubner and Andersson 2007).

Thus, the literature shows that oxide particles can have an influence on the mechanical properties and corrosion properties. Studies where the oxide content is systematically varied have not been carried out before. This work will study the effect of entrapped oxide particles (oxide streaks) on the mechanical and corrosion properties as a function of the initial oxide film thickness. If any of the properties is strongly affected by the presences of oxide particles this information can be used to set a process window for the welding process.

2 Weld preparation

It is difficult to create a homogenous streak of oxide particles in the weld by changing the oxygen level in the surrounding atmosphere since the oxidation throughout the weld depth is not homogenously distributed, see Appendix. To create a more controlled experiment one joint surface was pre-oxidised prior to welding. The welding was conducted with an external and internal inert gas shield known to produce a negligible amount of oxide particles (Björck et al. 2017). The aim was to have a known, homogenous, oxide film prior to joining.

During the design of the experiment a compromise was sought between having objects for pre-oxidation that could be handled under controlled lab conditions and at the same time contain enough material so that both corrosion tests as well as creep testing could be conducted. With this in mind 60° segments of welding rings were selected since this was the maximum size that could be fitted in a laboratory box furnace at Swerea KIMAB. Six segments made up one ring to be welded, see Figure 2-1. Using one segment as start and stop for the weld resulted in 5 segments that could be used for different oxide thicknesses. The segments were mounted onto a supporting ring. To facilitate measurement of the final oxide thickness space for coupons was created in the screw holes.

The maximum oxide thickness formed during welding in air has been estimated to be 8μm (Björck 2015). In order to validate this result experimental investigation of a down travel sequence conducted in air has been investigated with SEM and is presented in Appendix. The measured maximum oxide thickness was found to be 3 μm at the outer surface of the canister in good agreement with the calculations which estimated 3 μm before the final passage. It should be noted that this estimate is conservative since the joint surfaces had a lower oxide thickness.

Based on the above argumentation the maximum oxide thickness should be at least 10 μm. The initial plan was to have the maximum oxide thickness to 50 μm and then decrease to 10 μm from where it would be decreased in decades. The desired oxide thicknesses were thus: 50, 10, 1, 0.1 and "0" μm. However, severe flaking occurred at an oxide thickness of 10 μm and above rendering it impossible to create an adherent oxide film for thicker layers. This is in agreement with industrial knowledge for phosphorous alloyed copper (ASTM 2016b).
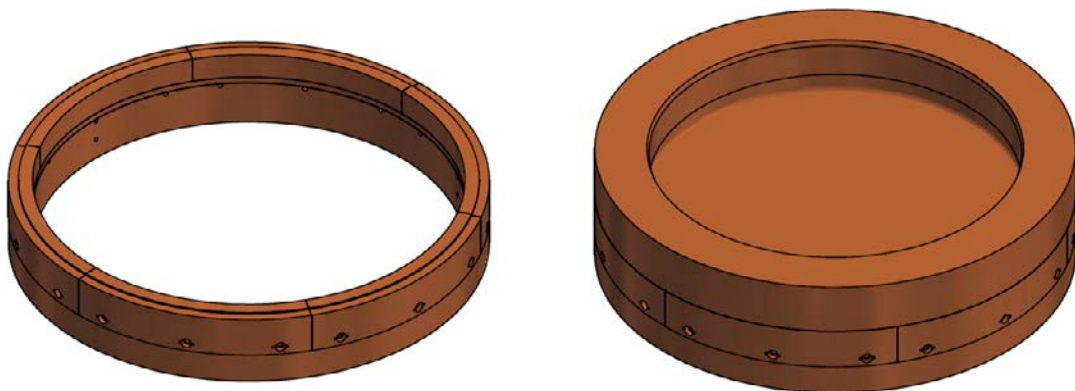

Figure 2-1. A sketch of the six segments placed on the supporting ring, left, and the assembled lid and ring intended for welding, right.

2.1 Oxidation

The exposures were performed in a laboratory box furnace in air environment at three different temperatures. Exposure time and temperatures were selected based on simulations using Björck and Elger (2013) model in order to achieve the desired oxide thicknesses. This model is used throughout this section for simulations. After the predetermined exposure time, the door of the oven was opened to enable faster cooling and slow down further oxidation. The complete cooling time to room temperature was approximately 10 h. The samples were put in and removed out of the furnace at room temperature.

A drawing of one sample is shown in Figure 2-2, left. The drawing shows the sample from the outer surface. Three screw holes with approximate diameter of 22 mm were present in the sample. As the sample should be further used in the welding cycle, it could not be sectioned for the GDOES and SEM analysis. Instead, discs of identical material and preparation were mounted in the screw holes indicated using a copper cylinder and two screws to secure the cylinder in place. The discs were mounted from the outside of the sample. A sketch of the disc mounted in the screw hole is shown in Figure 2-2, right. A photograph of the sample in the oven showing the inside of the sample and of the mounted analysis disc is shown in Figure 2-3. In the SEM/GDOES analysis, the middle disc was used for the SEM/EDS analysis and the innermost disc for the GDOES analysis. Only the outside of the discs was analysed.
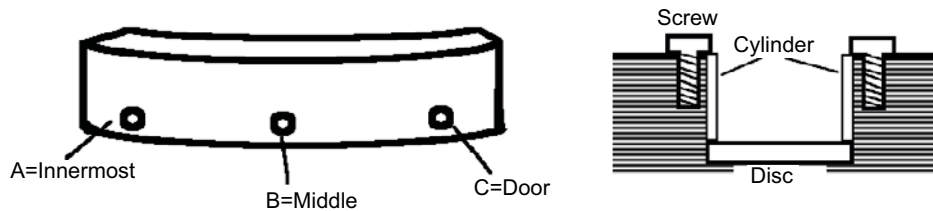
Figure 2-2. *Drawing of the exposed sample observed from the outside (left). Sketch of the mounting of the sample disc (right).*

Figure 2-3. *Photograph of the segment placed in the laboratory furnace with an insert showing an image of a mounted SEM/GDOES sample.*

As the surface temperature of the samples could not be monitored since a thermocouple will disturb the growth of the oxide layer, heating was performed slowly to avoid temperature gradients within the samples. A dummy sample with three connected thermocouples inserted in the sample was used to determine the final heating profile of the oven. The dummy sample had similar weight and volume as the final samples (Figure 2-4). The heating profile was then adjusted so that the final temperature was within a temperature range of ±2 °C from the final temperature. This is the maximum deviation allowed at exposures performed below 300 °C according to the standard for high temperature corrosion described in SS-EN ISO 21608:2012. Calibration of the dummy thermocouples was performed after the exposures. It was assumed that the temperature profile of the final samples was equal to the temperature profile of the dummy sample. The recorded heating profiles from the dummy sample at three different final temperatures were used for determining the needed exposure time for the desired oxide thicknesses. As expected, the spread in simulated oxide layer thickness due to temperature differences in the furnace was small for all evaluated cases, see Figure 2-5.

Figure 2-4. Photograph of the dummy sample with inserted thermocouples in the laboratory oven.
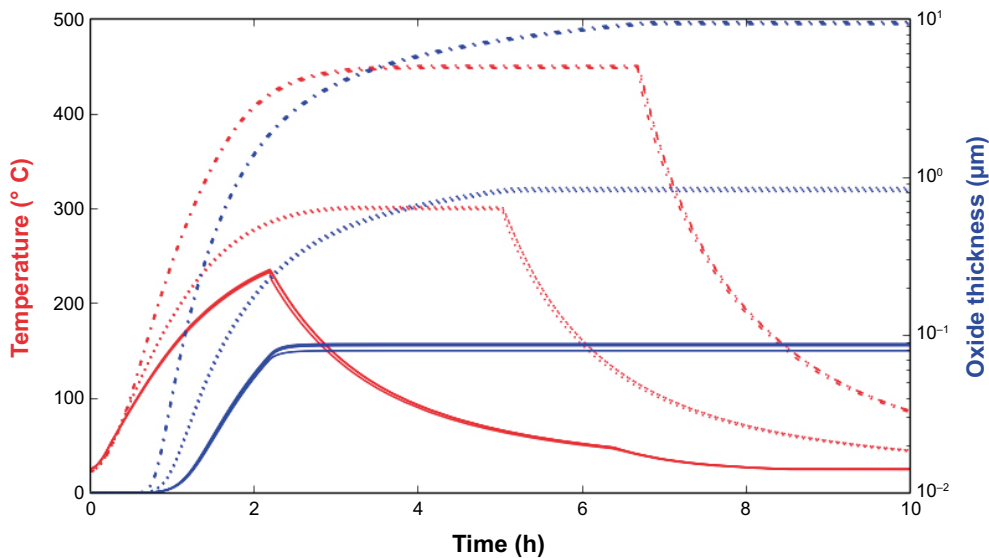

Figure 2-5. Oven calibration curves for three different final temperatures. The red curves show the temperature as a function of time (left axis). The blue curves shows the oxide thickness as a function of time (right axis) for each termoelement in the dummy sample, see Figure 2-4. Full lines denote exposure 232 °C, dotted lines exposure 300 °C, 5h and dash-dotted lines exposure 447 °C.

The maximum calibrated deviation from the final temperature of the dummy samples was within the span accepted by the standard at all positions. Generally, temperature was highest in the middle position and somewhat lower at the door and innermost positions. The calibrated final temperatures and the maximum deviation as well as the total time spans used in the exposures are given in Table 2-1. Heating cycles of the oven as measured in the dummy sample are included in Figure 2-5 together with simulations of the oxide thickness as a function of time.

Table 2-1. Information regarding temperatures and time spans for the different exposures. Temperatures are measured on the dummy sample.

Exposure	Calibrated final temperature	Maximum temperature deviation at final temperature	Time span, including heating
232 °C	248.5	1.31	2h 12 min
300 °C, 5 h	299.1	1.42	5 h
300 °C, 72 h	299.1	1.42	72 h
447 °C	447.0	1.93	6h 40 min

Photographs of the samples after exposure are given in Figure 2-6. The sample discs are shown in Figure 2-7. As displayed in the photographs, the three samples exposed to 232 °C and at 300 °C showed little delamination of the oxide, whereas the 447 °C sample spalled heavily. The sample exposed to 232 °C showed a very thin, gold-coloured layer of oxide which was not regarded possible to analyse by SEM. Only GDOES was performed for this sample.

Measurements on the oxide thickness were made in the SEM with values given in Table 2-2. The images in Figure 2-8 show typical examples of the oxide thickness and topography of the underlying metal surface after the different exposures. To confirm the presence of an oxide layer, EDS analysis (not reported here) was performed on the oxide film indicated in each image. It was observed that all oxides appeared to have poor attachment to the underlying metal, but even though care was taken to avoid damage, this might be due to sample preparation for SEM evaluation. In Figure 2-9, the measured oxide thickness analysed by GDOES is shown for the four different exposures. For GDOES, the oxide thickness is analysed as the thickness where the oxygen signal is 50 % of the oxygen level at the plateau caused by the oxide layer. All results are summarised in Table 2-2.
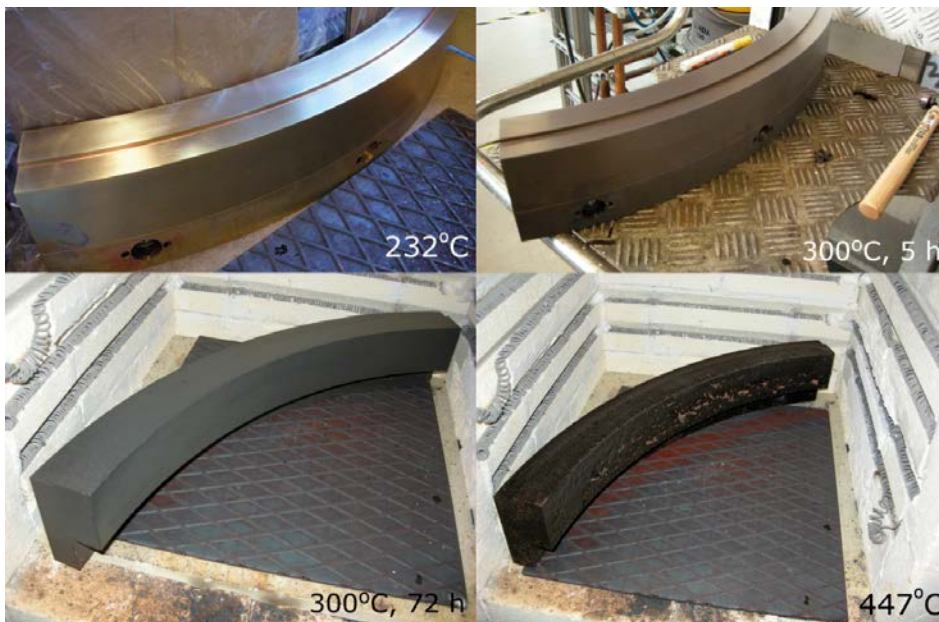

Figure 2-6. *The samples after exposure. The designation of each sample is given in the figure.*
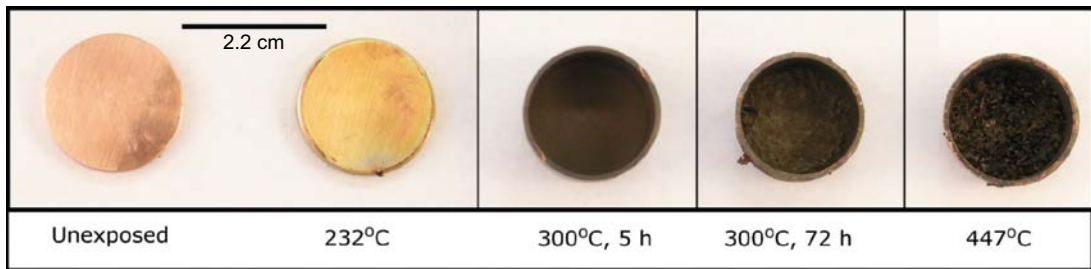
Figure 2-7. The sample discs after exposure. The designation of each sample is given in the figure.
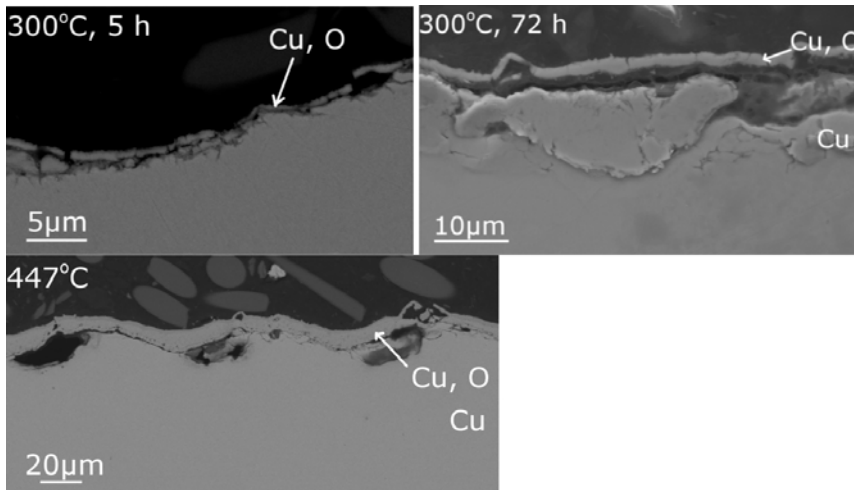

Figure 2-8. Upper, left: Back-scattered SEM image after 5 h exposure in the 300 °C heating cycle. Upper, right: Secondary electron image of disc after 72 h exposure in the 300 °C heating cycle. Lower, Back-scattered SEM image after 6h 40 min exposure in the 447 °C heating cycle. Note the different magnifications.
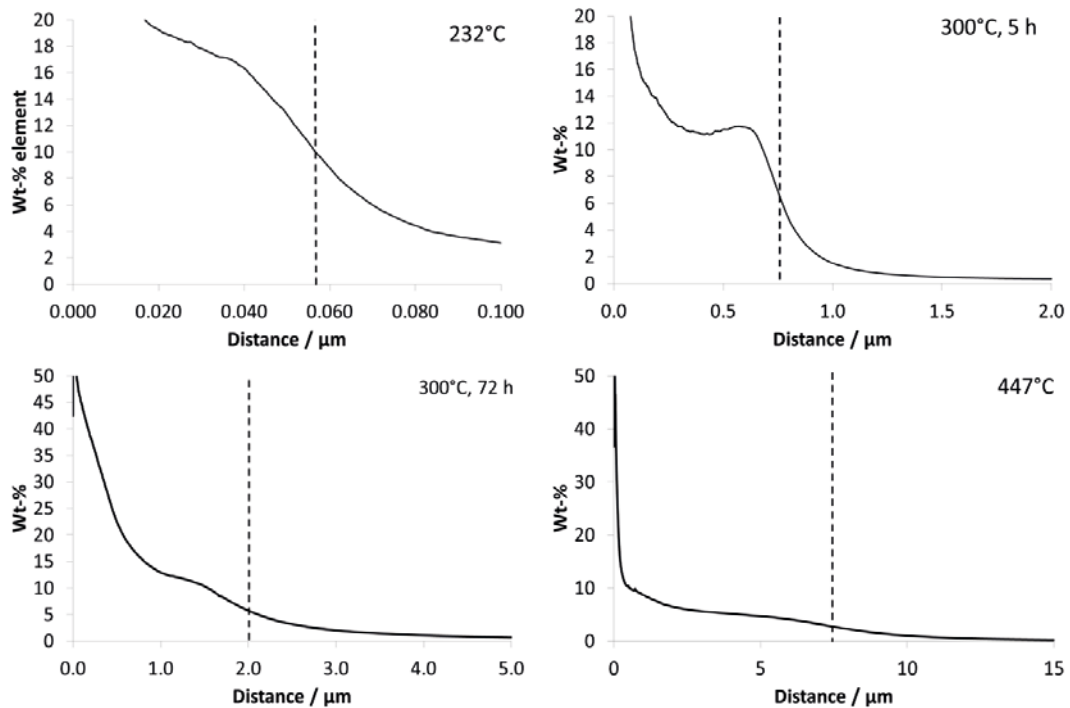

Figure 2-9. GDOES results as weight percentage oxygen as function of distance after the four indicated exposures. The dashed line indicates level of 50 % of maximum oxygen signal, excluding initial oxygen peak.

Table 2-2. Oxide thickness determined by SEM/EDS and GDOES.

Segment #	Exposure	Oxide thickness, SEM/EDS	Oxide thickness, 50 % O, GDOES	Modelled oxide thickness
6	232 °C	n/a	0.06 μm	0.1 μm
1	300 °C, 5 h	~1 μm	0.8 μm	0.89 – 0.85 μm
5	300 °C, 72 h	1.5 – 1.7 μm	2 μm	4 μm
2	447 °C	6 – 11 μm	8 μm	9 μm

In general, the exposures resulted in approximately equal oxide thickness of the discs as in the simulations when compared to maximum deviation of 40 % observed when developing the model (Björck and Elger 2013).

2.2 Welding

The different segments were mounted to the supporting ring at the Canister laboratory, with the supporting ring mounted onto a steel plate with gas line and vacuum connections as described by Björck et al. (2107). The mounted segment can be seen in Figure 2-10. Care was taken not to contaminate the surfaces of the segments or remove the fragile oxide film. During handling, flakes of oxide had loosened from segment 2. Some areas were not covered by oxide film, see Figure 2-10. When mounting the lid, the bare spots where covered with oxide flakes in order to produce a more even oxide film coverage. Segment 3 and 4 were cleaned abrasively with a rotating Scotch-Brite brush and then wiped with ethanol as described by Björck et al. (2017). The diameter of the reassembled ring was measured and the dimensions of the lid were adapted to the assembled ring.

The lid and ring was transferred to the welding machine. The outer gas shield was engaged. However, when vacuum was pumped on the inside of the ring the gap between the segments leaked so much that the gas in the outer gas shield was pumped at such a rate that air started to leak into the outer gas shield. This was noticed by an increase in oxygen content. Instead, the flow rate for the inside of the canister were fixed to 20 l/min for all the gas regulators and after 20 min the oxygen content on the inside as well as on the outside were below 40 at-ppm. The flow for the distributors located on the outside were set at 25 l/min. Details of the gas shield setup has been described previously (Björck et al. 2017).
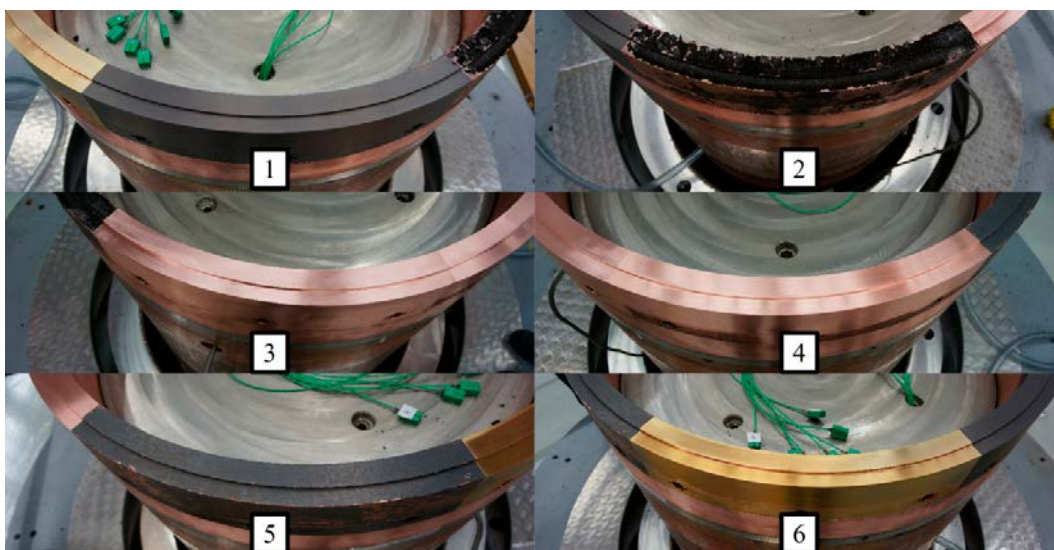

Figure 2-10. *The segments mounted to the supporting ring prior to placement of the tube. The numbers in each image is the segment number used in the report. Segment 2 and 5 show flaking.*

The zero position (start position) for the welding was defined 12 degrees into segment 4 from the transition between segment 4 and segment 5. The joint line was reached within segment 4. All monitored oxygen levels were below 30 at-ppm until an angle of 256° when the inflatable radial seal of the gas shielding broke and the oxygen level rose rapidly as shown in Figure 2-11. An angle of 256° corresponds to the middle of segment 6. The welding was stopped at an angle of 275.5°. The weld was allowed to cool and the seal was replaced and the welding was restarted at an angle of 278°. Segment 5, the last segment, was welded successfully. The SKB internal weld identification number is FSW113, used for traceability, and consists of lid TX201 and material from copper tube T76.

Before restarting the welding a failure analysis was conducted. The identified cause of the failure of the inflatable seal was the use of a lid that had been used for process development of the forging process and had not fully the correct shape, see Figure 2-12. This caused the water cooling channels in the lid clamp to not have direct contact with the lid. This probably caused the temperature to rise in the object. This also indicated that the inflatable seal had low margins towards a failure. The decision was taken to replace the inflatable seal with another design. The chosen design was to instead have three lamellas made of silicon rubber with tight fit against the canister surface. This, new design, currently maintain an oxygen level below 100 ppm in the gas shield and is also a more robust solution.
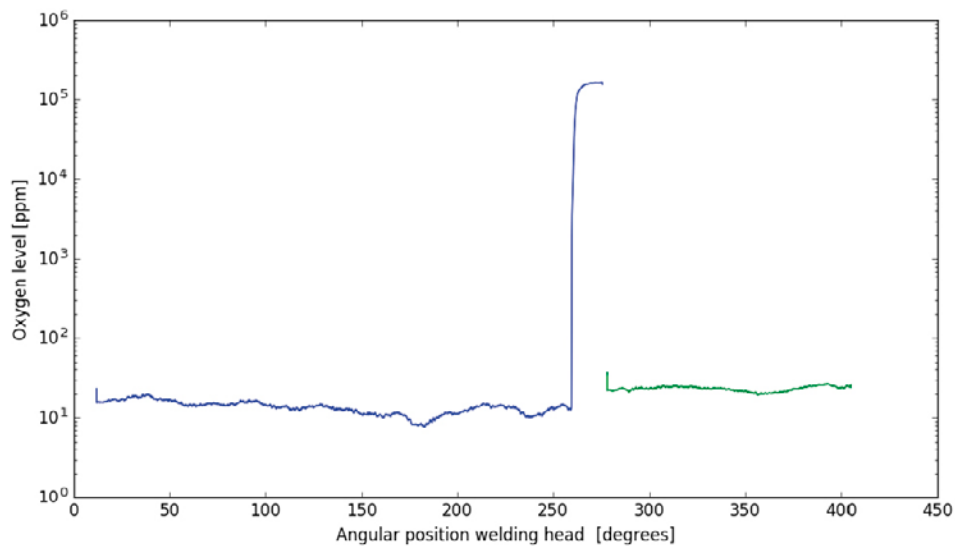

Figure 2-11. *The oxygen level for the first welding sequence (blue line) with a sharp increase in oxygen level when the inflatable seal failed. The restarted weld with a new seal is shown as a green line.*

Figure 2-12. *A picture of the lid used for welding. Note the radius (black) on the top of the lid. See text for details.*

3 Metallography and mechanical properties

3.1 Materials and methods

The welded segments with different initial oxide contents were delivered to Swerea KIMAB for further studies. This included both metallographic studies to characterise the extent and position of the oxide streaks as well as the influence of the oxide thickness on corrosion and mechanical properties. The weld, denoted as FSW113, was divided in six segments and is schematically presented in Figure 3-1. Table 3-1 summarises the oxide thicknesses and the denotations for the segments.

For hydrogen embrittlement tests and metallography, specimens of about 10 mm in thickness were cut from each segment. For mechanical testing, slices of up to 18 mm in thickness were first cut for further specimen preparation. All the specimens are denoted with the degree indicating the position in Figure 3-1.

Table 3-1. The initial oxide thicknesses and denotations used for the segments.

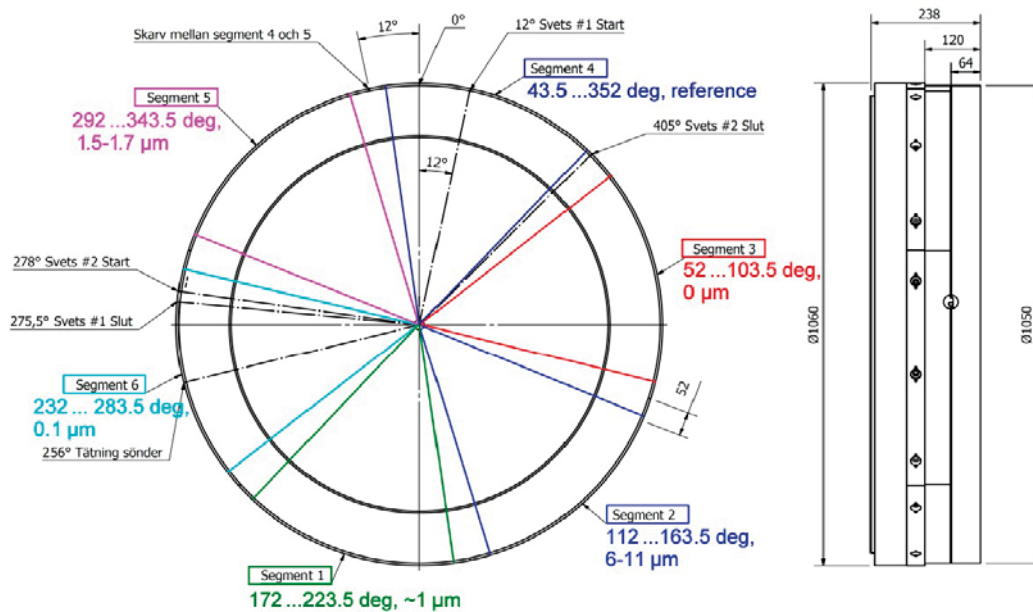| Segment	Initial oxide layer thickness	Deg. start	Deg. end
Segment 1	~1 µm	172	223.5
Segment 2	6–11 µm	112	163.5
Segment 3	0 µm	52	103.5
Segment 4	Reference	43.5	352
Segment 5	1.5–1.7 µm	292	343.5
Segment 6	0.1 µm	232	283.5

Figure 3-1. *The welded canister consisting of six segments for tests with different oxide contents.*

3.1.1 Metallography and hydrogen embrittlement susceptibility tests

The metallographic investigations in this work were carried out in order to identify the position and extent of oxide streaks in welds. Macrostructure of the welds was studied on specimens that were first mechanically ground and polished followed by local electrolytic polishing and etching. An example of weld cross-section and specimens cut for further studies is shown in Figure 3-2.

Hydrogen exposure tests were performed to identify the oxide streaks in welds. The testing is carried out according to the standard ASTM B577-10 Standard Test Methods for Detection of Cuprous Oxide (Hydrogen Embrittlement Susceptibility) in Copper method B (ASTM 2016a). The specimens cut from the welds with different oxide contents were heat treated in an atmosphere of at least 10 % hydrogen at 850 °C for 20 to 40 minutes. The presence of cuprous oxides in the heat treated and thereafter quenched specimens is evaluated using light optical microscopy (LOM).

3.1.2 Mechanical testing

In this study, the focus is on the effect of entrapped oxide particles. Therefore, a specimen with a short gauge length was designed for the mechanical tests as described below. The specimens were manufactured in such a way that the loading direction was perpendicular to the oxide streak to maximise the role of the impurities. The primary parameter quantifying the tensile and creep ductility of the specimens with different oxide contents is the reduction of area after failure.

Specimen design

Creep testing of cross-weld specimens where a large area of the FSW-zone is contained within the specimen gauge length has shown (Andersson et al. 2007) that necking occurs in the heat affected zone (HAZ) of the weld. In fact, necking in some cases occurred on two locations along the gauge length. To ensure that the experiments probe the streak of oxide particles, the tensile and creep specimens were designed in such a manner that the oxide streak is located in the middle of the gauge length and perpendicular to the loading direction. The specimen geometry is presented in Figure 3-3.
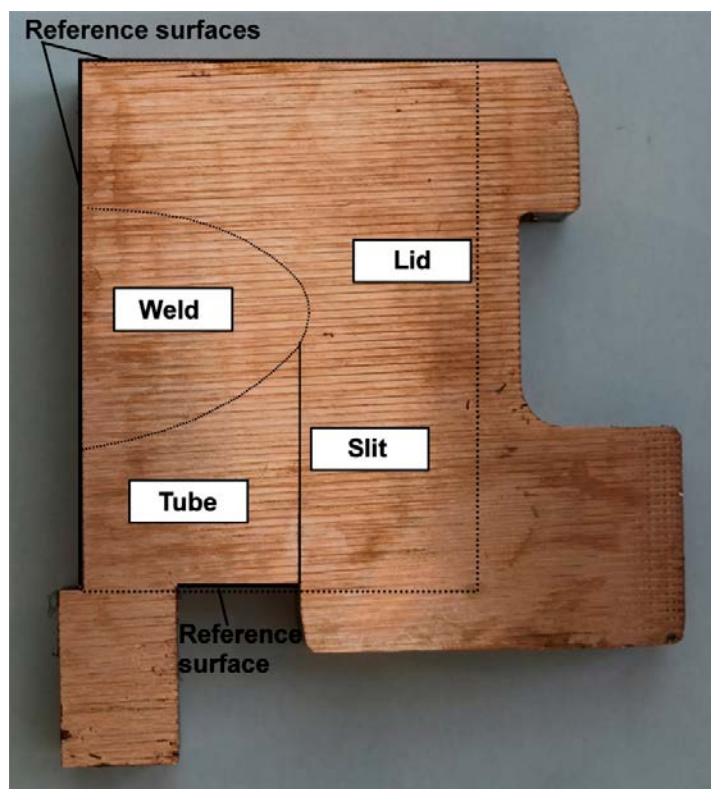

Figure 3-2. Cross-section of a welded roughly cut canister. Rectangular specimens indicated with dashed straight lines were cut from the segments for further investigations. The weld zone of interest is also indicated in the figure.

A finite element analysis (FEA) carried out prior to the specimen manufacturing. A linear elastic material with non-linear isotropic hardening was used to describe the deformation behavior of copper. Figure 3-4 shows the strain and stress distribution along the specimen. Only a quarter of the specimen is simulated due to symmetry.

Cross-weld specimens from segments 1, 2 and 3 were also manufactured and tested in order to evaluate if the cross-weld specimens showed a different behavior than the local specimens. The specimen geometry is shown in Figure 3-5. The specimen is a slightly modified standard creep test specimen with a 50 mm gauge length. The total length of the specimen had to be reduced to enable positioning the specimen across the oxide streak.
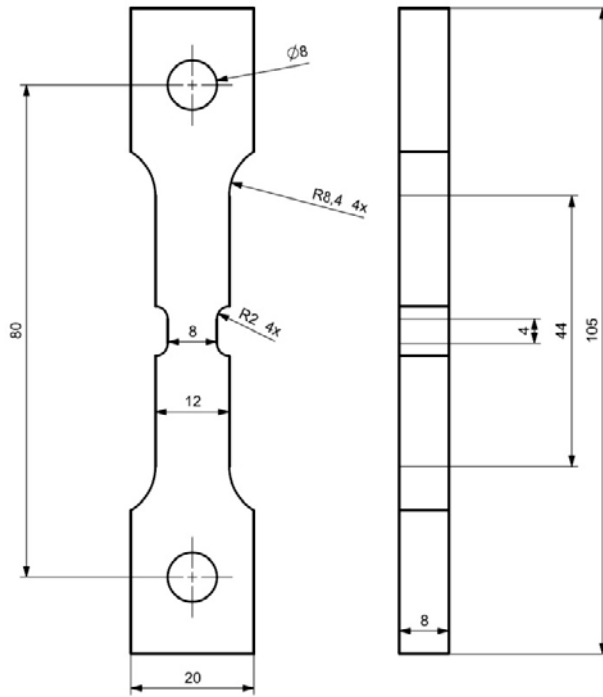

Figure 3-3. Specimen geometry to study the effect of oxide streak in tensile and creep loading.
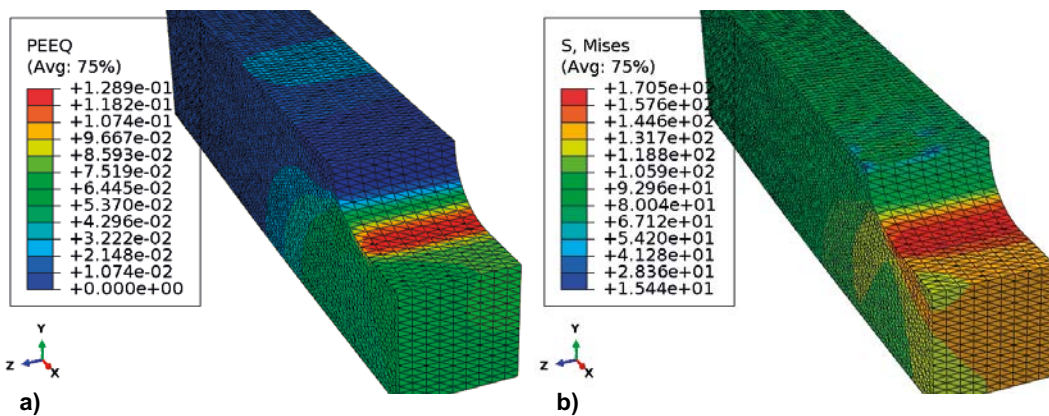

Figure 3-4. FE-analysis of the specimen geometry. A) equivalent strain and b) von Mises stress.
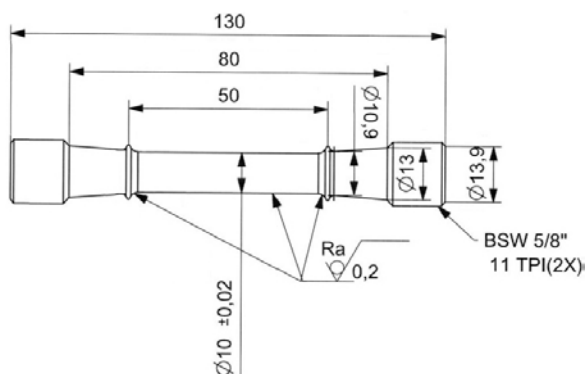
Figure 3-5. Specimen geometry for the cross-weld specimens.

Specimen manufacturing

Slices for tensile and creep testing of about 18 mm in thickness were first cut using a saw from each segment. Each cut piece is denoted with the canister identification number (FSW113), angular position along the lid and the segment, i.e., FSW113_138_2 indicates angular position 138° and segment 2. The slices were then milled to a thickness of 8 mm. The approximate position of the oxide streaks in each segment was defined based on the metallographic and hydrogen embrittlement studies. Thus, a smaller area could be selected for electrolytic polishing and etching to identify the exact position of the oxide streak in each individual specimen. An example of a locally polished specimen and the method to define the final position of the creep or tensile test specimen is given in Figure 3-6a. Markings are made to position the two D=8 mm holes as described in Figure 3-3. These markings and holes are further used in the subsequent wire electric discharge (WEDM) cutting of the specimens to final shape. Figure 3-6b shows the same WEDM cut specimen with the oxide streak positioned perpendicular to the loading direction within the gauge length of the specimen. All the creep and tensile test specimens were manufactured using the same procedure. The location of the oxide streak was also verified after the specimen manufacturing and prior to testing using a light optical microscope with a possibility to measure different features on the specimens. In addition, all the specimens were provided with markings at specific intervals (5−4−5 mm)

The cross-weld specimens from segments 1, 2 and 3 were manufactured by first cutting an about 18 mm thick piece. The position and angle to manufacture the specimens according to Figure 3-5 was determined based on specimen FSW113_63_3 and all the specimens were manufactured in the same angle as shown in Figure 3-7 of segment 3. In case of cross-weld specimens from segments 1 and 2, the oxide streak was visible after a light etching of the milled plates and thus the angle and position of each specimen was determined separately. The aim was that the 50 mm gauge length of the cylindrical specimens covers not only the oxide streak but the entire weld and heat affected zone (HAZ) in a similar way as was done in Andersson et al. (2007) and at the same time perpendicular to the oxide streak.

The reference specimens are manufactured from segment 4 with material without a weld and thus oxide streak, and are thought to serve as a reference for the bulk material.

Figure 3-6. *Example on positioning the oxide streak in the specimen gauge section. a) A milled specimen FSW113_221_1 that is electrolytically polished in the region of oxide streak. Two markings are made to ensure correct positioning and angle in WEDM-cutting of the specimens. B) A readily cut specimen with an oxide streak perpendicular to the loading direction and c) a specimen with markings for further deformation monitoring.*

Figure 3-7. *Schematic positioning of the cross weld specimens from segment 3 with 0 μm initial oxide layer thickness. The location of the oxide streak is given by the arrow. The metallographic sample is taken from segment 5 with 1.5–1.7 μm initial oxide thickness. The samples were extracted perpendicular to the oxide line.*

Hot tensile testing

In a previous study (Wu 2011a, b), indications of lower tensile strength and lower ductility were found when specimens containing oxide streaks were compared to defect free specimens. Tensile testing was carried out to see the effect of various oxide layer thicknesses on the deformation behavior of copper as well as screening for creep testing. The test matrix for the tensile tests carried out in this study is given in Table 3-2.

Table 3-2. Test matrix for the hot tensile tests.

Segment	Initial oxide layer thickness	Amount of tests	Temperature (°C)
Segment 1	~1 μm	2	75
Segment 1	~1 μm	2	175
Segment 1, cross weld	~1 μm	2	75
Segment 1, cross weld	~1 μm	1	175
Segment 2	6–11 μm	2	75
Segment 2	6–11 μm	2	175
Segment 2, cross weld	6–11 μm	2	75
Segment 2, cross weld	6–11 μm	1	175
Segment 3	0 μm	2	75
Segment 3	0 μm	2	175
Segment 3, cross weld	0 μm	2	75
Segment 3, cross weld	0 μm	2	175
Reference, segment 4	no weld	1	75
Reference, segment 4	no weld	1	175
Segment 6	0.1 μm	2	75
Segment 6	0.1 μm	1	175

The tensile tests at two elevated temperatures of 75 and 175 °C were carried out using a MTS servo-hydraulic materials testing machine that was equipped with an Instron 3119 series temperature chamber (−70 to 250 °C). The higher temperature were selected as to see if any embrittlement process would be accelerated by the higher temperature. The tests are carried out using displacement control at a constant displacement rate of 0.05 mm/min. In addition, a 25 mm gauge length, MTS extensometer 632.12C-20 was attached on the specimen as shown in Figure 3-8. As the Figure also indicates, the

extensometer measures the deformation over a much larger length than the original 4 mm gauge length. The figure also shows that the specimen deforms not only in the gauge length but also in the shoulder area as well as in the 12 mm wide section. Thus, the local strain in the gauge section cannot be accurately determined by conventional extensometer measurement. Therefore, a camera with a possibility for time lapse photography was used to monitor the deformation. Photographs were taken every 2–3 minutes and thus the deformation in the specimen gauge area could be recorded during the tensile tests. Another aim of the deformation monitoring was to record the location of the lowest ductility and the deformation behavior with regard to the oxide streak. The deformation was also recorded for the tensile tests of the cross-weld specimens to detect, i.e., localization of deformation.

Since the deformation measurement using the time-lapse photographs is mostly qualitative, the percentage of area reduction after failure is the primary quantitative measure of deformation behavior in each test.

Creep testing

All the creep tests were carried out in test rigs that are equipped with stepping motors to facilitate controlled loading. The tests with the rectangular cross-section and 4 mm gauge length were carried out in creep test rigs without an extensometer attached on the specimen as described in Andersson-Östling and Sandström (2011) and Mannesson et al. (2013). An extensometer was, however, placed in the load rod below the load cell. With a correction for the machine compliance, displacement could be measured. This displacement value, however, accounts for all the movement of the loading rod. As mentioned above in the case of hot tensile testing, the specimens deformed not only in the gauge section but also in the shoulders and the wider, 12 mm area. In addition, some deformation occurred in the gripping area, around the 8 mm holes. Thus, the elongation value obtained from the creep tests is only indicative and not a true measure of deformation in the gauge section. Instead, percentage of area reduction after failure and time to failure are used as quantitative measures when the results of creep testing are reported.

Attempts were also made to monitor the deformation of the specimens using the same setup as for hot tensile tests. However, the long duration of the creep test allowed only monitoring a few of the specimens and in that case during the loading phase and early deformation.

The testing of the cross-weld specimens of segment 3 was conducted in the same or similar creep test rigs as in Mannesson and Andersson-Östling (2016). In this case, elongation along the 50 mm gauge length is measured using internal extensometers. Thus, the strain describes the deformation behavior within the specimen gauge length only.

All creep testing in this study was carried out at 75 °C and the temperature was controlled to ±1 °C.
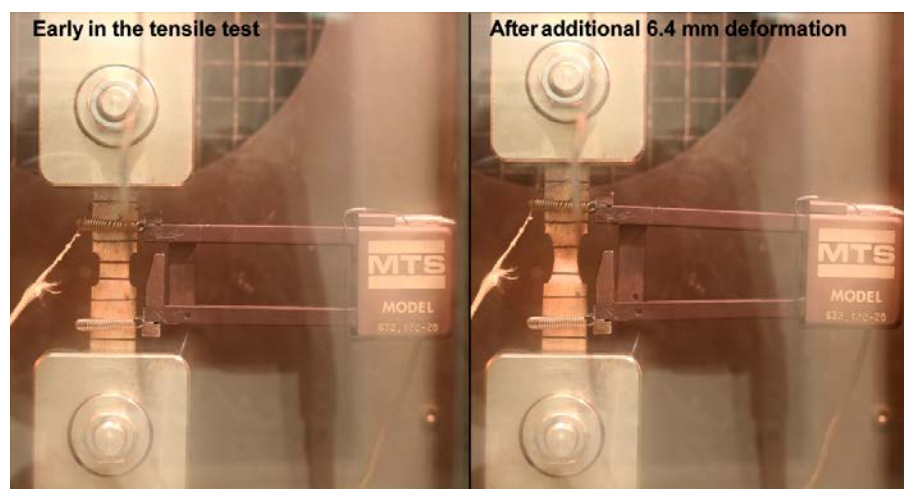

Figure 3-8. Hot tensile testing using a 25 mm extensometer in a temperature chamber. Example specimen FSW113_238_6 at 175 °C early during the tensile test (left) and after additional 6.4 mm elongation (right).

3.2 Results and discussion

3.2.1 Metallography and hydrogen embrittlement susceptibility tests

Specimens from each segment were studied using light optical microscopy (LOM) in order to identify the extent and position of oxide streaks in welds. Results of these studies are presented in Figure 3-9. Segments 1, 2 and 5 with initial oxide layer thickness greater than 1 µm show a clear streak of oxides in the weld zone. The two segments, 3 and 6 with low initial oxide content, do not show a sharp streak of oxides.

Based on the LOM studies, the position of the creep and tensile test specimens was decided as presented in Figure 3-10. This position with the oxide streak perpendicular to the loading direction is considered as the worst case in terms of effect on, e.g., ductility. The exact position and angle of the oxide streaks was measured in several specimens of the same segment but since the position could slightly vary, electrolytic etching of each slice to reveal the oxide streak as described above in Section 3.1.1 was considered necessary to position the specimen in a correct way.
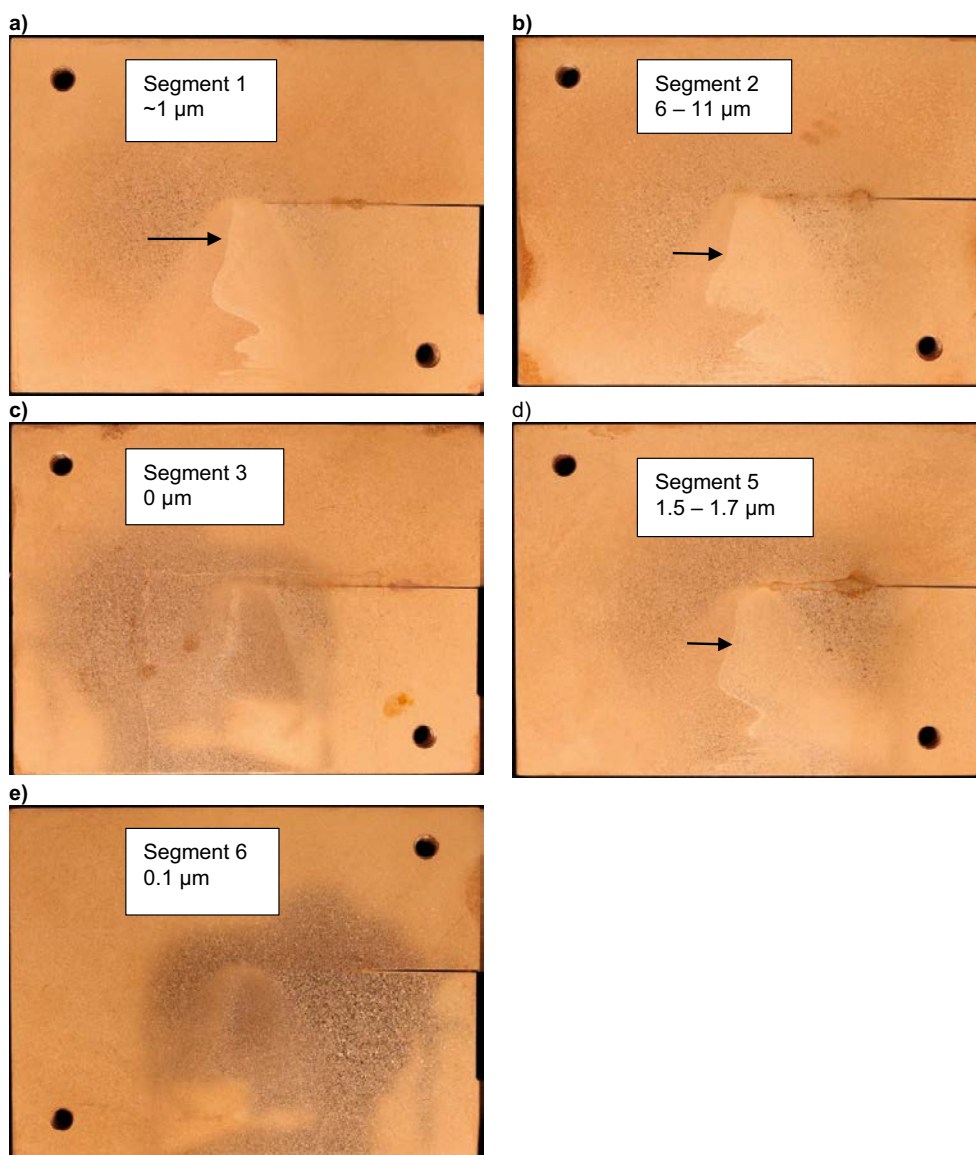

Figure 3-9. *Macroetched specimens of the segments with different oxide contents. a) Segment 1, specimen 223.5°, ~1 µm, b) Segment 2, specimen 163.5°, 6–11 µm, c) Segment 3, specimen 103.5°, 0 µm, d) Segment 5, specimen 343.5°, 1.5–1.7 µm, and e) Segment 6, specimen 232°, 0.1 µm initial oxide layer thickness. The arrows in the figures points to the location of the oxide lines.*
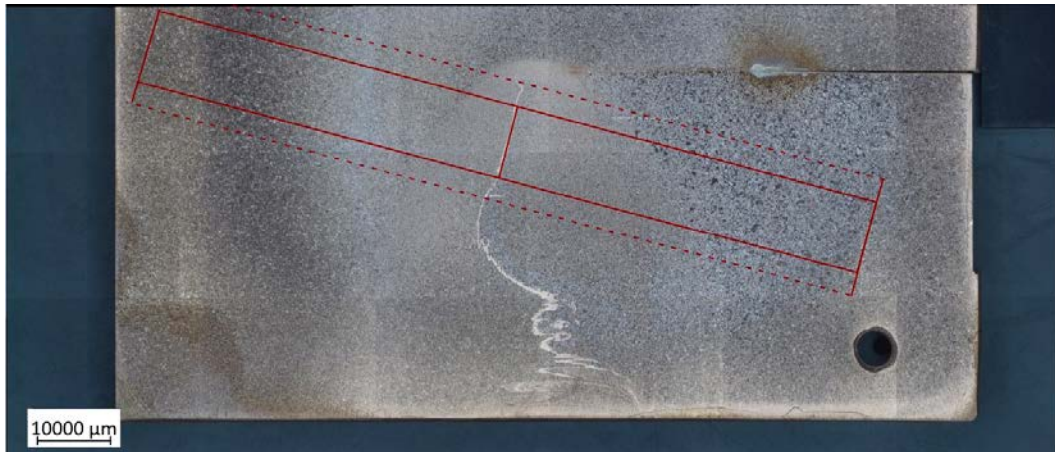
Figure 3-10. *Example of specimen position across streak of oxides, specimen FSW113_112_2 with 6−11µm initial oxide layer thickness.*

The oxide streaks were further studied by the hydrogen embrittlement susceptibility tests. The high temperature in combination with a hydrogen atmosphere reduces the copper oxides to copper and water vapour. The water vapour causes blisters making possible oxide streaks more visible in macro photographs and LOM. The results for segments 2, 3, 5 and 6 are shown in Figure 3-11 to Figure 3-14. As also the results in Figure 3-9 showed, the oxide streak is apparent in specimens from segments 2 and 5 but not visible in specimens from segments 3 and 6 with the lowest oxide contents.
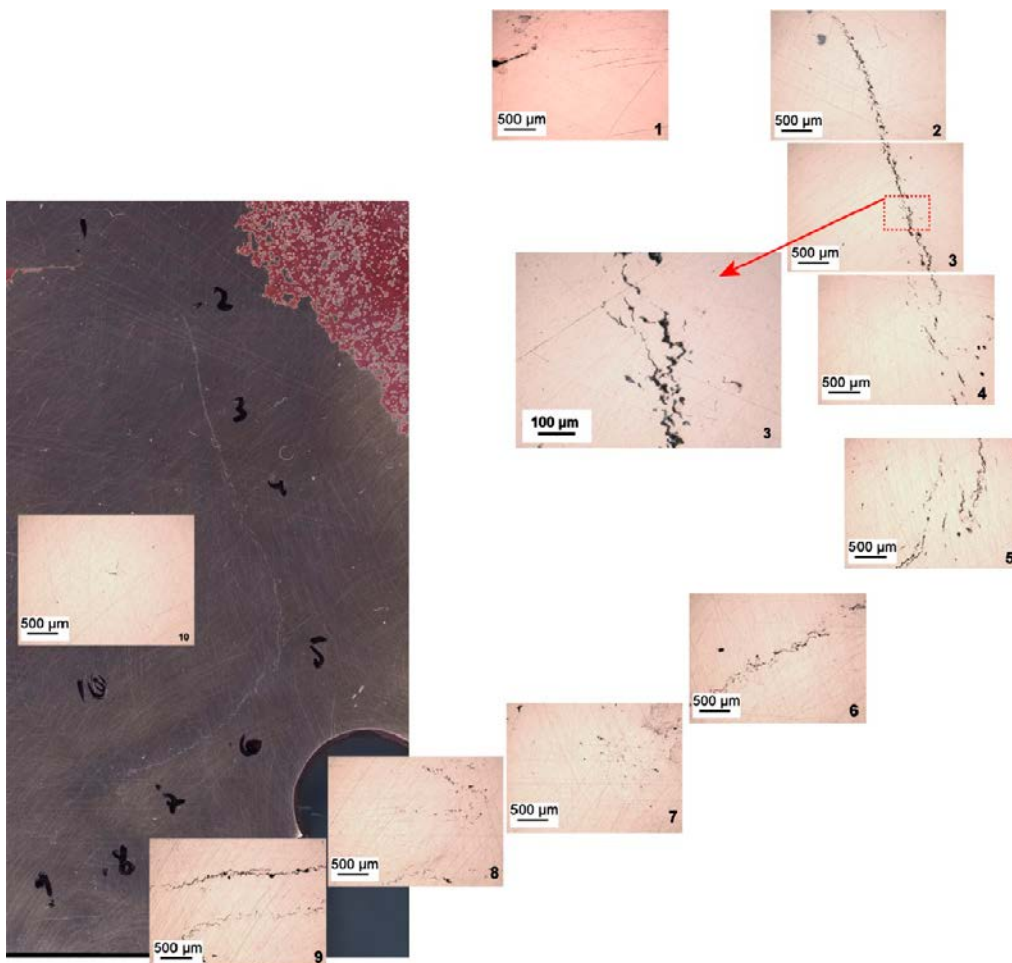
Figure 3-11. *Specimen of segment 2 with 6−11 µm initial oxide layer thickness after hydrogen exposure.*
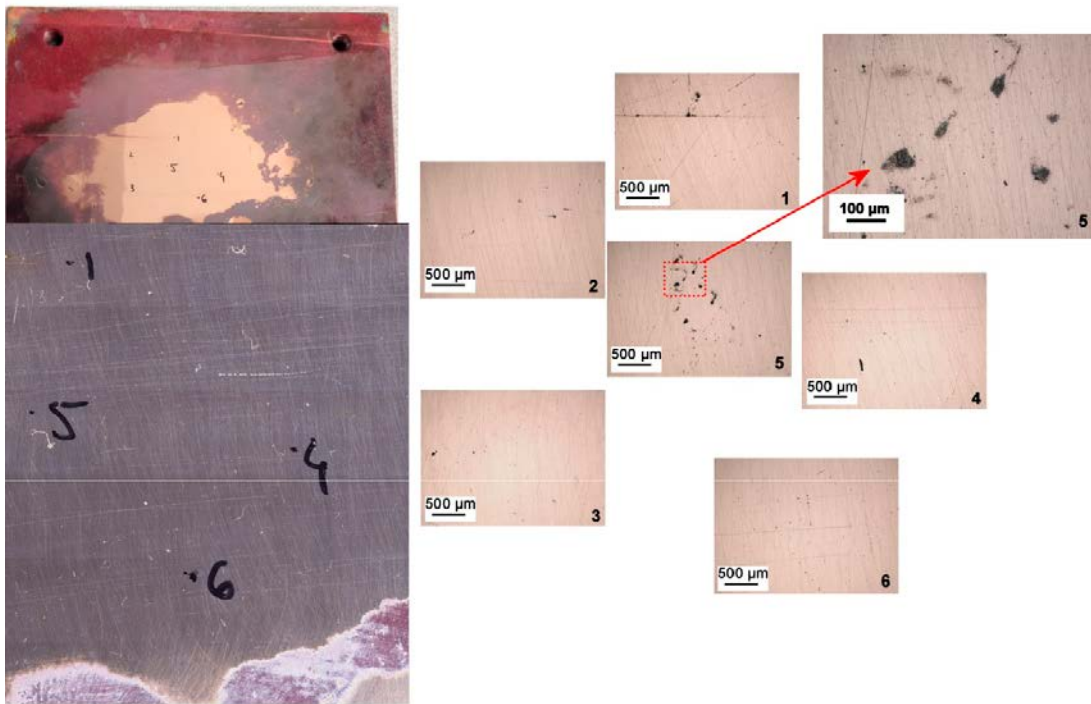
Figure 3-12. *Specimen of segment 3 with 0 µm initial oxide layer thickness after hydrogen exposure. The larger black dots is contamination from sample preparation.*
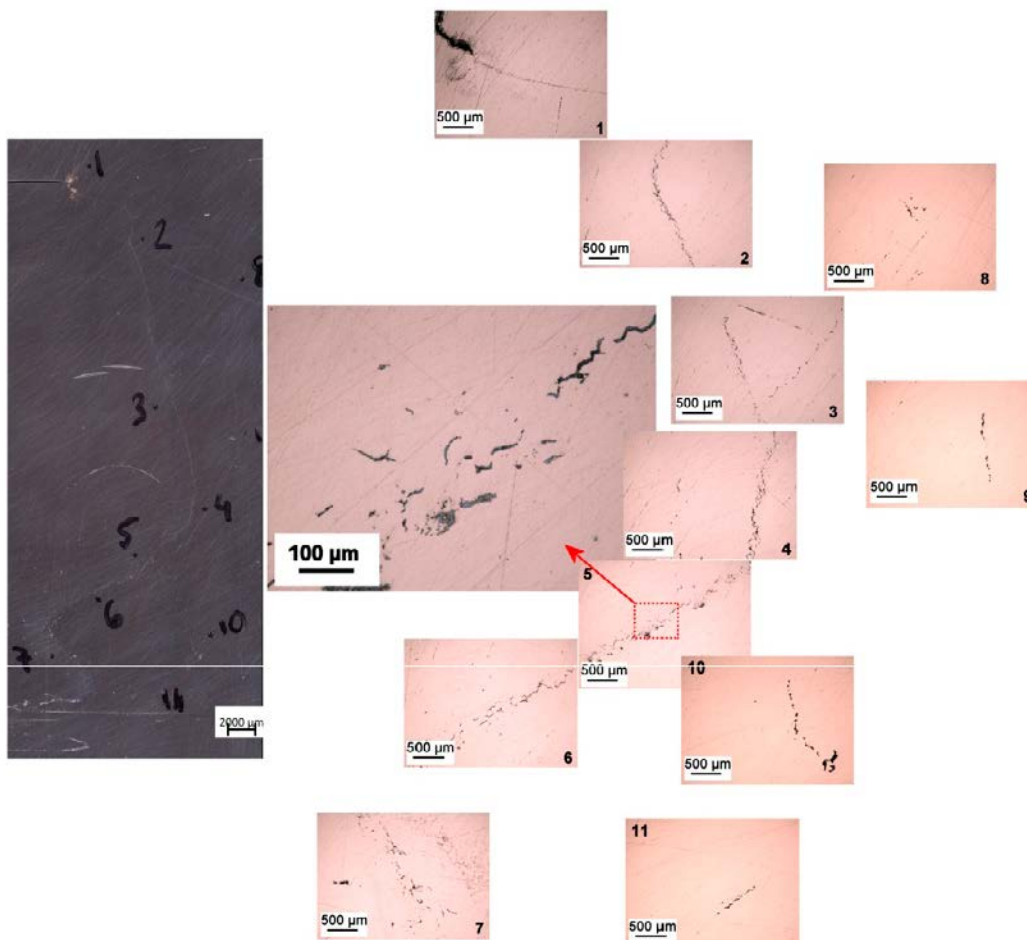

Figure 3-13. *Specimen of segment 5 with 1.5–1.7 µm initial oxide layer thickness after hydrogen exposure.*
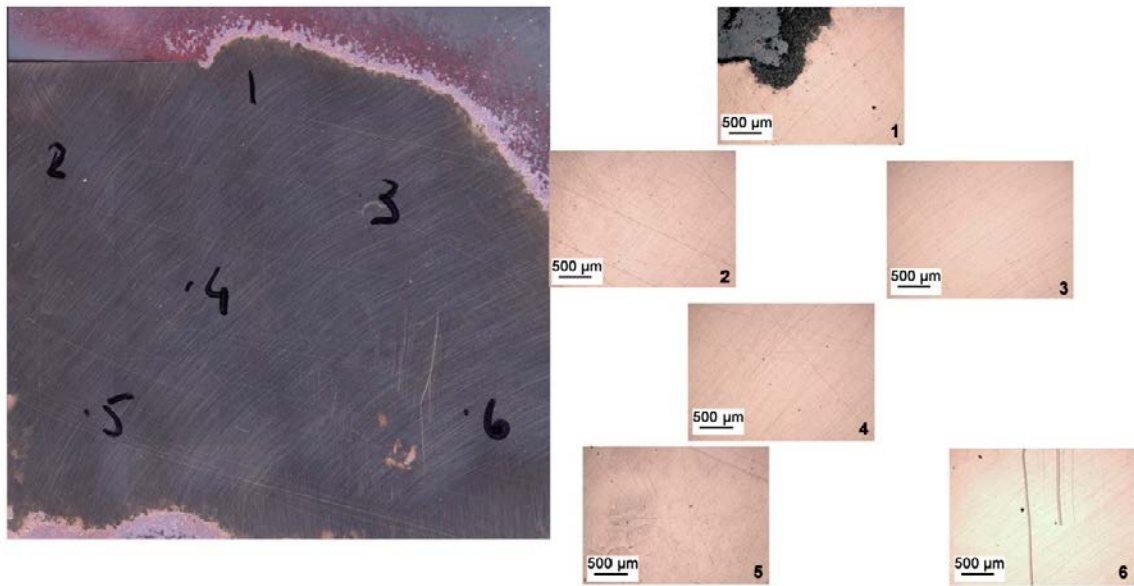
Figure 3-14. Specimen of segment 6 with 0.1 μm initial oxide layer thickness after hydrogen exposure.

3.2.2 Hot tensile tests

The results of hot tensile tests at temperatures of 75 and 175 °C are summarised in Figure 3-15 to Figure 3-18 and in Table 3-3. The true strain in the 4 mm gauge section could not be used to measure the deformation and thus the elongation is expressed as displacement that is measured either using a 25 mm gauge length extensometer (Figure 3-15) or the LVDT sensor recording the movement of the piston (Figure 3-16). The variation between two parallel tests (same initial oxide layer thickness and testing temperature) is rather small while the differences between the specimens from different segments are clear. These are indications of the robustness and sensitivity of the testing method. In the stress displacement curves, the displacement to failure observed for segments 1 and 2 is clearly smaller compared to segments 3, 6 and the reference. The same applies to cross-weld specimens at 175 °C (Figure 3-17). As expected, the tensile strength of the material is decreased by about 30 MPa when the temperature increases from 75 to 175 °C. The tensile strength measured for the specimens for different segments does not vary with the initial oxide content.

The most important quantitative measure from these tests is the reduction of area at failure presented in Figure 3-18. The ductility represented by the reduction of area is clearly lower for the specimens from sections 1 and 2 that have the highest initial oxide contents, about 1 μm and 6–11 μm, in these tests. The cross-weld specimens of these segments tested at 75 °C, however, reach about 90 % reduction of area while the ones tested at 175 °C fail in the oxide streak and show clearly lower area reduction values. Also for the specimens with 4 mm gauge length it appears that the decrease in ductility is higher at the higher temperature of 175 °C for specimens with highest oxide contents. There are no significant differences between the ductility of reference specimens and the specimens from segments 3 and 6.

The deformation behaviour of the specimens from different segments is further illustrated in Figure 3-19 and Figure 3-20 by the fracture surfaces from tests for different segments. There is a clear transition in fracture mode between segments 6 (0.1 μm oxide) which was very ductile and segment 1 (1 μm oxide) which appeared to be brittle.

The hot tensile tests of the cross-weld specimens manufactured of segment 3 as well as cross-weld specimens of segments 1 and 2 tested at 75 °C showed a ductile behaviour as evidenced by the area reduction values in Table 3-3. In these specimens, the area containing the possible oxide streak was placed in the middle of the 50 mm long gauge section. However, the failure occurred outside this area as shown in Figure 3-21 and Figure 3-22. In addition, another area with slight necking can be observed on the tested specimens. The deformation behaviour is similar to the one observed by Andersson et al. (2007) for cross-weld specimens after creep tests. Areas with coarser grains are observed in the HAZ of the specimens whereas the grains in the weld zone are smaller. The specimen fails and deforms most in the area of larger grain size. The tensile test results indicate a slightly lower tensile strength for the cross-weld specimens compared to the specimens where the deformation occurs mainly in the weld zone with the possible oxide streak and smaller grain size.

The stress displacement curves for the cross-weld specimens presented in Figure 3-17 and the reduction of area values in Table 3-3 show that at 175 °C the specimens from segments 1 and 2 have a lower elongation and lower reduction of area compared to segment 3. The difference in fracture type is also evident based on the fracture surfaces in Figure 3-23. Also, when the true stress-strain behaviour, i.e., the reduction of cross-sectional area with increasing deformation, of these specimens is considered, the strength of segment 3 at 175 °C is clearly higher than of the segments 1 and 2.
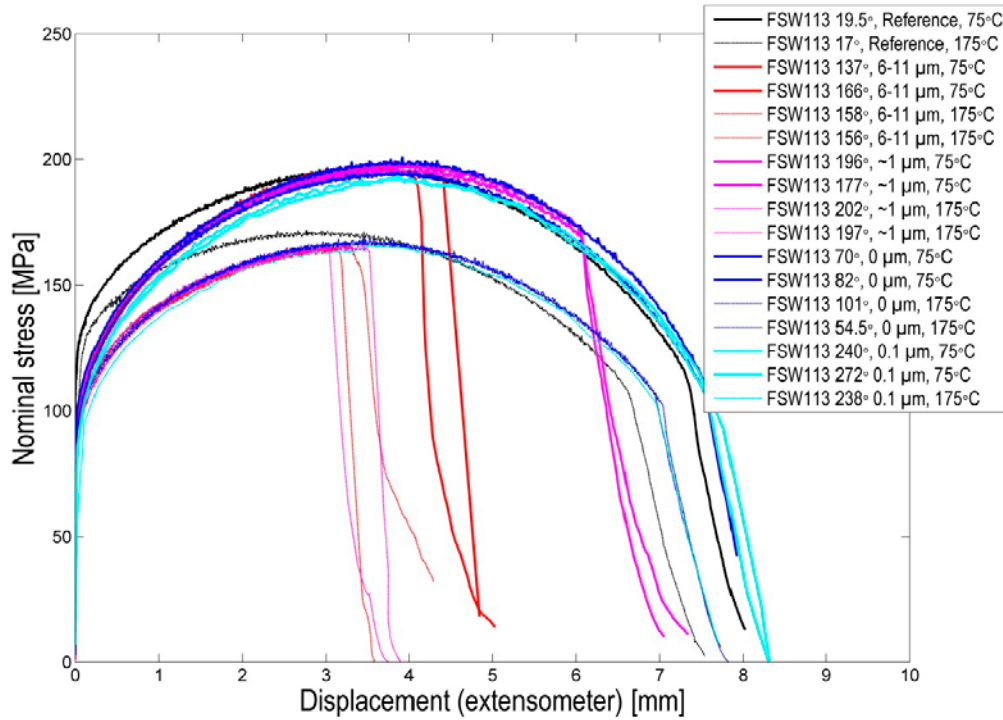
Figure 3-15. *Results of the tensile tests for the tensile tests for the rectangular specimens with 4 mm nominal gauge length.*
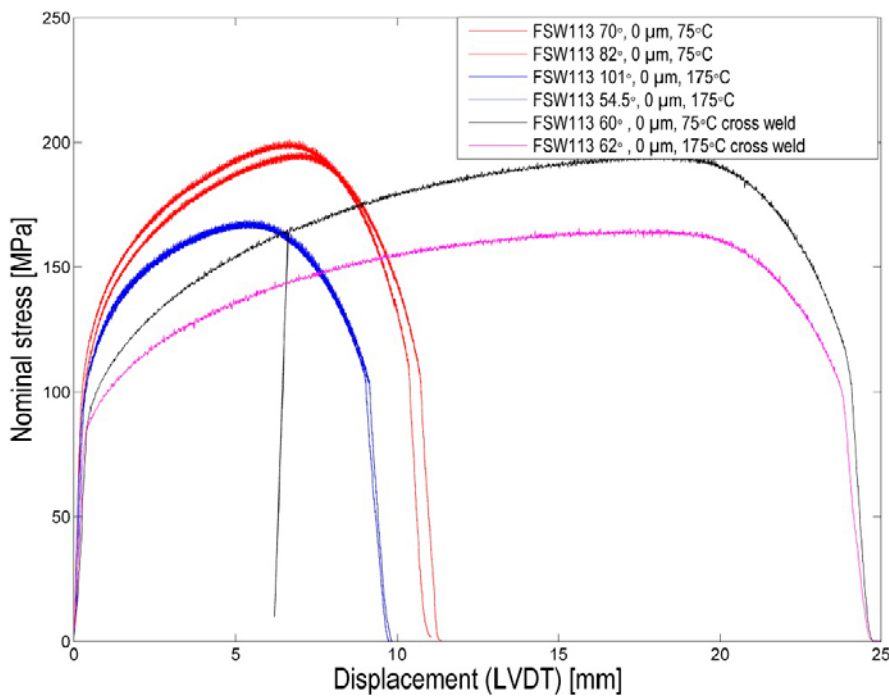

Figure 3-16. *Results of the tensile tests for the tensile tests from segment 3 with both specimens with 4 mm nominal gauge length and round, cross-weld specimens with 50 mm gauge length.*
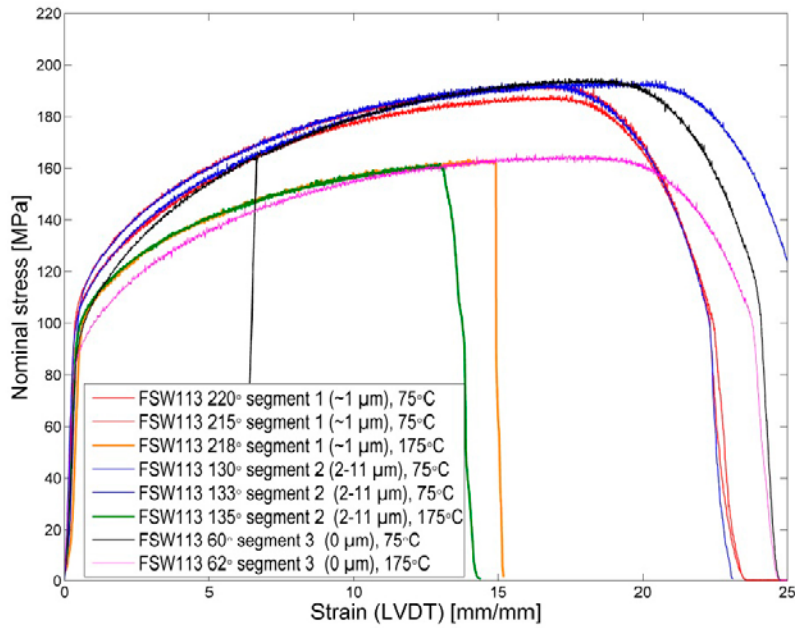
Figure 3-17. *Results of tensile tests for the cross-weld specimens from segments 1, 2 and 3 at temperatures 75 and 175 °C.*
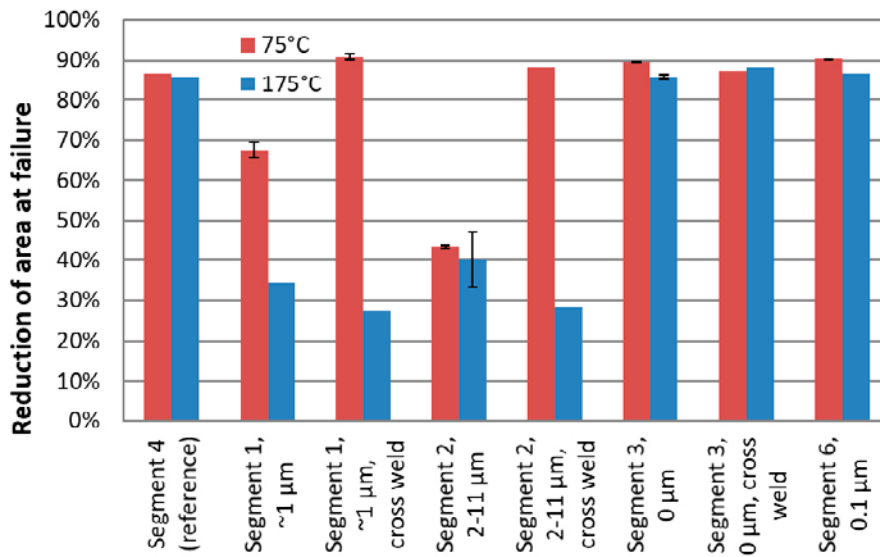

Figure 3-18. *Reduction of area for the hot tensile specimens at temperatures 75 and 175 °C. The error bars represent the range of two test results when available.*

Table 3-3. Results of the hot tensile tests.

| Segment	Angle (°)	Temperature (°C)	Reduction of area at failure (%)	Ultimate tensile stress (MPa)
Ref. segment 4	17	175	86	172
Ref.segment 4	19,5	75	87	198
Segment 1	177	75	69	198
Segment 1	196	75	66	200
Segment 1	202	175	34	167
Segment 1, cross weld	215	75	90	196
Segment 1, cross weld	220	75	92	193
Segment 1, cross weld	218	175	28	164
Segment 2	137	75	44	200
Segment 2	161	75	43	199
Segment 2	156	175	33	167
Segment 2	158	175	47	168
Segment 2, cross weld	130	75	88	194
Segment 2, cross weld	133	75	87	194
Segment 2, cross weld	135	175	28	162
Segment 3	70	75	89	201
Segment 3	82	75	90	196
Segment 3	101	175	85	169
Segment 3	54,5	175	86	169
Segment 3, cross weld	60	75	87	195
Segment 3, cross weld	62	175	88	166
Segment 6	240	75	90	194
Segment 6	272	75	90	195
Segment 6	238	175	87	167
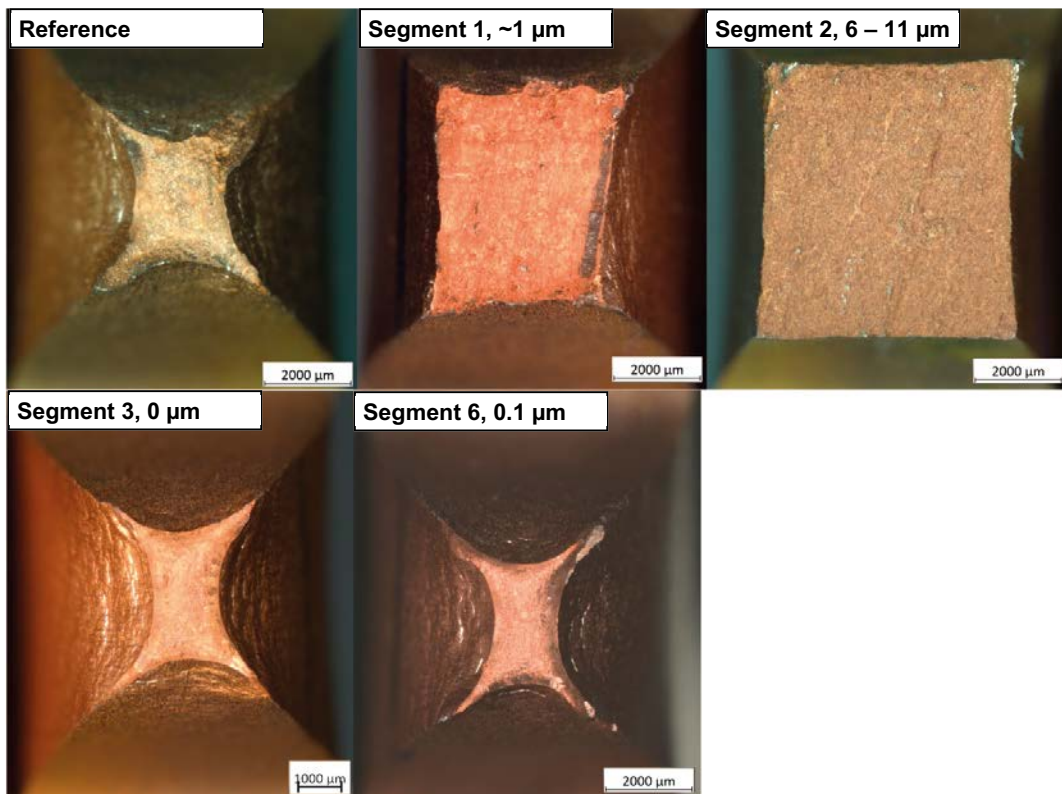
Figure 3-19. *Fracture surfaces of tensile test specimens tested at 75 °C. a) Reference, b) segment 1, position 177°, c) segment 2, position 161°, d) segment 3, position 70° and e) segment 6, position 240°.*
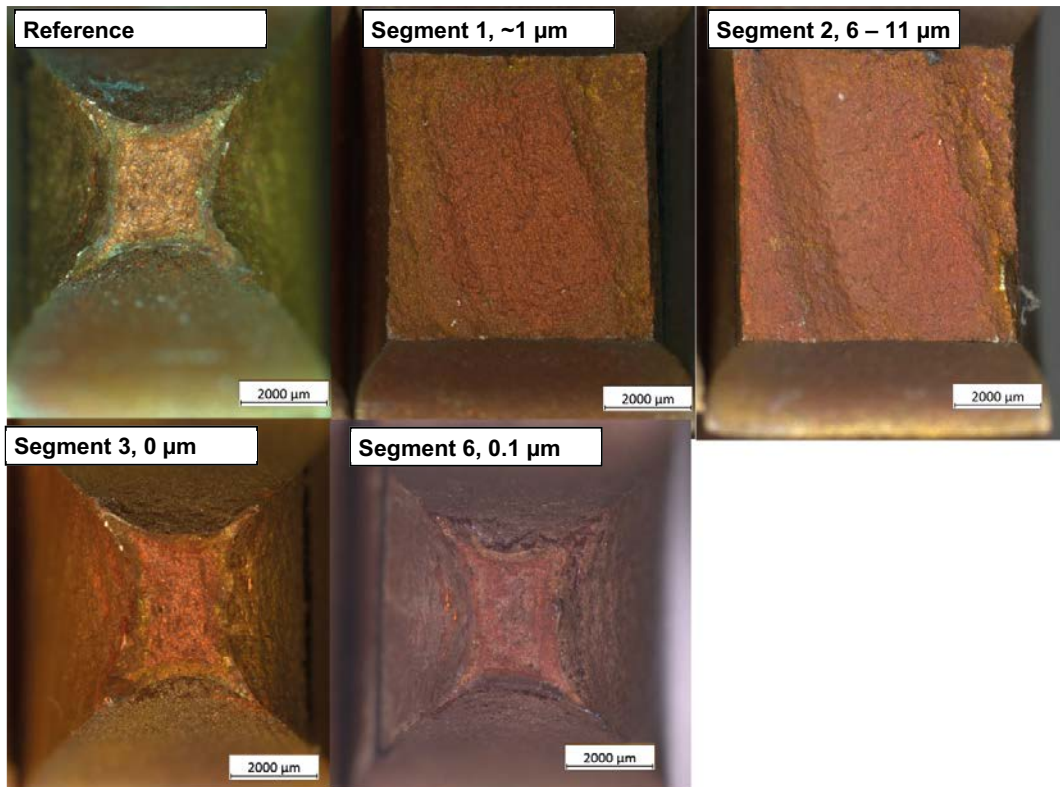
Figure 3-20. *Fracture surfaces of tensile test specimens tested at 175 °C. a) Reference, b) segment 1, position 197°, c) segment 2, position 156°, d) segment 3, position 101° and e) segment 6, position 238°.*
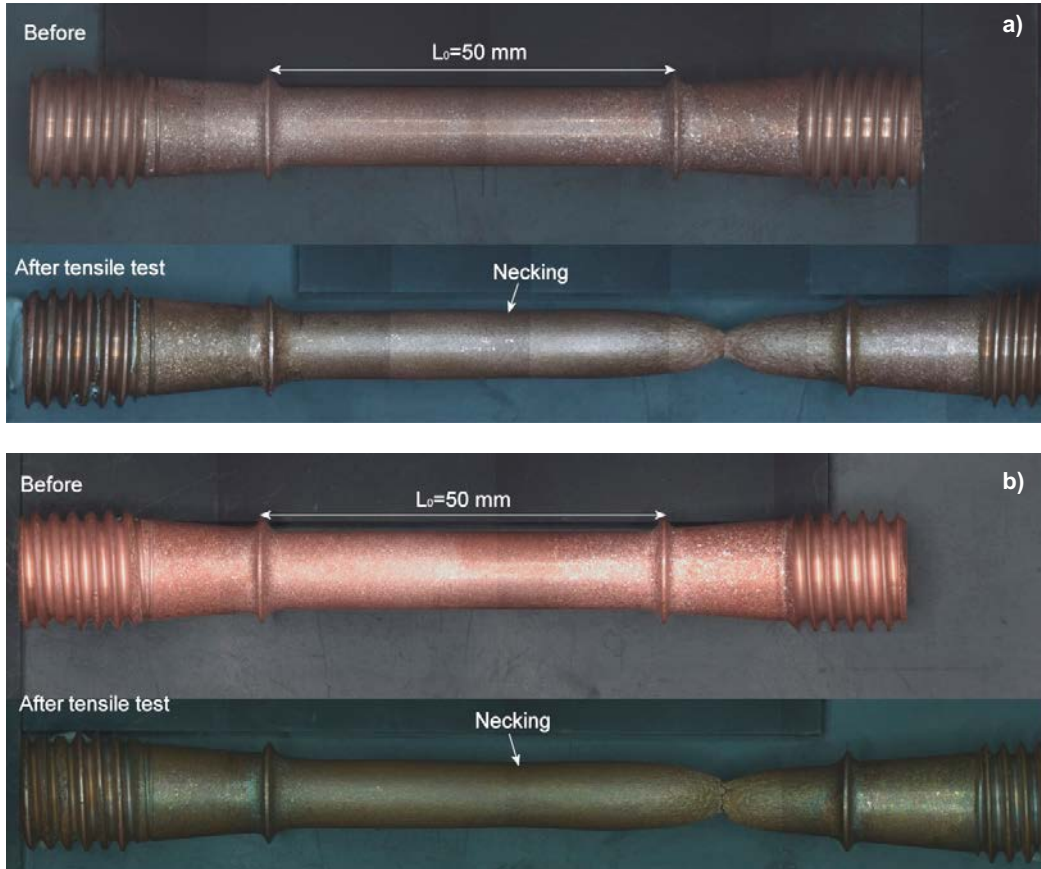

Figure 3-21. *Cross-weld tensile test specimens from segment 3 with 0 μm initial oxide layer thickness before and after hot tensile testing at a) 75 °C and b) 175 °C.*
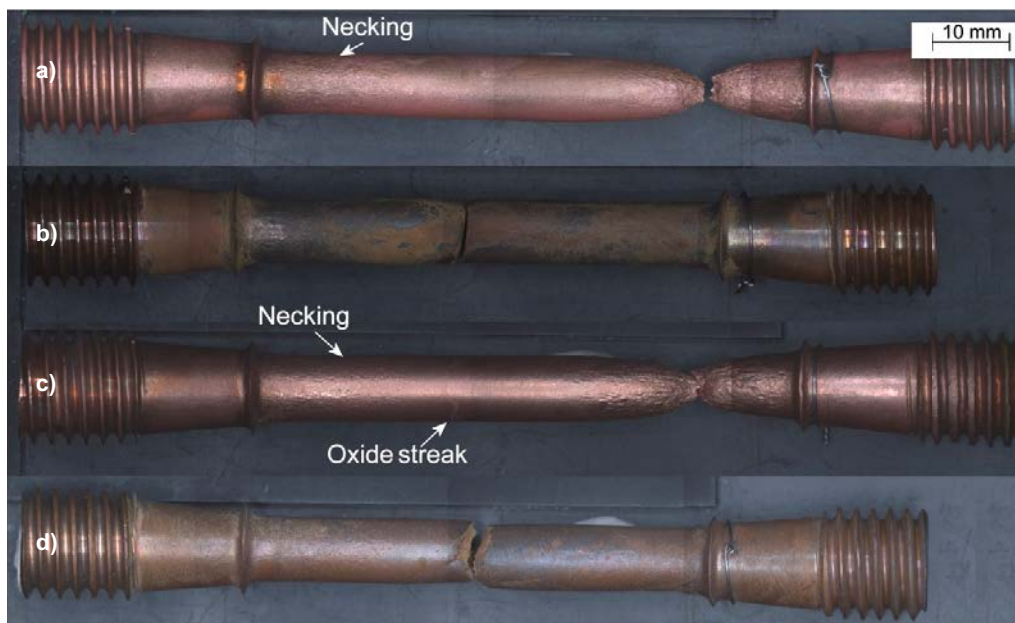
Figure 3-22. Cross-weld tensile test specimens from segment 1 and 2 with about 1 and 6–11 µm initial oxide layer thicknesses after hot tensile testing at a) segment 1, 75 °C, b) segment 1, 175 °C, c) segment 2, 75°C and d) segment 2, 175 °C.
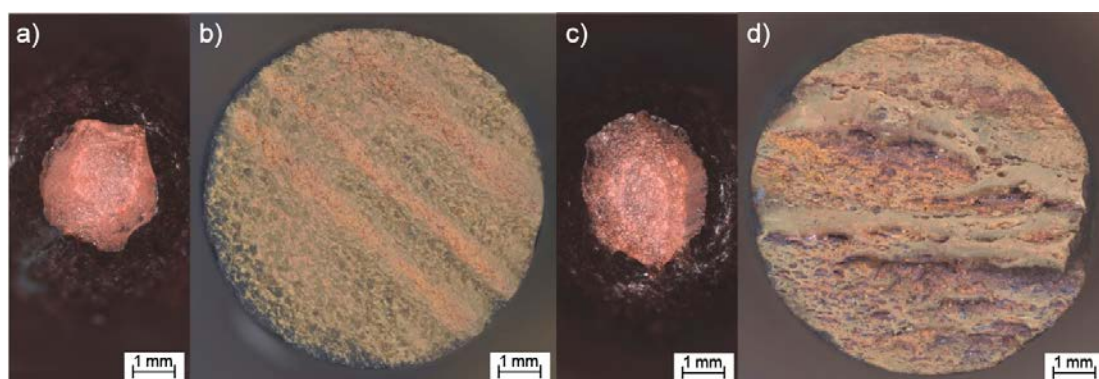

Figure 3-23. Fracture surfaces of cross-weld tensile test specimens from segment 1 and 2 with about 1 and 6–11 µm initial oxide layer thicknesses after hot tensile testing at a) segment 1, 75 °C, b) segment 1, 175 °C, c) segment 2, 75°C and d) segment 2, 175 °C.

3.2.3 Creep experiments

The results of creep tests at 75 °C are summarised in Table 3-4. Conventional creep data, i.e., creep strain as a function of time, is available for the cross-weld specimens only. This test data is shown in Figure 3-24. Time to rupture for all the creep test specimens is presented in

Figure 3-25 as a function of the nominal initial stress. The overall trends within the individual segments are mainly as expected. The reference specimen at the highest load of 175 MPa and the specimen from segment 3 at the lowest load of 135 MPa appear to have survived a shorter time than expected. Three of the specimens were interrupted prior to final failure either for metallography or due to machine problems.

As described above in Section 3.1.2, the specimens deform also in the gripping area as well as outside the 4 mm gauge section and thus the elongation values measured as a displacement of the loading rod are only indicative. Therefore, the primary parameter to compare the deformation behaviour and ductility of the different segments is the reduction of area also for these tests.

Table 3-4. Results of creep tests at 75 °C. At the time of writing this report, five creep tests were still running.

Segment	Oxide thickness obtained	Stress (MPa)	Time (h)	Specimen	Test name	Status	Reduction of area (%)	Comment
Lid (4)	Reference material	175	545	FSW113 41/4	FS475175	Finished	88	
		135	17 276	FSW113_4	FS475135	Running		
		155	15 387	FSW113_4	FS475155	Finished	63*	* Interrupted prior to final failure
1	~1 µm	155	169	FSW113 221/1	FS175155	Finished	47	
		135	181	FSW113 199,5/1	FS175140	Finished	50	
2	6–11 µm	175	100	FSW113 139/2	FS275175	Finished	43	
		155	425	FSW113 154/2	FS275155	Finished	42	
3	0 µm	175	1 949	FSW113 77/3	FS375175	Interrupted	58*	* Interrupted for metallography
		170	534	FSW113 76/3	FS375170	Finished	90	
		135	817	FSW113 85/3	FS375135	Interrupted	16*	* Interrupted for metallography
		155	2 106	FSW113 79.5/3	FS375155	Interrupted	32*	* Interrupted due to rig problem
		155	15 407	FSW113 65/3	FT375155	Running		
		115	1 077	FSW113 62/3	FS375115	Finished	80	
3 cross weld	0 µm	175	129	FSW113 64/3	FSW64175	Finished	89	
		155	9 642	FSW113 85/3	FSW85155	Running		
		135	9 473	FSW113 88/3	FSW88135	Running		
6	0.1 µm	175	288	FSW113 242/6	FS675175	Finished	91	
		155	2 346	FSW113 235/6	FS675155	Finished	64*	* Interrupted prior to failure
		135	7 867	FSW113 270/6	FS675135	Running		

As shown in Table 3-4, the reference specimen as well as the specimens from segments 3 and 6 with the lowest oxide content behave in a ductile manner and the area reduction is 80 % or greater. The specimens from segments 1 and 2 only reach an area reduction in the order of 40 to 50 %. The differences in ductility are also clear for the fracture surfaces presented in Figure 3-26 to Figure 3-28. The cross-weld creep test specimen presented in Figure 3-29 shows similar behaviour as the cross-weld tensile test specimens shown in Figure 3-21 with necking in another position along the gauge length except for the primary fracture.

Since the differences in ductility are large, the true stress state from the onset of necking to final failure differs between the segments with higher ductility (reference, segments 3 and 6) and the ones with a visible oxide streak (segments 1 and 2). Therefore the true stress prior to failure for the specimens with higher ductility is higher at the same nominal initial stress than for the specimens with lower ductility. If the true stress could be accounted for, the differences between the materials presented in Figure 3-25 would likely be more evident. For example, the true stress just a moment before the final failure is more than six times higher in the specimens from segments 3 and 6 than the true stress in specimen from segment 2 when all three were tested at the same nominal stress level of 175 MPa.
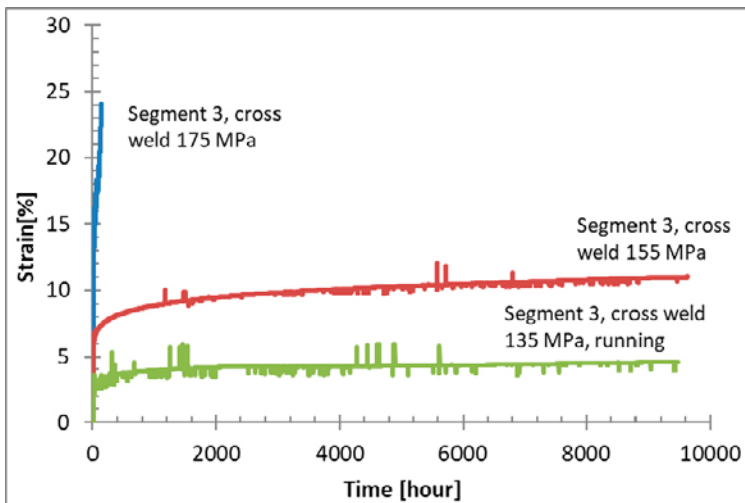

Figure 3-24. *Creep test data for the cross-weld specimen from segment 3 with 0 μm initial oxide layer thickness.*
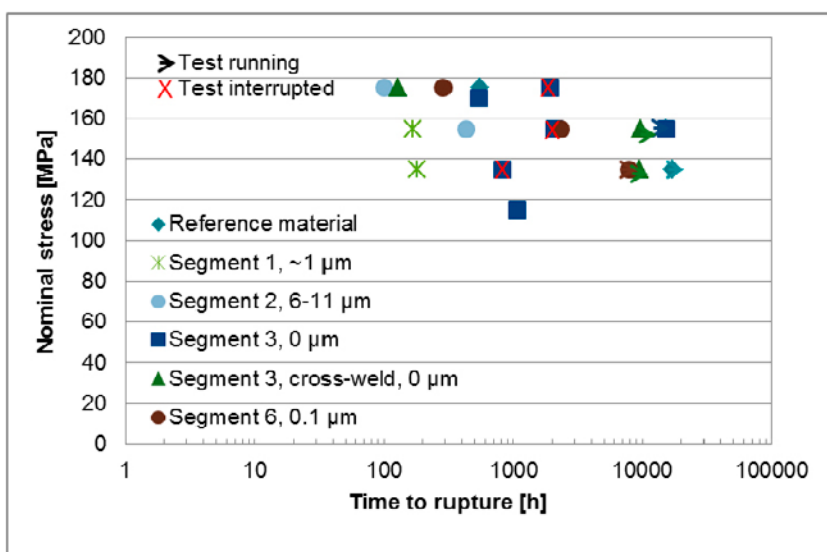

Figure 3-25. *Time to rupture vs. nominal initial stress in creep tests. A total of five tests are still running at the time of this report. The tests that were interrupted due to problems with the testing or prior to final failure for microscopy are marked with a red cross.*
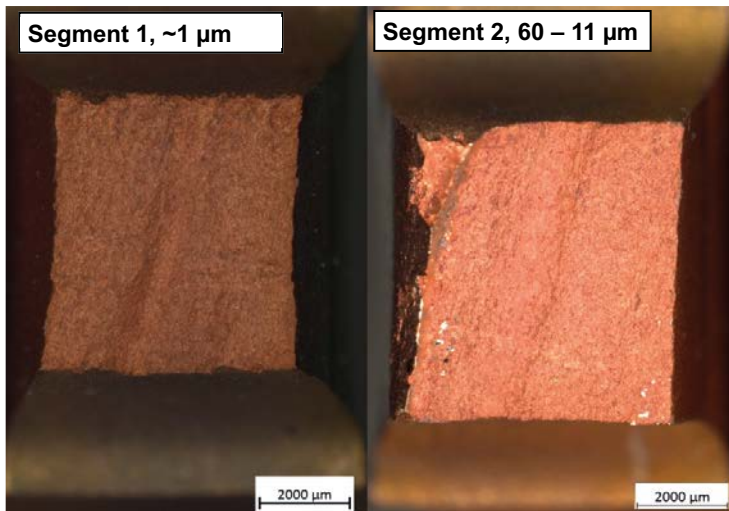
Figure 3-26. *Fracture surfaces of creep test specimens tested at 155 MPa and 75 °C. Time to failure for specimen from segment 1 (~1 μm) 169 h and for segment 2 (6–11 μm) 425 h.*
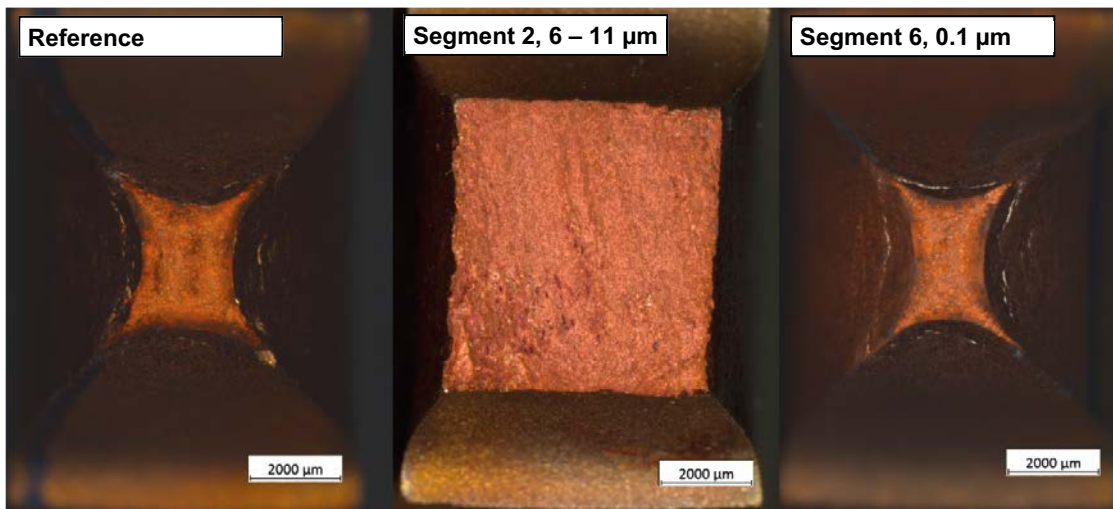

Figure 3-27. *Fracture surfaces of creep test specimens tested at 175 MPa and 75 °C. Time to failure for reference specimen 545 h, segment 2 (6–11 μm) 100 h and segment 6 (0.1 μm) 288 h.*
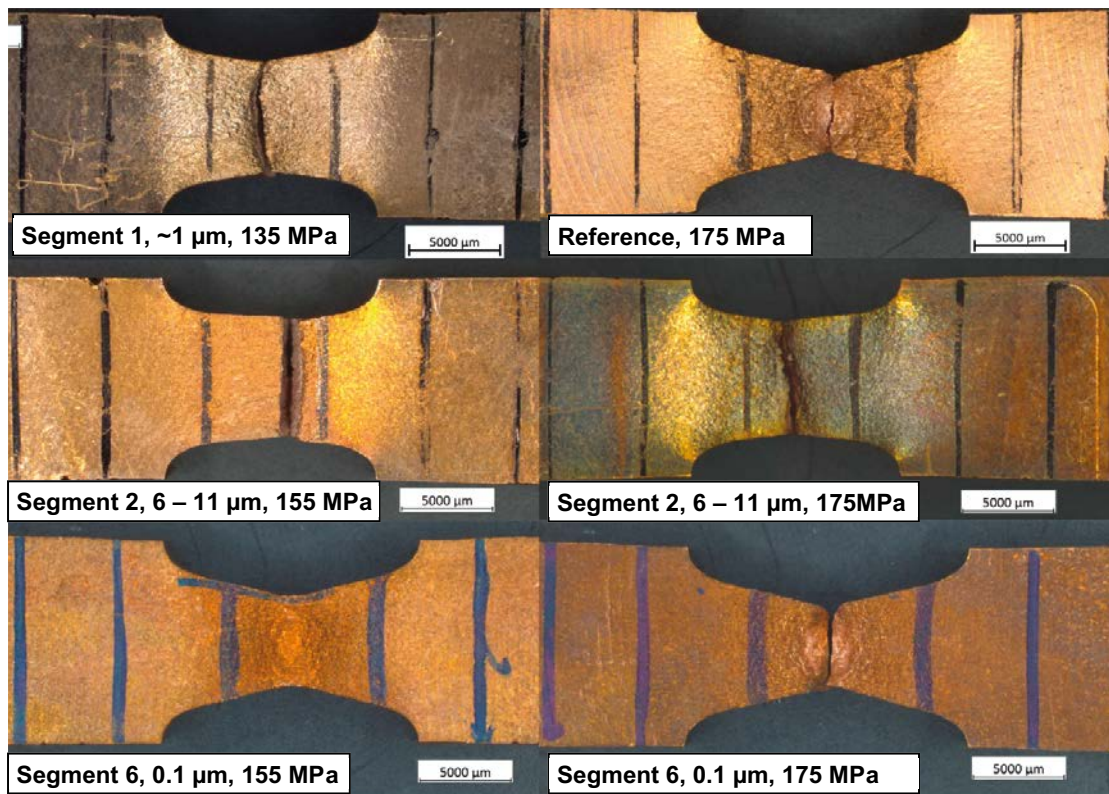
Figure 3-28. *Selected creep test specimens in axial direction, the specimens on the left are tested at a nominal stress of 155 MPa and the ones on the right at 175 MPa.*

Figure 3-29. *Cross-weld specimen from segment 3 (0 µm) before and after creep testing at 75 °C and 175 MPa, rupture time 129 h.*

3.2.4 Fractography

Fractography using scanning electron microscopy (SEM) was carried out for specimens from both hot tensile tests and creep tests. The results of fractography of the tensile test specimens from the reference and segments 1, 2 and 3 are shown in Figure 3-30 and Figure 3-31. The fracture surfaces, especially for the reference material and specimens from segment 3, are characterised by dimples indicating a ductile fracture. The fracture surfaces of specimens from segment 1 and 2 are also partly characterised by dimples as shown in the figures on the left. However, a closer look at the fracture surfaces (figures on the right) reveals large amounts of particles on the fracture surfaces. An EDS analysis of the particles confirmed that they consist to about 25 % at-% of oxygen and 75 at-% copper. The particles cannot be seen to the same extent on the fracture surfaces of the reference specimen or segment 3 and 6. Thus, the existence of these particles can be coupled to the lower ductility as presented above.

Fracture surfaces of cross-sections of selected creep test specimens also studied. The fractographs in Figure 3-32 and Figure 3-33 show essentially the same features as the hot tensile tests. The specimens from reference material, segments 3 and 6 show again large ductility whereas a great amount of particles can be observed on the fracture surfaces of the specimens from segments 1 and 2.
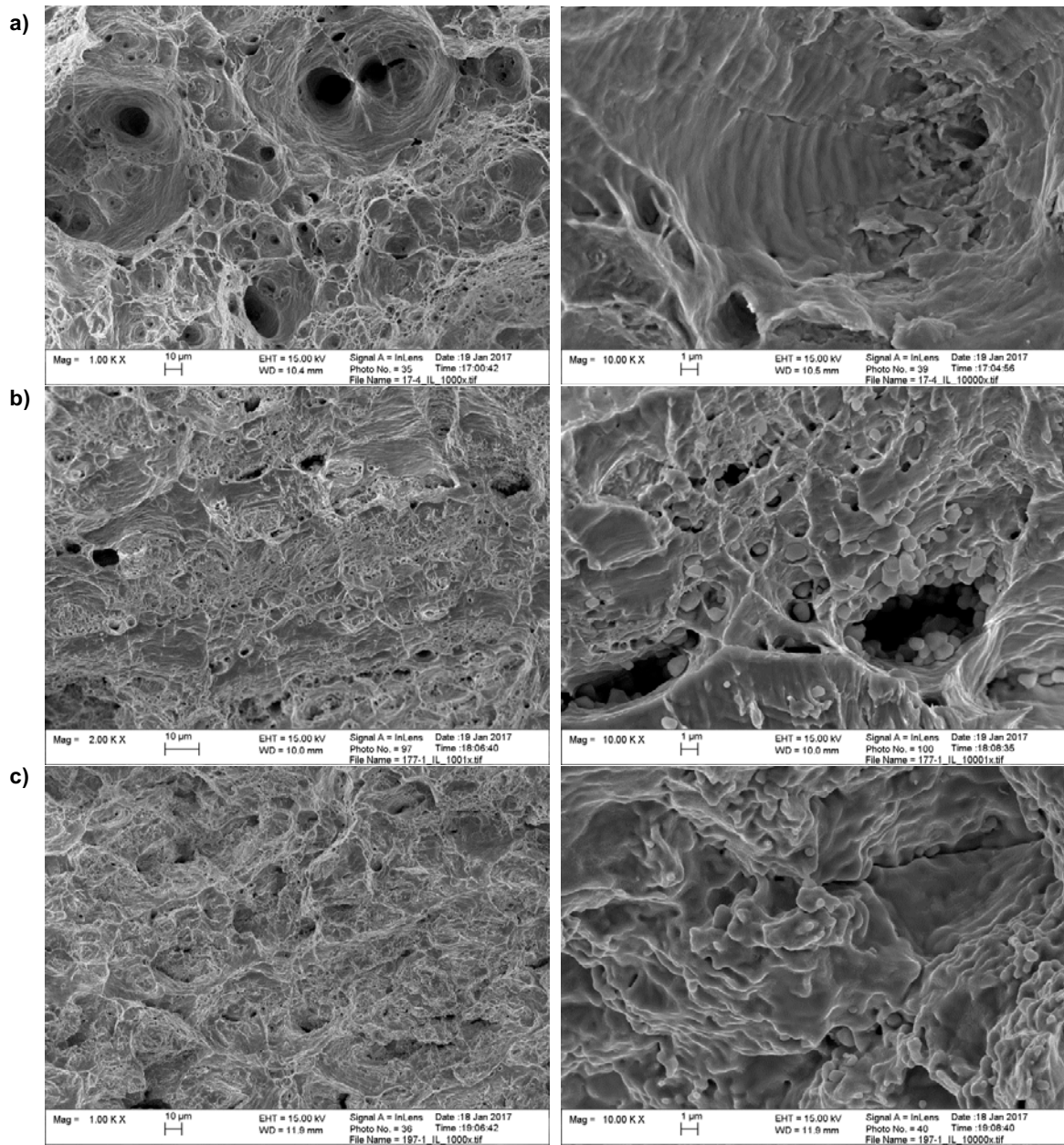

Figure 3-30. *Fracture surfaces of hot tensile specimens. A) reference tested at 75 °C, b) segment 1 (~1 μm) tested at 75 °C and c) segment 1 (~1 μm) tested at 175 °C. The fractographs on the right are with a higher magnification of the same area as the ones on the left.*
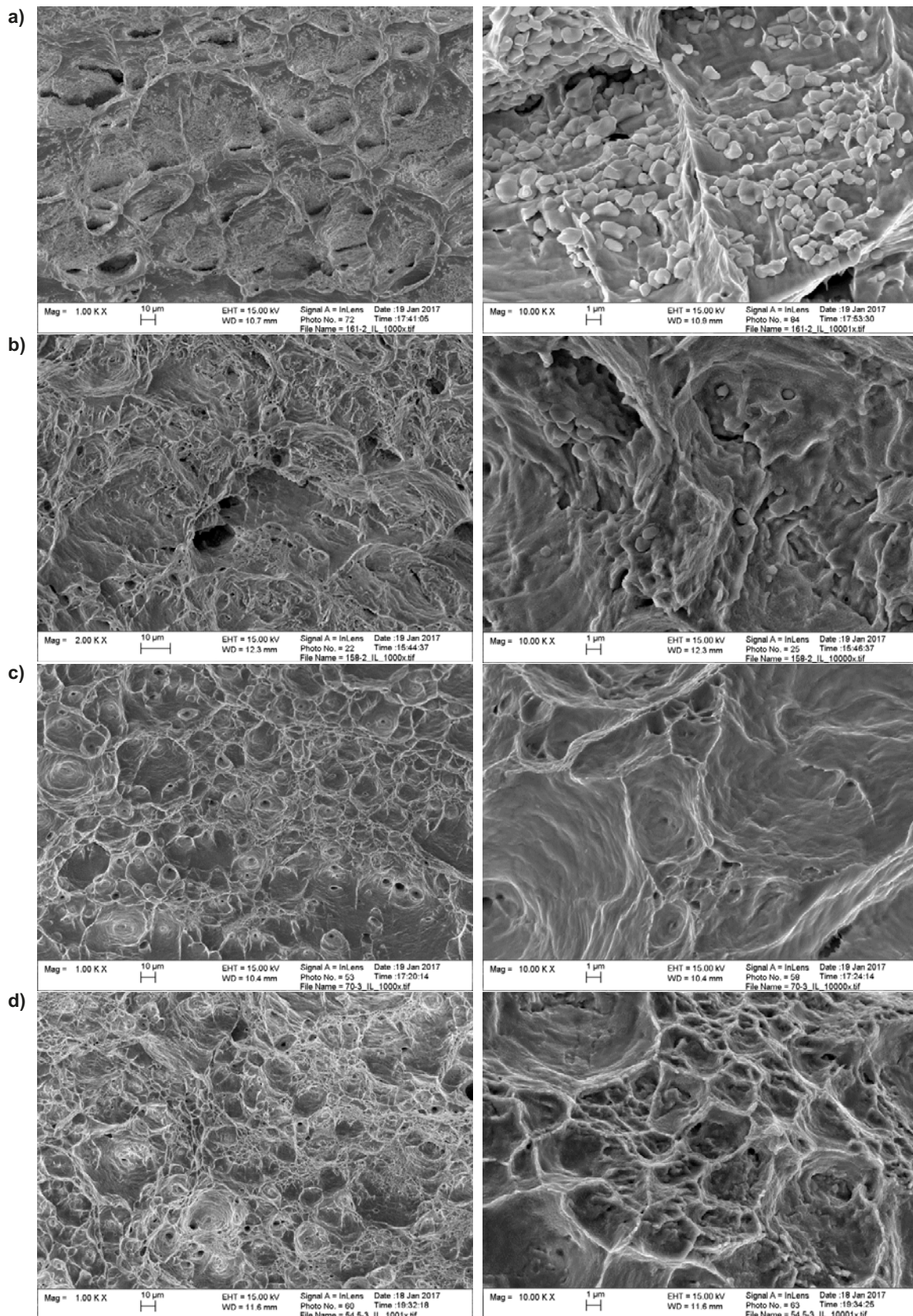
Figure 3-31. *Fracture surfaces of hot tensile specimens. A) segment 2 (6−11 µm) tested at 75 °C, b) segment 2 (6−11 µm) tested at 175 °C, c) segment 3 (0 µm) tested at 75 °C and d) segment 3 (0 µm) tested at 175 °C. The fractographs on the right are with a higher magnification of the same area as the ones on the left.*
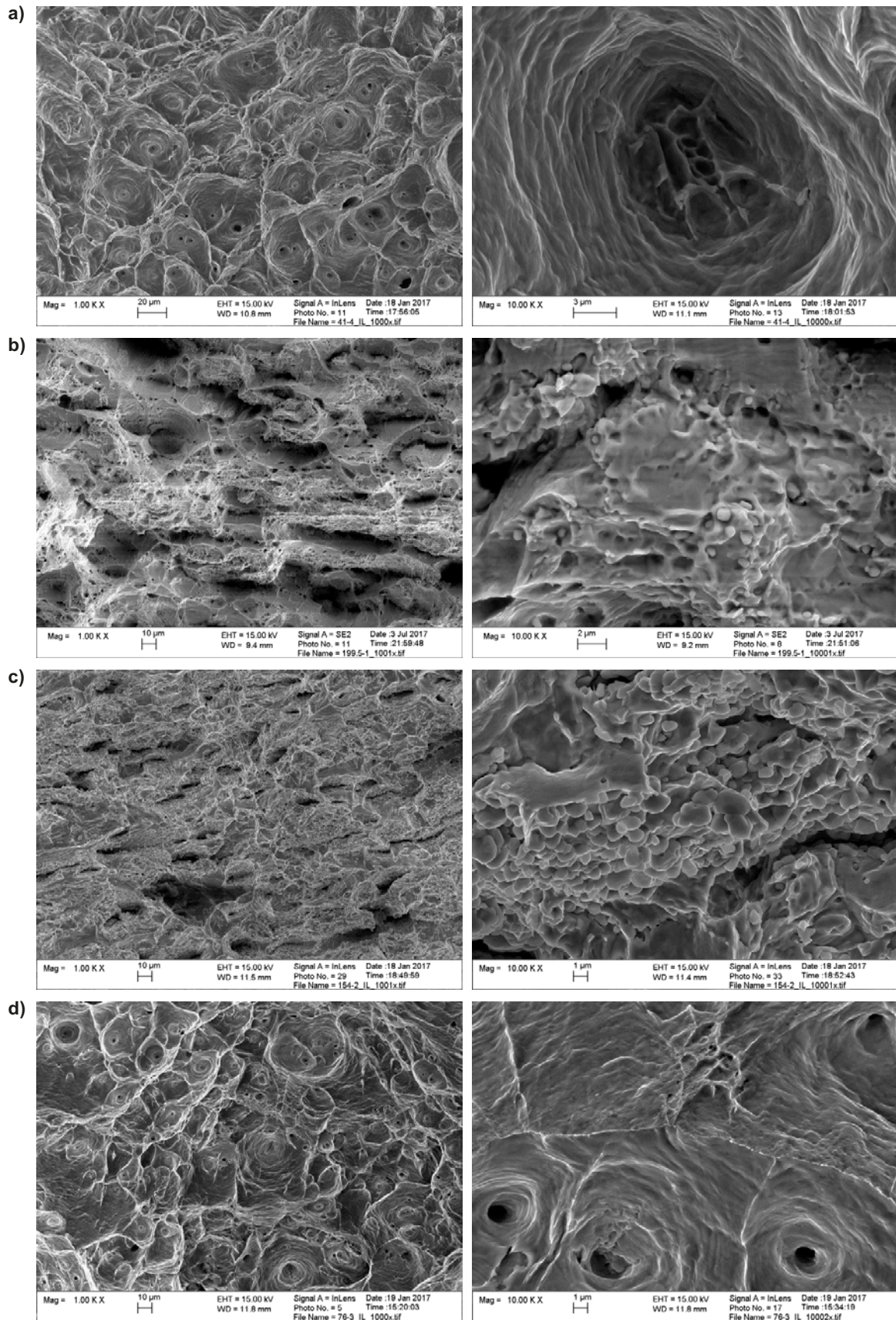
Figure 3-32. *Fracture surfaces of creep test specimens. A) reference tested at 175 MPa, time to rupture 545 h, b) segment 1 (~1 μm) tested at 135 MPa, 181 h, c) segment 2 (6–11 μm) tested at 155 MPa, 425 h and d) segment 3 (0 μm) tested at 170 MPa, 534 h. The fractographs on the right are with a higher magnification of the same areas as the figures on the left.*
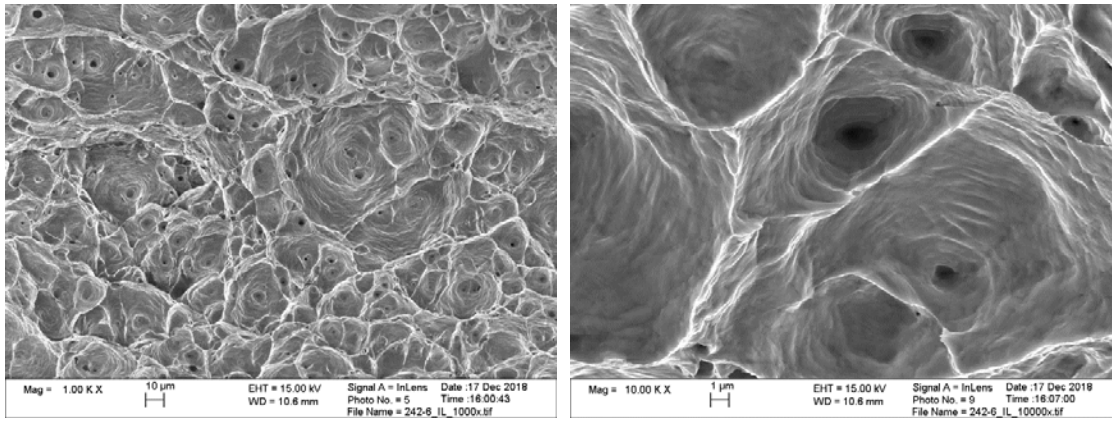
Figure 3-33. *Fracture surfaces of creep test specimen from segment 6 (0.1 µm) tested at 175 MPa, time to rupture 288 h. The fractograph on the right is with a higher magnification of the same area as the figure on the left.*

4 Corrosion properties

The oxide particle streaks that form during welding have a limited extension. Therefore it can be expected that the overall electrochemical potential will be rather uniform (in weldment). Nevertheless this is studied in Section 4.3 for two parts of the weld. In order to estimate corrosion behaviour of the oxide streaks a model for the dissolution of copper oxide in waters similar to the ground water is studied theoretically using both an analytical as well as a numerical model.

4.1 Analytical expressions for dissolution of oxide bands in copper

The chemical dissolution of copper oxide in waters with various chloride concentrations is studied theoretically. Analytical expressions of the dissolution rate are used in this section and results from a numerical model are presented in Section 4.2.

A numerical model allows many complicated relations to be represented simultaneously. However, the result is frequently not transparent to the reader and it may be difficult to ascertain whether results from a numerical model are reasonable. In order to increase the transparency of the results, an analytical treatment is given here as a complement to the numerical model.

4.1.1 Equilibrium concentrations of dissolved copper

Figure 4-1shows an illustration of a continuous oxide band that stretches from the outer wall of the canister, through the canister, to the inner wall.

The copper oxide is considered to be under dissolution according to Reaction 4-1.

$$Cu_2O(s) + 2n\ Cl^- + H_2O \rightarrow 2\ CuCl_n^{(n-1)-} + 2\ OH^- \tag{4-1}$$

Copper(I) forms a series of chloride complexes. In a solution with chloride concentrations in the order of 1.0 M, $CuCl_2^-$ and $CuCl_3^{2-}$ are the dominating forms of Cu(I) in solution.

If Reaction 4-1 is fast, a solubility equilibrium between Cu(I) in the solid and aqueous forms will establish. Figure 4-2 shows an equilibrium diagram from Puigdomenech and Taxén (2000). The diagram shows that the $CuCl_2^-$ complex is the most stable dissolved form of copper over a wide range of chloride concentrations. At concentrations slightly higher than 1.0 mol/kg H_2O ($Log[Cl^-]_{TOT}=0$), the $CuCl_3^{2-}$ complex is of equal stability and this complex dominates at higher chloride concentrations.
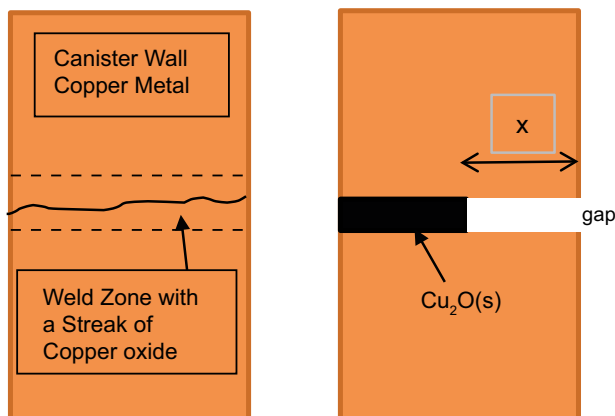

Figure 4-1. *Illustration of a continuous oxide band that stretches through the canister wall. The left hand figure shows the initial state and the right hand figure shows the idealized oxide band under dissolution.*

If we concentrate on chloride concentrations where the $CuCl_2^-$ complex dominates we can approximate the total concentration of dissolved copper with the expression for the concentration of the $CuCl_2^-$ complex in equilibrium with $Cu_2O(s)$.

Reaction 4-1 can be rewritten using hydrogen ions instead of hydroxide ions and only one half formula unit of $Cu_2O(s)$ can be considered, Reaction 4-2.

$$\frac{1}{2}\ Cu_2O(s) + 2\ Cl^- + H^+ \rightarrow CuCl_2^- + \frac{1}{2}\ H_2O \qquad (4\text{-}2)$$

Equation 4-3 shows an equilibrium condition for Reaction 4-2. Equation 4-3 is valid under the conditions that $Cu_2O(s)$ is present at unit activity and that activities of aqueous species can be approximated with concentrations,

$$\frac{[CuCl_2^-]}{[Cl^-]^2 \times [H^+]} = K \qquad (4\text{-}3)$$

The value of the equilibrium constant K is calculated from the free energy of formation through Equation 4-4 (Puigdomenech and Taxén 2000).

$$\ln K^\circ = -\frac{1}{RT} \sum_i \nu_i\ \Delta G_f^\circ(i) \qquad (4\text{-}4)$$

Table 4-1 shows the free energy of formation for the relevant chemical species.

Table 4-1. Free energies of formation for species participating in Reaction 4-2 (Puigdomenech and Taxén 2000).

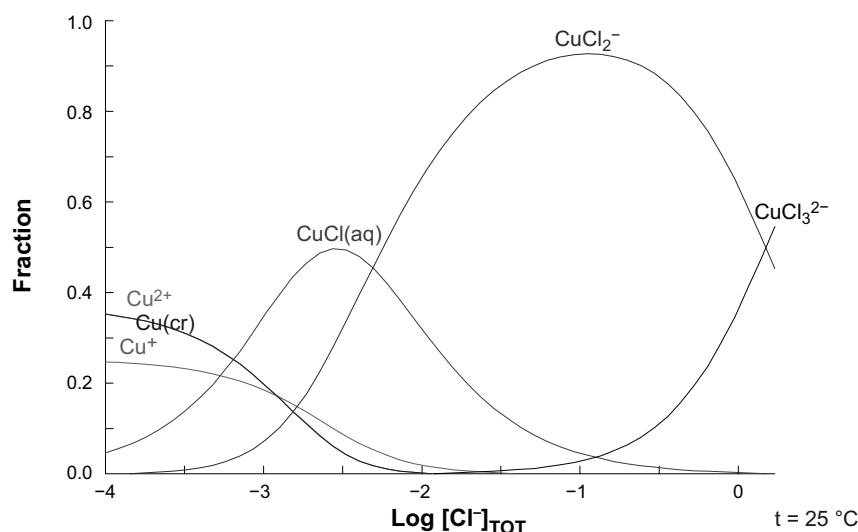|	G_f° (kJ/mol)	Coefficient in Reaction 4-2
$Cu_2O(s)$	−147.9	−0.5
H^+	0	−1
Cl^-	−131.2	−2
$CuCl_2^-$	−245.6	1
$H_2O(l)$	−237.1	0.5

Figure 4-2. *Equilibrium diagram. Fraction of copper(I) as chloride complexes: 25 °C. Diagram calculated for, $[Cu]_{TOT} = 10^{-5}$ mol/kg, and for $[Cl^-]_{TOT}$ between 10^{-4} and 1.7 mol/kg (Puigdomenech and Taxén 2000).*

Using Expression 4-4 and values of ν and G^o_f from Table 4-1, ln K is calculated as:

ln $K = -1/(8.314 \times 298) \times (-0.5 \times (-147.9) + (-1) \times 0 + (-2) \times (-131.2) + 1 \times (-245.6) + 0.5 \times (-237.1)) \times 1\,000$
ln $K = 11.22$

Finally the concentration of $CuCl_2^-$, can be calculated through Equation 4-5.

$$[CuCl_2^-] = e^{11.22} \times [Cl^-]^2 \times [H^+] \tag{4-5}$$

At 1.0 M chloride and pH 7, $[CuCl_2^-] \approx 7.5 \times 10^{-3}$ M.

4.1.2   The dissolution rate of oxide bands in copper

The right hand drawing in Figure 4-1 illustrates the state when the chemical dissolution of an oxide band has progressed a distance of x from the outer surface of the copper canister. We refer to the volume of previously dissolved copper oxide as the gap.

We will here assume that the conditions at the site of the oxide band immediately outside copper canister are constant. The local concentration of Cu(I) is close to zero and pH 7.

The flux of copper from the dissolving end of the copper oxide band to the mouth of the gap is determined by diffusion. The high end concentration, *Cmax*, is that determined by equilibrium with $Cu_2O(s)$ and the low end concentration is zero. The diffusion distance is denoted x.

If the value for the diffusion coefficient for $CuCl_2^-$ is denoted D, the total flux can be written:

$$j = D \times \frac{Cmax}{x} \tag{4-6}$$

$Cmax = [CuCl_2^-]$

The flux j is coupled to the dissolution rate of the copper oxide and thereby to the value of x.

$$\frac{dx}{dt} \left[\frac{m}{s}\right] = \frac{\frac{j}{2}\left[\frac{mole}{s \times m^2}\right] \times Mw\left[\frac{kg}{mole}\right]}{\rho\left[\frac{kg}{m^3}\right]} \tag{4-7}$$

Mw is the molar mass of Cu_2O
ρ is the density of Cu_2O
The flux j is divided by 2 because Cu_2O contains 2 copper atoms

Combining Equations 4-6 and 4-7 yields:

$$\frac{dx}{dt} = \frac{D \times Cmax \times Mw}{2 \times \rho \times x} \tag{4-8}$$

Rearranging gives Equation 4-9 that can be integrated from $x = 0$ at $t = 0$ which gives Equation 4-10.

$$x \times dx = \frac{D \times Cmax \times Mw}{2 \times \rho} \times dt \tag{4-9}$$

$$x^2 = \frac{D \times Cmax \times Mw}{\rho} \times t \tag{4-10}$$

Equation 4-11 gives the time, t, to dissolve a uniform band of $Cu_2O(s)$ to the depth, x.

$$t = \frac{\rho \times x^2}{Mw \times Cmax \times D} \tag{4-11}$$

4.1.3   The substance in the gap

In deriving expressions for the equilibrium concentrations of dissolved copper and for the diffusion rate in the gap it was implicitly assumed that there was an aqueous medium present in the gap. What is the medium in the gap after the $Cu_2O(s)$ has been dissolved? We find three possibilities.

1. *Water.* The capillary force of the gap would have to compete for water with the bentonite, which has a very high affinity for water.

2. *Bentonite.* Bentonite under pressure has a strong tendency to fill the available volume, particularly when the bentonite is in contact with liquid water. However, even bentonite particles have a finite size and may find that the gap width is too narrow.

3. *Nothing.* If there is no liquid water available and if the gap is too narrow to allow bentonite particles to enter the gap, further dissolution of the copper oxide band would seem impossible.

We treat these three cases as possible and try to estimate the time to perforation of a 5 cm thick copper wall by dissolving a continuous band of $Cu_2O(s)$.

Water in the gap

The basic composition of the water in the gap is assumed to be that of ground water. For a worst case, a ground water with high concentrations of chloride and carbonate is assumed. The role of chloride is obvious since chloride greatly increases the solubility of Cu_2O. However, the role of carbonate as a pH buffer is also important.

Reaction 4-2 consumes hydrogen ions and thus increases the local pH at the site of the reaction. An increased local pH decreases the solubility of the $Cu2O(s)$ and thus decreases the rate of diffusion of copper ions. But in water with high concentration of carbonate this tendency for pH increase will be counteracted by a buffering action. Carbonic acid diffusing inwards into the gap would be converted to hydrogen carbonate by the increased pH and diffuse outwards and be regenerated at the lower pH. At higher pH values, carbonate ions can also participate in the buffering action.

Equation 4-11 will be used to illustrate the calculated time for perforation of a 5 cm copper wall with a continuous band of $Cu_2O(s)$. The parameters used are:

Mw $= 0.143$ kg/mole Cu_2O
ρ $= 6\,000$ kg/m^3 Cu_2O
D $= 6 \cdot 10^{-10}$ m^2/s
x $= 0.05$ m

Table 4-2 shows the calculated times from Equation 4-11 with the highest dissolved copper concentration calculated from Equation 4-5. Several alternative pH values arising at the site of dissolution are considered. The pH values are typical for Forsmark ground waters, the chloride concentration 0.1 M could be regarded as a representative present-day value, while 0.5 M and 1 M represent more saline ground water (SKB 2011).

Table 4-2. Calculated values for the copper concentration at dissolving $Cu_2O(s)$ for various chloride concentrations and pH values at the site of dissolution. The estimated time to dissolve Cu_2O to a depth of 5.0 cm is also shown. The concentration, Cmax, is approximated as that of the $CuCl_2^-$ complex which is the dominating form of dissolved copper in the present range of chloride concentrations. Diffusion in water is considered.

[Cl⁻] (M)	Local pH	Cmax (M)	t (s)	t (years)
0.1	7.0	7.5×10^{-5}	2.3×10^{12}	74 304
0.5	7.0	1.9×10^{-3}	9.4×10^{10}	2972
1.0	7.0	7.5×10^{-3}	2.3×10^{10}	743
0.1	7.5	2.4×10^{-5}	7.4×10^{12}	234 970
0.5	7.5	5.9×10^{-4}	3.0×10^{11}	9399
1.0	7.5	2.4×10^{-3}	7.4×10^{10}	2350
0.1	8.0	7.5×10^{-6}	2.3×10^{13}	743 042
0.5	8.0	1.9×10^{-4}	9.4×10^{11}	29 722
1.0	8.0	7.5×10^{-4}	2.3×10^{11}	7430

Results from the numerical model indicate that the pH at the site of dissolution would be approximately pH 7.4 in water with 1.0 M chloride and 10 mM carbonate ($[H_2CO_3]+[HCO_3^-]+[CO_3^{2-}]$). From Table 4-2 it is found that 5 cm of $Cu_2O(s)$ could be dissolved in roughly 2 350 years at a pH of 7.5 at the dissolution site. This is in fair agreement with numerical model results of about 2 300 years at a pH of 7.4 at the dissolution site.

Bentonite in the gap

The diffusivity of the negatively charged species, Cl^-, $CuCl_2^-$ and HCO_3^- in bentonite is two orders of magnitude lower than the diffusion coefficients in water. A value of that magnitude seems reasonable for the effective diffusion coefficient of chloride ions in bentonite and water, respectively (Leroy et al. 2006). Equation 2-11 predicts that the time for dissolution to a given depth is inversely proportional to the value of the diffusion coefficient. This would imply that the times for perforation in Table 2-2 could be increased by the same factor. However, the pH at the site of dissolution is likely to become less alkaline with bentonite in the gap than with water in the gap. Bentonite carries with it a certain buffer capacity[1] which would be transported in the gap through a different mechanism than diffusion.

The net result is probably that of lower dissolution rate than in water but higher than that indicated by the lower diffusion coefficient.

Nothing in the gap

If there is no liquid water available and if the gap is too narrow to allow bentonite particles to enter the gap, further dissolution of the copper oxide band would seem impossible.

Physical contact between a grain of copper oxide and a grain of bentonite would enable dissolution of some copper oxide in the pore water of the bentonite and thus cause the copper oxide boundary to retreat. If the bentonite boundary does not move but the copper oxide boundary retreats, physical contact would eventually be lost. Only gases in equilibrium, or near equilibrium, with the wet bentonite would occupy the space between copper oxide and bentonite. For some gap width the bentonite may be squeezed into the gap to a certain distance but eventually loose contact with the retreating front of dissolving copper oxide so that dissolution stops.

4.2   Numerical model for the dissolution of oxide bands in copper

The model geometry used is the same as that illustrated in Figure 4-1 for the analytical expressions in the previous section. The numerical treatment allows the chemical system to be treated in deeper detail than possible using analytical expressions.

Copper(I) oxide dissolution takes place in contact with aqueous solution. There are a number of homogeneous reactions in the vicinity of the oxide affecting the rate of dissolution.

A diluted electrolyte modeling approach incorporating a system of reactions is used to investigate the weld stability over time.

In order to account for the possibility of different geometries of the oxide bands, and consequently the gap resulting from dissolution, we considered both a linear dissolution model and a wedge shaped model which is wider at the opening towards the outer canister surface. The latter could possibly lead to more rapid dissolution.

---

[1] The continued dissolution of Cu_2O increases the pH, locally. Figure 4-4 shows that the dissolution rate is higher with 10 mM total carbonate than with 1 mM total carbonate concentration. This is an effect of the buffering property of carbonate that limits the increase in pH due to the dissolution. Bentonite probably has a similar buffering effect so that bentonite that is pressed into the gap undergoes partial ion exchange. H^+ replacing Na^+ in bentonite and Na^+ replacing H^+ in the water.

4.2.1 Theory

Reactions

The complete reaction system together with the equilibrium constants at 25 °C is given below. All equilibrium constants were calculated from Puigdomenech and Taxén (2000).
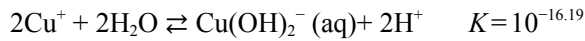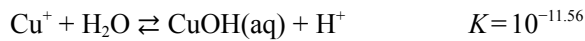
Copper(I) oxide dissolution is driven by the following equilibrium reaction present in aqueous solution:
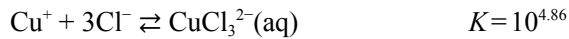
$$2Cu^+ + H_2O \rightleftarrows Cu_2O(s) + 2H^+ \qquad K_S = 10^{1.49}$$
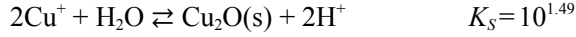
The solution contains carbonates in the form of carbonic acid, bicarbonate, and carbonate in equilibrium:

$$H_2CO_3 \rightleftarrows H^+ + HCO_3^- \qquad K = 10^{-3.90}$$

$$HCO_3^- \rightleftarrows H^+ + CO_3^{2-} \qquad K = 10^{-10.33}$$

The dissolved copper(I) ions form hydroxides as followed:

$$Cu^+ + H_2O \rightleftarrows CuOH(aq) + H^+ \qquad K = 10^{-11.56}$$

$$2Cu^+ + 2H_2O \rightleftarrows Cu(OH)_2^- (aq) + 2H^+ \qquad K = 10^{-16.19}$$

Aqueous copper(I)-chloride complexes are formed in the following manner:

$$Cu^+ + Cl^- \rightleftarrows CuCl(aq) \qquad K = 10^{3.30}$$

$$Cu^+ + 2Cl^- \rightleftarrows CuCl_2^-(aq) \qquad K = 10^{5.62}$$

$$Cu^+ + 3Cl^- \rightleftarrows CuCl_3^{2-}(aq) \qquad K = 10^{4.86}$$
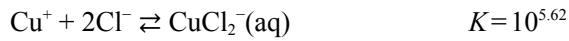
4.2.2 Model

The rate at which the weld thickness decreases is modeled. This is done for a 1D geometry representing an initial 1 μm crevice that grows as the weld dissolves. In the geometry, one boundary equals the Cu_2O surface and the other the bulk-crevice interphase. Consequently, this 1D representation models the situation at which the transport of species between the reacting site and the bulk is inhibited by the shape of the crevice to the least possible extent.

Mass transport in the solution is described by diffusion alone. Electromigration of charged species is neglected since no electrochemical reactions are considered and the diffusion potentials are likely to be small. Under these conditions the flux j for species i is described by Expression 4-12.

$$j_i = -D_i \frac{\partial C_i}{\partial x} \tag{4-12}$$

The fluxes for four total concentrations are summed up using the species concentrations and their dependence of the component concentrations. Copper ions undergo a number of reactions primarily with chloride ions to form complex dissolved species. When the diffusion rate is calculated it includes dissolved copper in all its forms. Likewise, in order to correctly compute the effect on the local pH the transport of acidity in all its forms is included. The total concentrations are based on proton, copper ion, carbonate, and chloride containing species:

$$[H^+]_{Total} = [H^+] - [OH^-] - [CO_3^{2-}] + [H_2CO_3] - [CuOH] - 2[Cu(OH)_2^-] \tag{4-13}$$

$$[Cu^+]_{Total} = [Cu^+] + [CuOH] + [Cu(OH)_2^-] + [CuCl] + [CuCl_2^-] + [CuCl_3^{2-}] \tag{4-14}$$

$$[CO_2(aq)]_{Total} = [CO_3^{2-}] + [HCO_3^-] + [H_2CO_3] \tag{4-15}$$

$$[Cl^-]_{Total} = [Cl^-] + [CuCl] + 2[CuCl_2^-] + 3[CuCl_3^{2-}] \tag{4-16}$$

The model system solves four mass balances for each total concentration over the model geometry. The mass balances have the following form:

$$\frac{\partial C_i}{\partial t} = -\frac{\partial}{\partial x}(j_i) \tag{4-17}$$

The reaction source is incorporated by solving for the speciation of the total concentrations (Equation 4-13 to 4-16).

Constant total concentrations are set at the outer boundary of the crevice and at the weld surface a flux is set representing the dissolution reaction, defined as:

$$N_i = k_{diss}\left(1 - SI_{Cu_2O(s)}\right)$$

(4-18)

where k_{diss} is the rate of dissolution and SI is the computed solubility index of the copper oxide (≤ 1).

The activity coefficients for charged species are estimated for the local ionic strength, I, according to Davies' model (Stumm and Morgan 1981):

$$\log \gamma_i = -0.51 \cdot z_i^2 \left(\frac{\sqrt{I}}{1 + \sqrt{I}} - 0.2 \cdot I\right) \quad \text{where} \quad I = 1/2 \cdot \sum z_i^2 \cdot C_i$$

(4-19)

The ionic strength includes the concentration of sodium-ions which is computed from the electro-neutrality condition.

4.2.3 Model results, linear dissolution

The geometry for linear diffusion is illustrated in Figure 4-3. Copper oxide is considered to be dissolved from left to right in the figure. The outer surface of the copper canister is located at x-coordinate zero and the inner surface is located at x-coordinate 0.05 m. A stage where the dissolution has almost reached 5.0 cm which would lead to perforation of a canister is illustrated.

Figure 4-4 shows a diagram with the depth of penetration is plotted versus time for various compositions of the bulk water. The diagram shows that higher chloride concentrations and higher carbonate concentrations result in shorter times to dissolve an oxide band to a certain depth. The worst case in Figure 4-4, 1.0 M chloride and 10 mM carbonate, could lead to perforation of 5 cm in about 2 300 years.

4.2.4 Model results, wedge formed oxide band

Figure 4-5 illustrates the growth mode for a wedge shaped oxide band. The wedge is 20 mm at the outer surface of the canister and 5 mm at the inner surface. The model volume, a short time before penetration to 50 mm, is color coded after the local pH. A wedge shaped oxide band is found to lead to higher maximum dissolution rates than oxide bands of constant widths. The calculated depth of penetration as function of time is shown in Figure 4-6. Figure 4-6 includes two types wedge formed oxide bands and the linear growth mode is included for comparison.
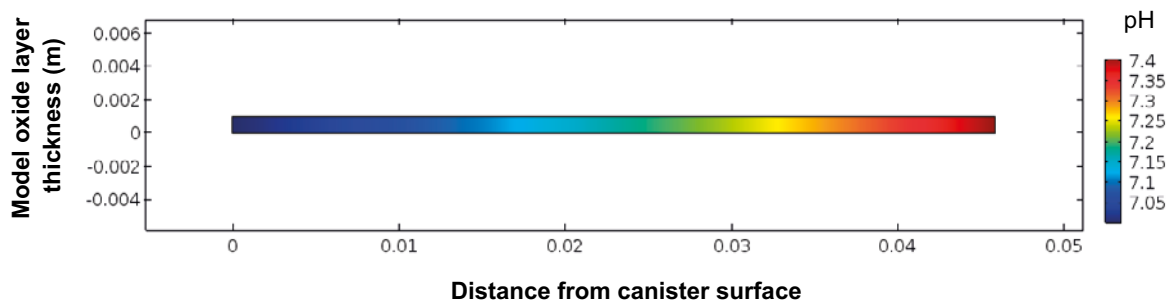

Figure 4-3. *Growth mode of the gap resulting from dissolution of a linear oxide band. The oxide dissolves from the left to the right, the right hand boundary of the model grows. The model volume (volume of the previously dissolved Cu_2O), a short time before penetration to 50 mm, is color coded after the local pH.*
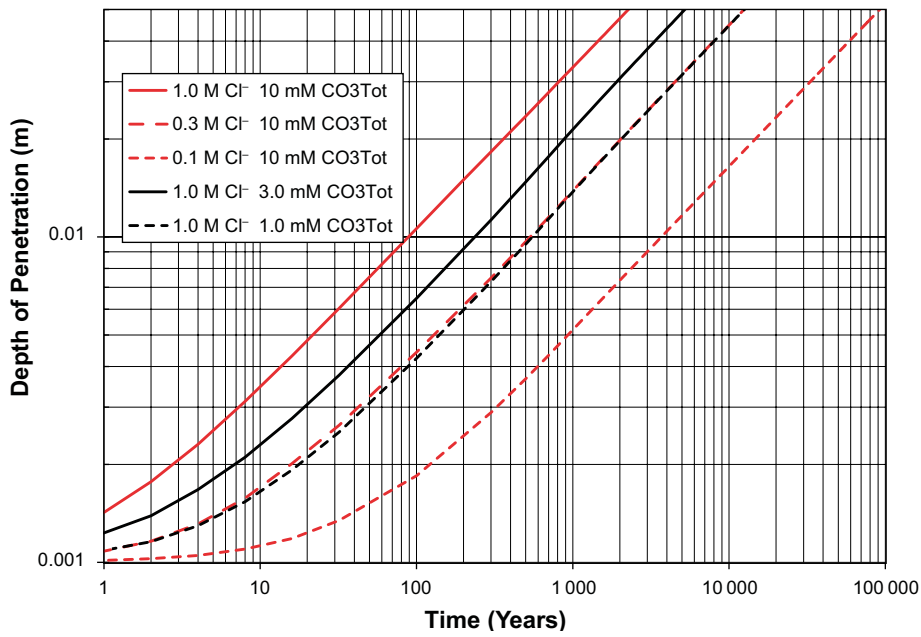
Figure 4-4. Depth of penetration as function of time for linear dissolution in solutions containing various concentrations of chloride and carbonate.
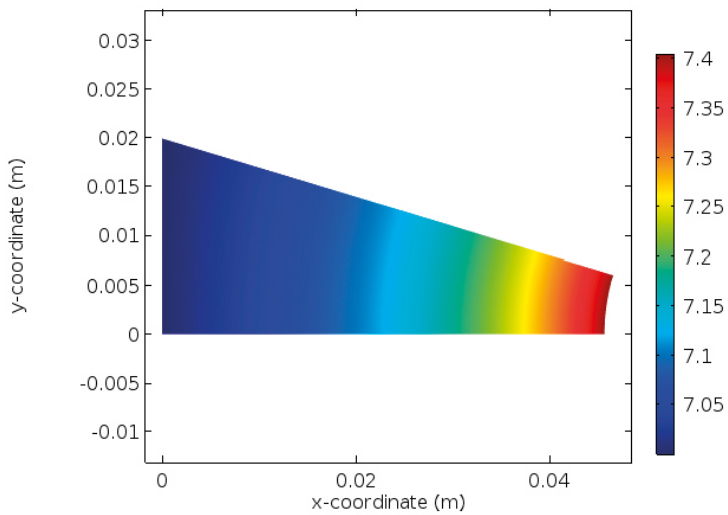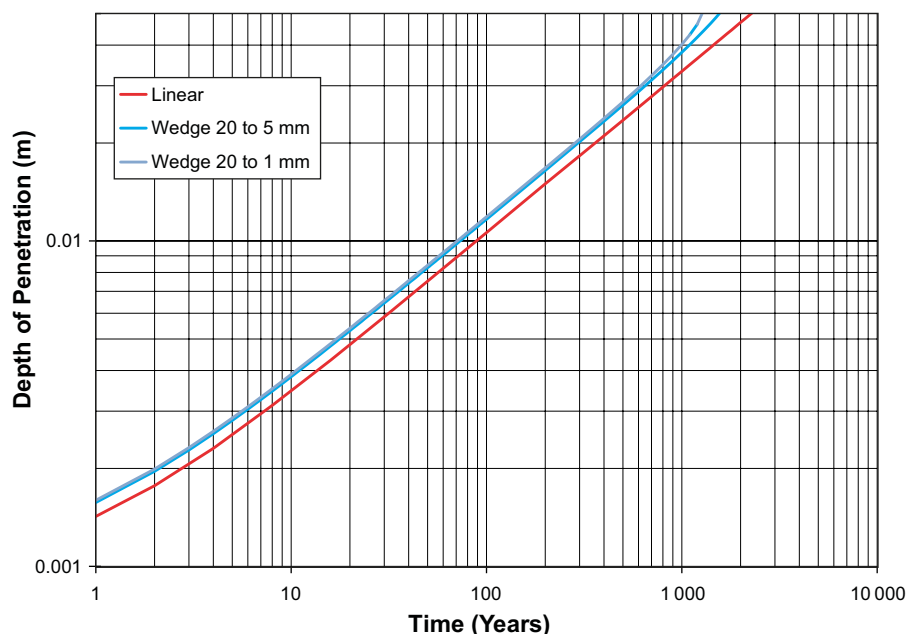

Figure 4-5. Growth mode for a wedge shaped oxide band. The wedge is 20 mm at the outer surface of the canister and 5 mm at the inner surface. The model volume, a short time before penetration to 50 mm, is color coded after the local pH.

Figure 4-6. *Depth of penetration as function of time for a solution of 1.0 M chloride and 10 mM total carbonate. Two alternative wedge shapes of the oxide band are shown. The growth mode for linear oxide band is included for comparison.*

4.2.5 Model results summary

Table 4-3 summarizes the conditions that arise at the dissolving copper oxide for various compositions of the water outside the canister.

A wedge shaped oxide band could dissolve faster than the linear bands considered in Table 4-3. A wedge shape 20 mm at the outer surface of the canister and 1 mm at the inner surface could perforate 5.0 cm after about 1 270 years, compared to 2 271 years for linear dissolution.

Table 4-3. Calculated values for the copper concentration and pH at dissolving Cu₂O(s) for various chloride concentrations and total carbonate concentrations in the bulk. The estimated time to dissolve Cu₂O to a depth of 5.0 cm is also shown. The bulk pH is set to 7.0. Linear dissolution.

[Cl⁻]bulk (M)	[CO₃]²⁻Tot, bulk (mM)	pH Max	[Cu(I)]Max (mM)	t (years)
1.0	10	7.41	2.44	2 271
0.3	10	7.06	0.45	12 479
0.1	10	7.01	0.06	91 988
1.0	3.0	7.76	1.07	5 215
1.0	1.0	8.15	0.44	12 537

4.3 Experimental

The apparent electrochemical nobility of welded copper is estimated by measurements of equilibrium potentials in solutions of varying copper concentrations (Taxén and Sparr 2014). Gubner and Andersson (Gubner and Andersson 2007) studied corrosion potentials in similar experiments on copper, with and without welds, but without additions of copper ions.

4.3.1 Material

The material was supplied by Matts Björck (SKB). All test pieces were labelled FSW113. Individual labels were 112/2, Figure 4-7a, 52/3, Figure 4-7b and 172/1, Figure 4-7c. *A* for Advancing in Figure 4-7 indicates the side of the weld where the movement of the friction stir weld tool has the same direction as the rotation of the tool. The local relative velocity between the tool and the copper is higher at point *A* than it is at point *R* (*R* for Retreating) where the movement of the tool and the direction of the rotation oppose one another.

Figure 4-8 shows an image of a friction stir weld where there is a band visible in lighter colour than the weld material. Close inspection of Figure 4-7 shows that this band is visible also after polishing.
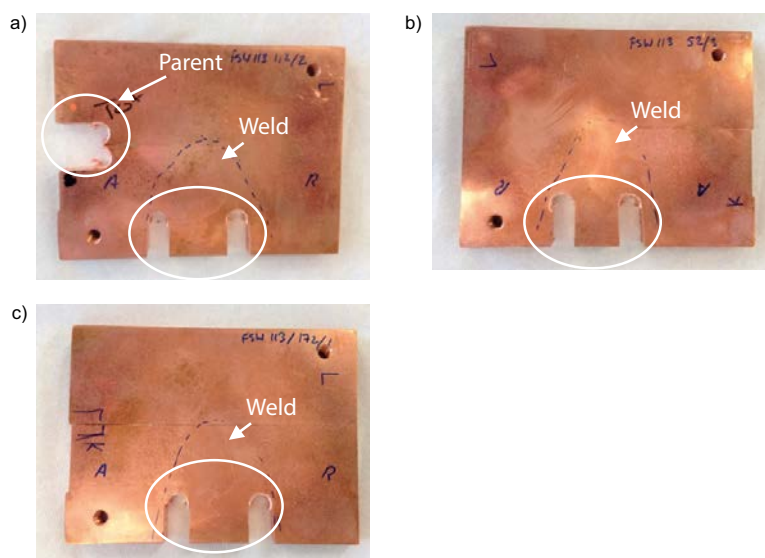
Figure 4-7. *Photographs of copper plates showing where samples (circled) were cut from material 112/2 (a), 52/3 (b) and 172/1 (c), leaving the empty spaces seen in the pictures. Regions within dashed lines drawn on the plates mark weld location and tool rotation direction is indicated by the letters A (advancing) and R (reversing) adjacent to the weld.*
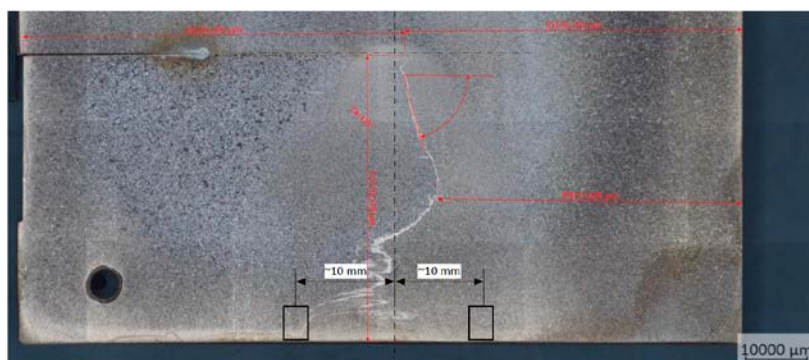
Figure 4-8. *Image of a friction stir weld before polishing. The contour of the weld is visible and a narrow light band close to the centre line of the weld. The black squares shows the approximate location of the samples.*

4.3.2 Electrodes

Duplicate rectangular rod specimens were cut from the copper plates described above, with approximate dimensions of 10 mm diameter length, 5 mm height and 4 mm width.

In order to make electrical contact with the copper samples, sheathed wire (peeled at the ends) was run through holes drilled at the ends of the rod specimens. The wire was eventually fixed to the specimens by conductive epoxy (Conductive Epoxy CW2400, Chemtronics). The samples were then cold mounted in a two component epoxy resin (Epofix, Struers). Each mount contained the duplicate samples (electrically insulated) from each material, i.e. 4 specimens/mount. Each specimen had an area of approximately 0.2 cm^2 in contact with the solution.

The electrodes were labelled #1−16. The labelling is clarified in Table 4-4.

Table 4-4. Clarification of electrode designations.

Electrode Number	Weld Direction	Material
1	Parent	
2	Parent	112/2
3	Parent	
4	Parent	
5	Advancing	
6	Advancing	112/2
7	Retreating	
8	Retreating	
9	Advancing	
10	Advancing	172/1
11	Retreating	
12	Retreating	
13	Advancing	
14	Advancing	52/3
15	Retreating	
16	Retreating	

4.3.3 Performance

The experiments were carried out in a glass cell with a volume of approximately 1 L. A supporting electrolyte consisting of 0.5 M MgSO$_4$ at pH 2.5 was selected. This solution was selected to allow minor differences in the corrosion properties of the metal itself to manifest and not be clouded by solid corrosion products forming at the surface. Nitrogen gas was continuously bubbled through the test solution. The nitrogen gas came from the building's central gas system which is fed by nitrogen gas of quality Instrument 5.0, AGA. All additions during the course of the experiments were, however, made using solutions not previously de-aerated.

4.3.4 Equilibrium potentials for the copper materials

In order to measure how noble or un-noble the different copper materials behave, the electrodes' potential in solution were measured relative to a reference electrode of saturated calomel (SCE).

All potentials were measured using a potentiostat: Solartron Electrochemical Interface 1286. Before and after each experiment, the potential of the reference electrode was measured relative to a similar electrode that is always kept in saturated KCl. The difference was always less than 1 mV, confirming that the reference electrode remained accurate and was not affected by the measurements made.

The copper content in the solution was increased by successive additions of a stock solution of 0.5 M CuSO$_4$ to the supporting electrolyte. Decreasing concentrations were achieved by withdrawing a volume of the test solution and replacing with the supporting electrolyte, 0.5 M MgSO$_4$.

4.3.5 Surface morphology after forced corrosion

Accelerated corrosion was carried out for half of the duplicate electrodes from the different copper samples (8 electrodes in total) in 0.5 M $MgSO_4$ solution at pH 2.5. The electrodes were corroded simultaneously by applying a constant anodic current of 0.630 mA. Based on an electrode area of approximately 0.2 cm^2/specimen, the average current density was about 0.394 mA/cm^2 for each of the 8 parallel samples. The time of the galvanostatic polarization was set to 192 hours so that the average corrosion depth would be 0.1 mm.

Figure 4-9 illustrates the principle for galvanostatic polarization of several electrodes simultaneously. The use of serial resistors, 160 kΩ, ensures that that an equal part of the total current is fed to each electrode.

After forced corrosion to 0.1 mm average depth the electrodes were imaged by confocal microscopy in order to study the shape of the corrosion attack and the morphology of the surface.

4.4 Experimental results

Figure 4-10, *a* through *d* and Figure 4-11, *a* through *d* show the open circuit potential for the reference material and for the weld from test rods as function of experiment duration. A time span of about 2−3 days was allowed for equilibrium to establish. The open circuit potentials observed after this time were interpreted as equilibrium values. Table 4-5 and Table 4-6 shows a compilation of equilibrium potentials for the different copper electrodes at various solution compositions. These equilibrium potentials as function of the logarithm of the copper ion concentration are shown in Figure 4-12, *a* through *d* and Figure 4-13, *a* through *d*. The straight black lines in Figures 4-12 and 4-13 are drawn with the theoretical slope from Nernst's law. E_0 is estimated by visual fit of the line to the datapoints giving higher weight to points at higher concentrations where the possible influence from other reactions (O_2) is expected to be lower.
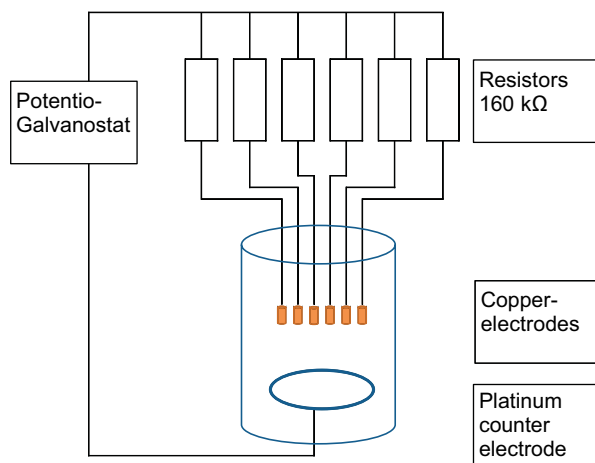
Figure 4-9. Illustration of the setup used to forcibly corrode several copper electrodes simultaneously to the same average depth.

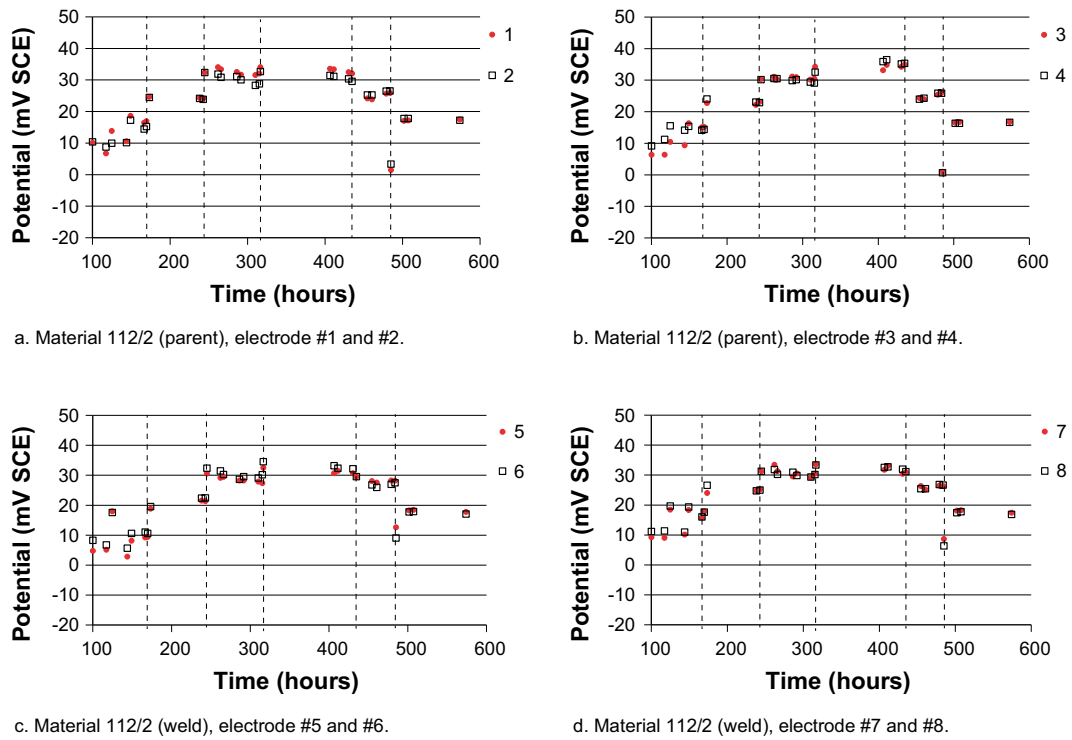## 4.4.1 Equilibrium potentials for the copper materials

a. Material 112/2 (parent), electrode #1 and #2.

b. Material 112/2 (parent), electrode #3 and #4.

c. Material 112/2 (weld), electrode #5 and #6.

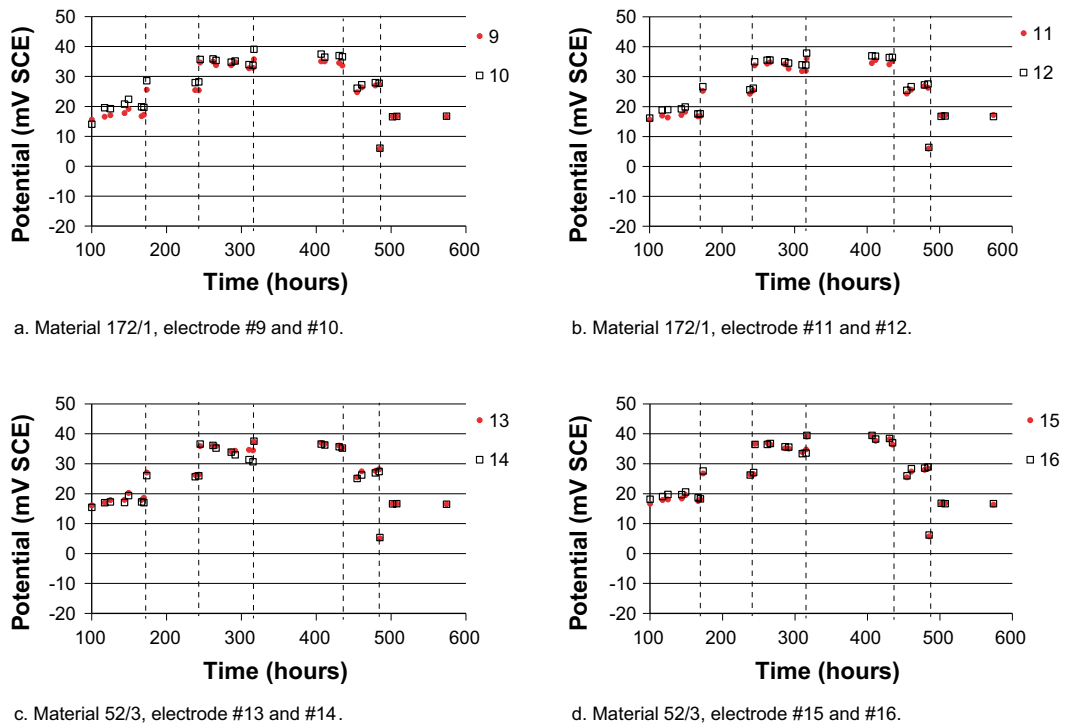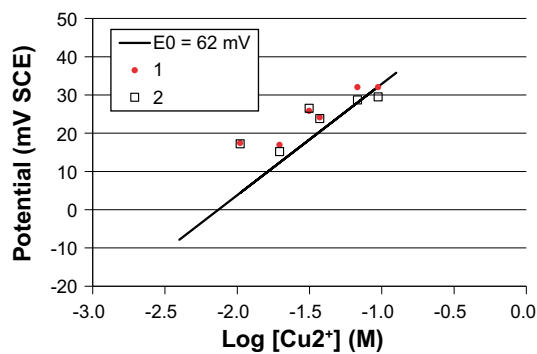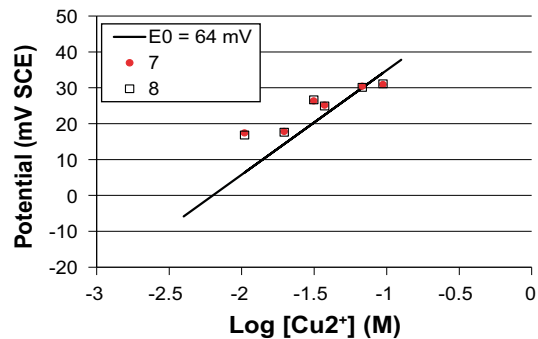d. Material 112/2 (weld), electrode #7 and #8.

Figure 4-10. *Open circuit potentials for copper electrodes #1–8 as function of experiment duration. The vertical dashed lines indicate times when the copper content in the solution was increased by the addition of a copper rich stock solution or decreased by dilution.*

a. Material 172/1, electrode #9 and #10.

b. Material 172/1, electrode #11 and #12.

c. Material 52/3, electrode #13 and #14.

d. Material 52/3, electrode #15 and #16.

Figure 4-11. *Open circuit potentials for copper electrodes #9–16 as function of experiment duration. The vertical dashed lines indicate times when the copper content in the solution was increased by the addition of a copper rich stock solution or decreased by dilution.*

Table 4-5. Electrode potentials (mV SCE) interpreted as equilibrium potentials for the different electrodes (#1–8).

Time (Hours)	[Cu²⁺] (M)	Electrode ID number							
		1	2	3	4	5	6	7	8
169	0.020	16.9	15.2	15.1	14.3	9.4	10.5	17.8	17.6
243	0.037	24.1	23.8	23.1	22.8	21.3	22.4	25.1	24.9
315	0.068	32.0	28.7	30.4	29.0	27.3	30.1	30.4	30.1
435	0.094	32.0	29.5	34.9	35.3	29.4	29.5	30.9	31.1
484	0.031	25.8	26.5	25.9	25.8	28.1	27.4	26.3	26.6
574	0.010	17.4	17.2	16.7	16.6	17.7	17.0	17.4	16.8

Table 4-6. Electrode potentials (mV SCE) interpreted as equilibrium potentials for the different electrodes (#9–16).

Time (Hours)	[Cu²⁺] (M)	Electrode ID number							
		9	10	11	12	13	14	15	16
169	0.020	17.1	19.6	16.7	17.6	18.6	16.9	18.0	18.2
243	0.037	25.3	28.1	25.3	26.1	26.3	25.9	26.4	27.0
315	0.068	32.8	33.7	31.9	33.8	34.4	30.6	34.7	33.5
435	0.094	33.6	36.5	35.2	36.4	35.2	35.2	36.3	37.0
484	0.031	27.3	27.7	26.2	27.5	28.1	27.3	28.3	28.9
574	0.010	16.6	16.7	17.1	16.6	16.4	16.4	16.3	16.6

a. Material 112/2 (parent), electrode #1 and #2.
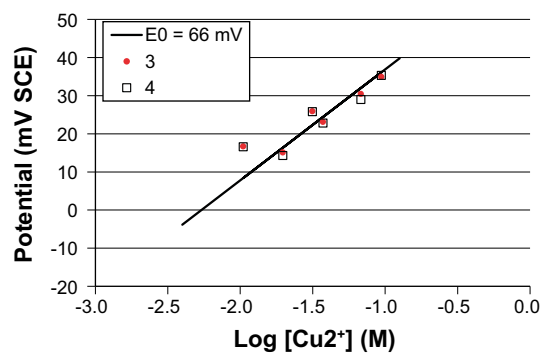
b. Material 112/2 (parent), electrode #3 and #4.
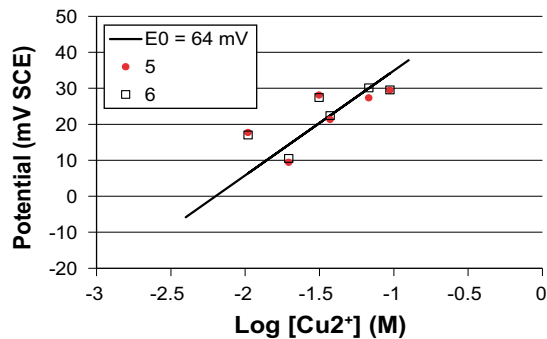
c. Material 112/2 (weld), electrode #5 and #6.

d. Material 112/2 (weld), electrode #7 and #8.

Figure 4-12. Equilibrium potentials for copper material 112/2 (weld and parent material) as function of the logarithm of the copper ion concentration. The solid lines have the theoretical slope of 29.1 mV per decade. The legend in each graph shows the value of the estimated E_0.
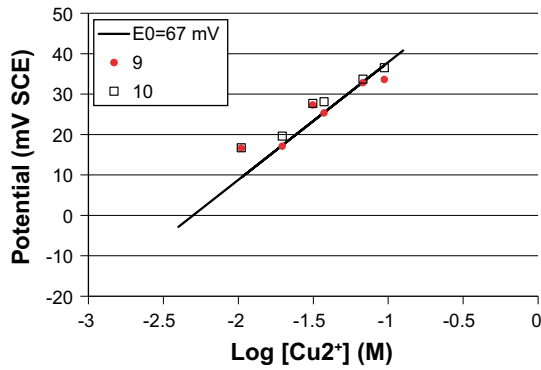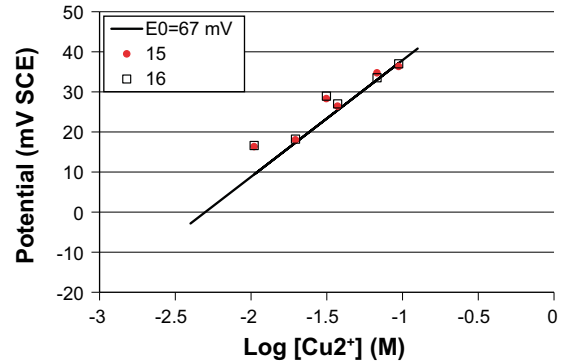
a. Material 172/1, electrode #9 and #10.
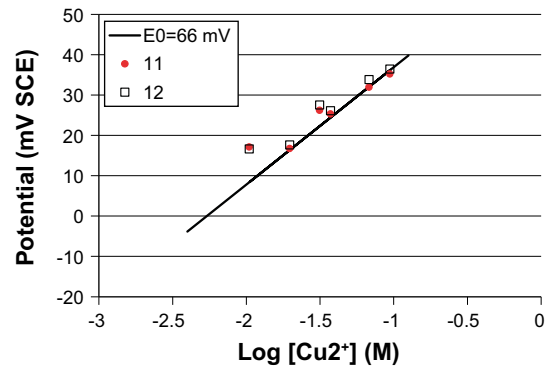
b. Material 172/1, electrode #11 and #12.
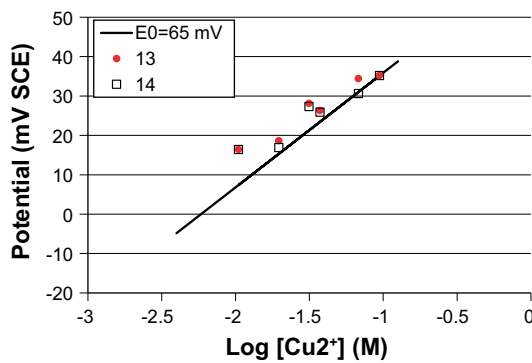
c. Material 52/3, electrode #13 and #14.

d. Material 52/3, electrode #15 and #16.

Figure 4-13. *Equilibrium potentials for welds from copper material 172/1 and 52/3 as function of the logarithm of the copper ion concentration. The solid lines have the theoretical slope of 29.1 mV per decade. The legend in each graph shows the value of the estimated E_0.*

4.4.2 Surface morphology after forced corrosion

After forced corrosion for 192 hours to a calculated average depth of attack of 0.1 mm, the electrodes were studied by confocal microscopy.

Figure 4-14 and Figure 4-17 show optical images of a small part of the electrode surface (2.6×2.6 mm) for the parent material from the lid. Figure 4-14 and Figure 4-18 show depth profiles of the area. The images are colour coded after the local depth. The closest objects (peaks) are coded red and the most distant (deepest) parts of the surface are coded blue. Figure 4-16 and Figure 4-19 show depth profiles along three selected lines across the corroded surface.

Figure 4-20 through Figure 4-25 show corresponding results for the weld labelled 112/2, advancing and reversing weld direction, respectively. Figure 4-26 through Figure 4-31 show corresponding results for the weld labelled 172/1 and Figure 4-32 through Figure 4-37 show results for the weld labelled 52/3. Figure 4-38 summarises the root mean square (RMS) roughness of the measured line profiles as a function of initial oxide thickness.

Figure 4-14. *Parent material (not weld) from copper sample 112/2. The imaged size is 2.6 × 2.6 mm.*
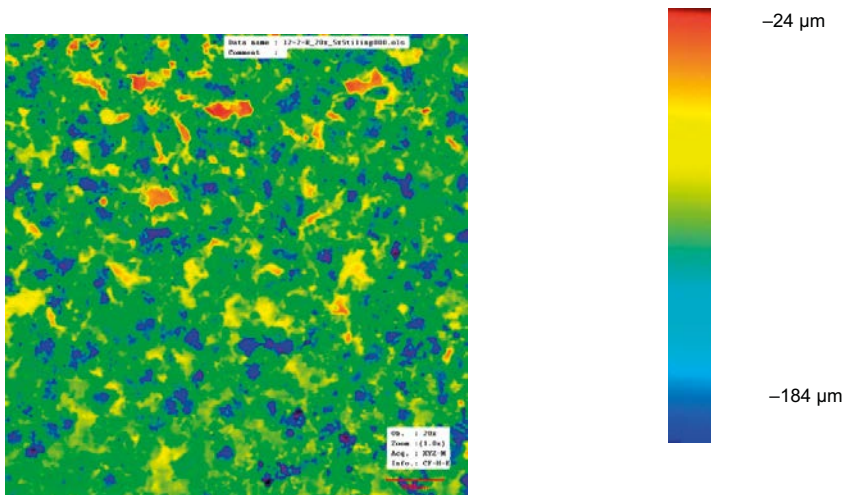
Figure 4-15. *Parent material (not weld) from copper sample 112/2. The imaged size is 2.6 × 2.6 mm.*
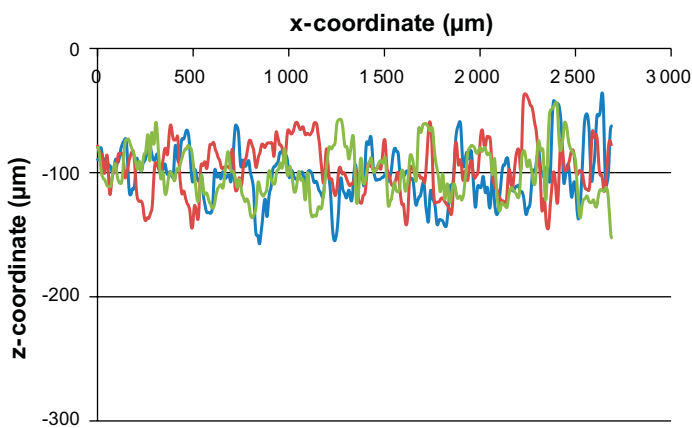

Figure 4-16. *Depth profile from the original surface of a part of the copper surface after forced corrosion to an average depth of 0.1 mm. The different lines represent different parallel lines across the surface in Figure 4-14. Parent material from sample 112/2.*
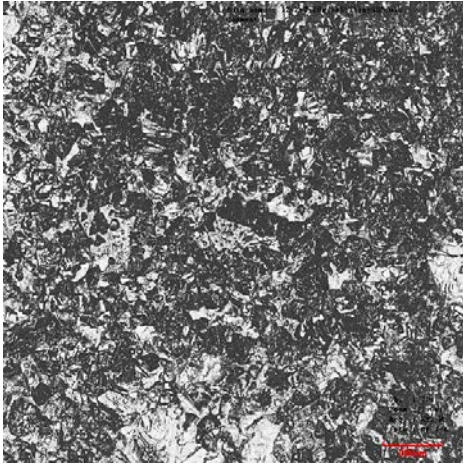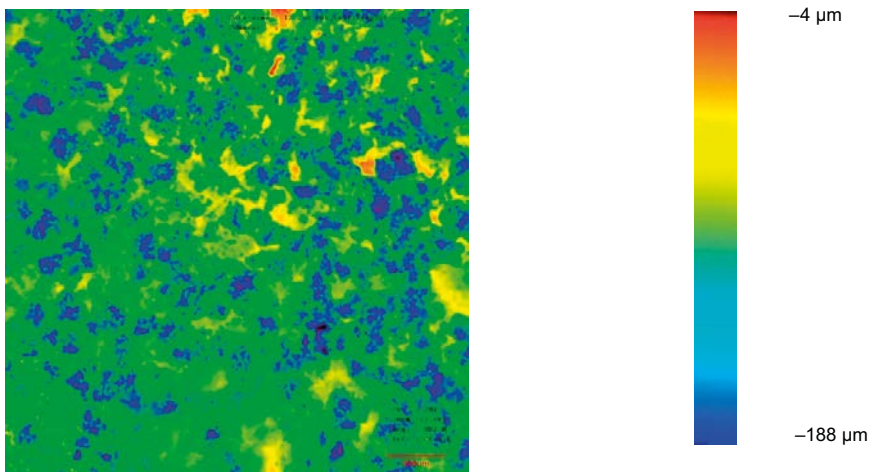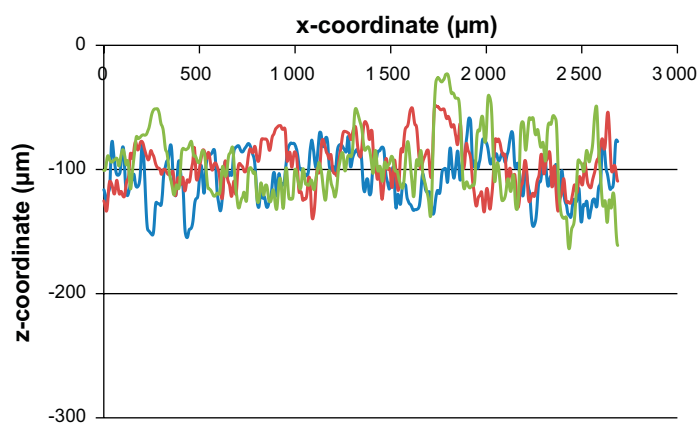
Figure 4-17. *Parent material (not weld) from copper sample 112/2. The imaged size is 2.6 × 2.6 mm.*

Figure 4-18. *Parent material (not weld) from copper sample 112/2. The imaged size is 2.6 × 2.6 mm.*

Figure 4-19. *Depth profile from the original surface of a part of the copper surface after forced corrosion to an average depth of 0.1 mm. The different lines represent different parallel lines across the surface in Figure Figure 4-18. Parent material from sample 112/2.*
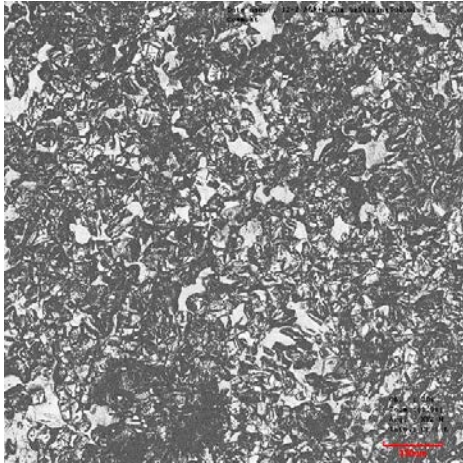
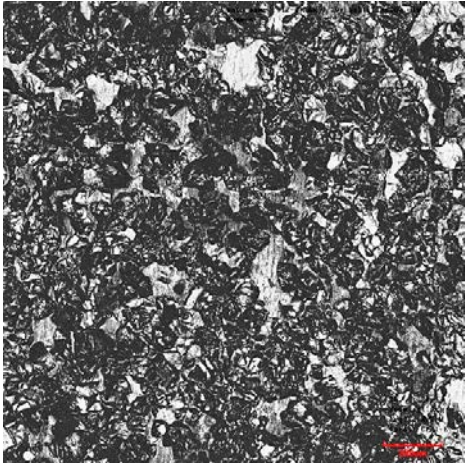**Figure 4-20.** *Weld (advancing) on copper material 112/2. The imaged size is 2.6 × 2.6 mm.*
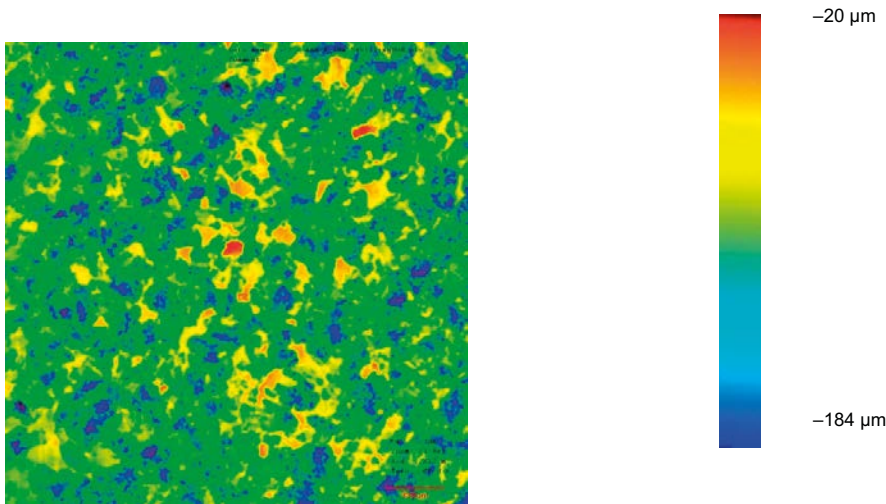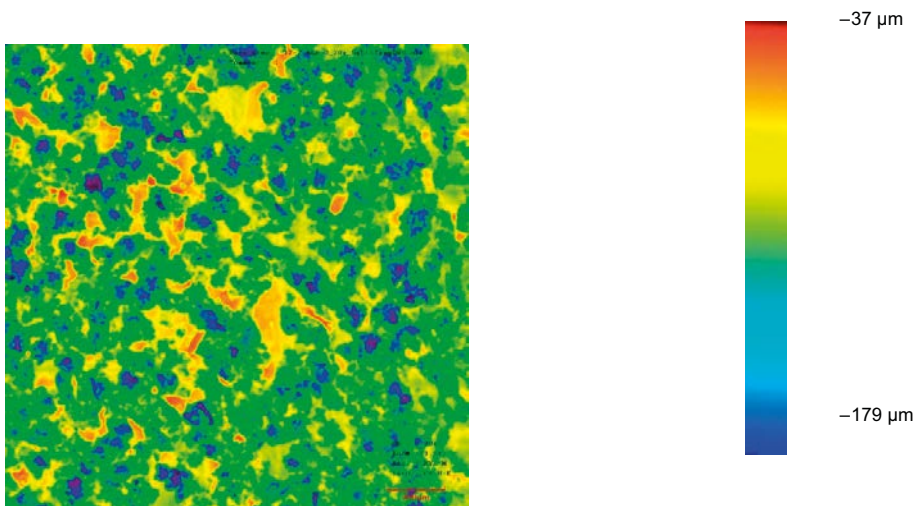

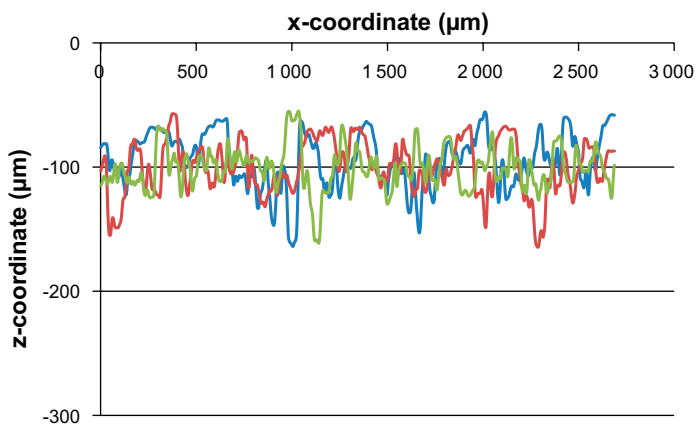**Figure 4-21.** *Weld (advancing) on copper material 112/2. The imaged size is 2.6 × 2.6 mm.*
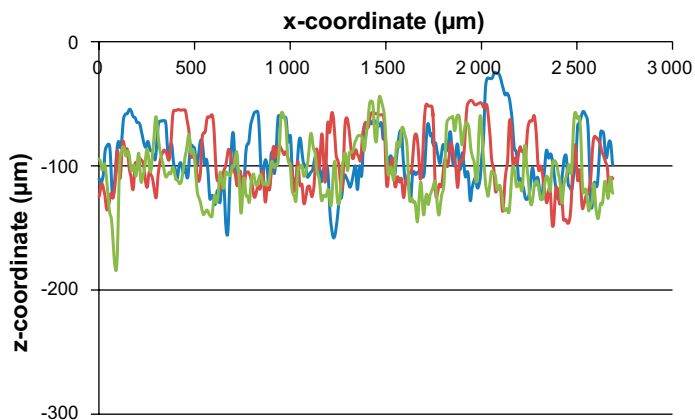
Figure 4-22. *Depth profile from the original surface of a part of the copper surface after forced corrosion to an average depth of 0.1 mm. The different lines represent different parallel lines across the surface in Figure 4-21. Weld (advancing) material from sample 112/2.*

Figure 4-23. *Weld (retreating) on copper material 112/2. The imaged size is 2.6 × 2.6 mm.*

Figure 4-24. *Weld (retreating) on copper material 112/2. The imaged size is 2.6 × 2.6 mm.*

Figure 4-25. *Depth profile from the original surface of a part of the copper surface after forced corrosion to an average depth of 0.1 mm. The different lines represent different parallel lines across the surface in Figure 4-24. Weld (retreating) material from sample 112/2.*
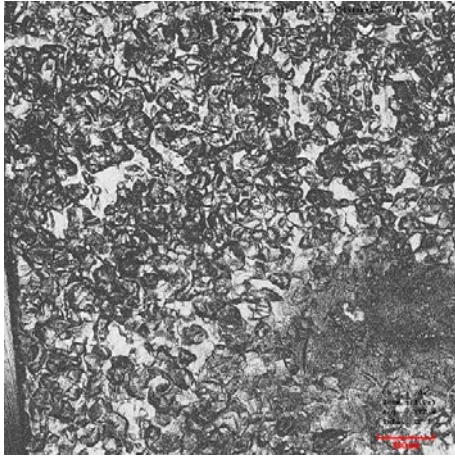
Figure 4-26. Weld (advancing) on copper material 172/1. The imaged size is 2.6 × 2.6 mm. The darker region in the lower right corner is from deposits formed during the corrosion process (likely due to local saturation of $Cu_x(OH)_ySO_4$), inhibiting uniform corrosion of that region.
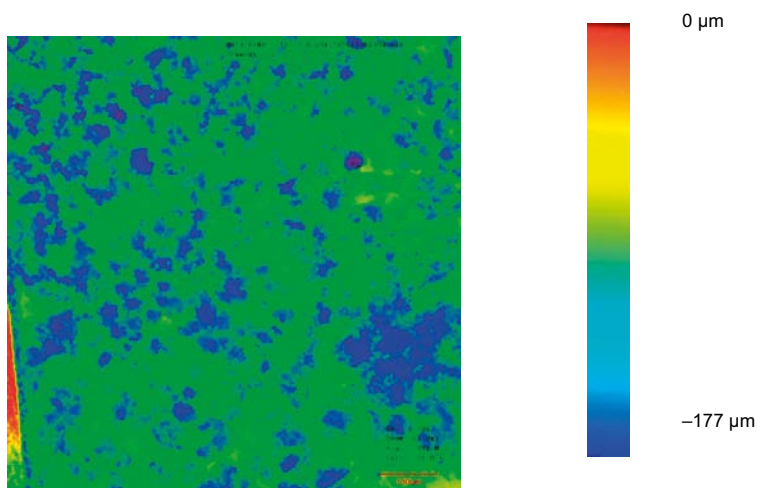

Figure 4-27. Weld (advancing) on copper material 172/1. The imaged size is 2.6 × 2.6 mm. Red colouring in the lower left corner is due to overlap with the epoxy during the measurements, which is at an elevated level in relation to the corroded copper electrode.
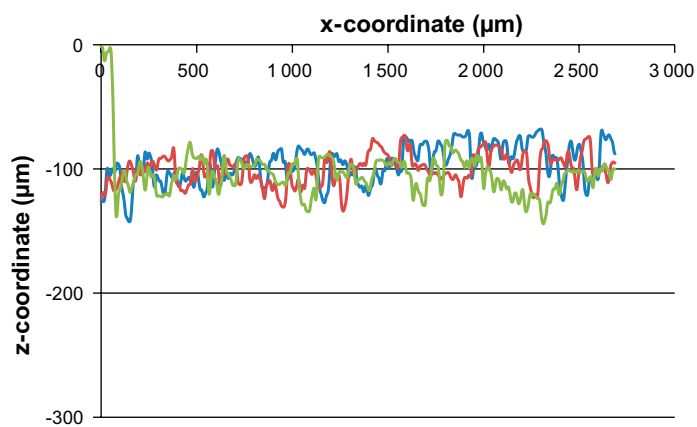

Figure 4-28. Depth profile from the original surface of a part of the copper surface after forced corrosion to an average depth of 0.1 mm. The different lines represent different parallel lines across the surface in Figure 4-27. Weld (advancing) material from sample 172/1. The peak in height, at x-coordinate zero, for the green coloured line is due to overlap with the epoxy during the measurements, which is at an elevated level in relation to the corroded copper electrode.
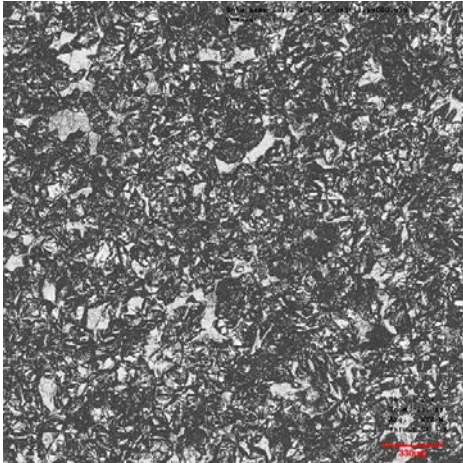
Figure 4-29. *Weld (retreating) on copper material 172/1. The imaged size is 2.6 × 2.6 mm.*
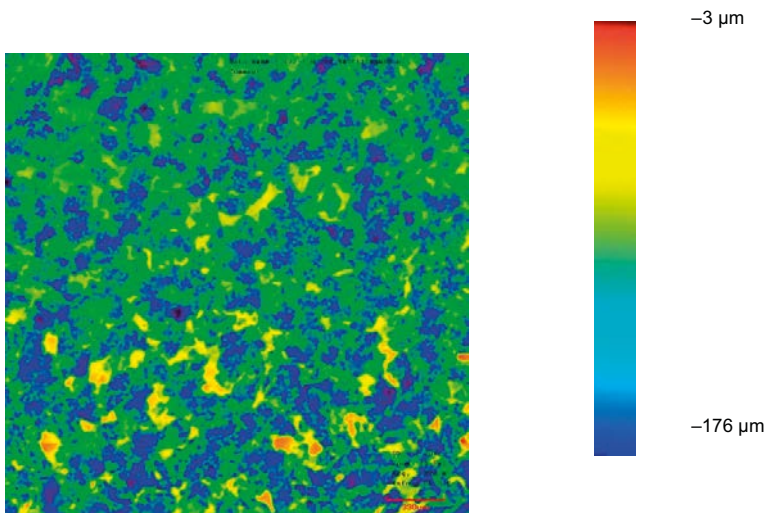

Figure 4-30. *Weld (retreating) on copper material 172/1. The imaged size is 2.6 × 2.6 mm.*
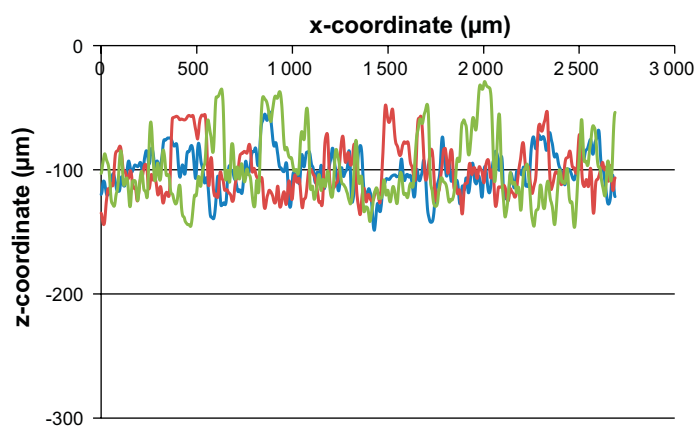

Figure 4-31. *Depth profile from the original surface of a part of the copper surface after forced corrosion to an average depth of 0.1 mm. The different lines represent different parallel lines across the surface in Figure 4-30. Weld (retreating) material from sample 172/1.*
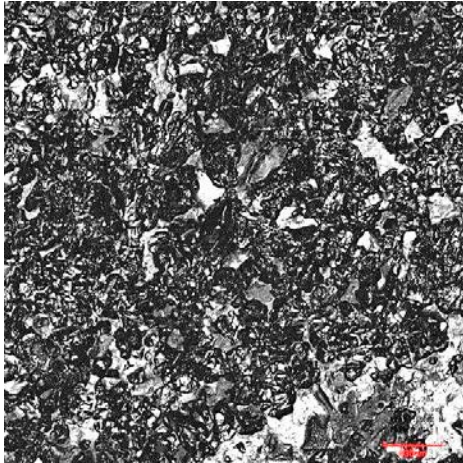
Figure 4-32. *Weld (advancing) on copper material 52/3. The imaged size is 2.6 × 2.6 mm.*

Figure 4-33. *Weld (advancing) on copper material 52/3. The imaged size is 2.6 × 2.6 mm.*

Figure 4-34. *Depth profile from the original surface of a part of the copper surface after forced corrosion to an average depth of 0.1 mm. The different lines represent different parallel lines across the surface in Figure 4-33. Weld (advancing) material from sample 52/3.*

Figure 4-35. *Weld (retreating) on copper material 52/3. The imaged size is 2.6 × 2.6 mm.*
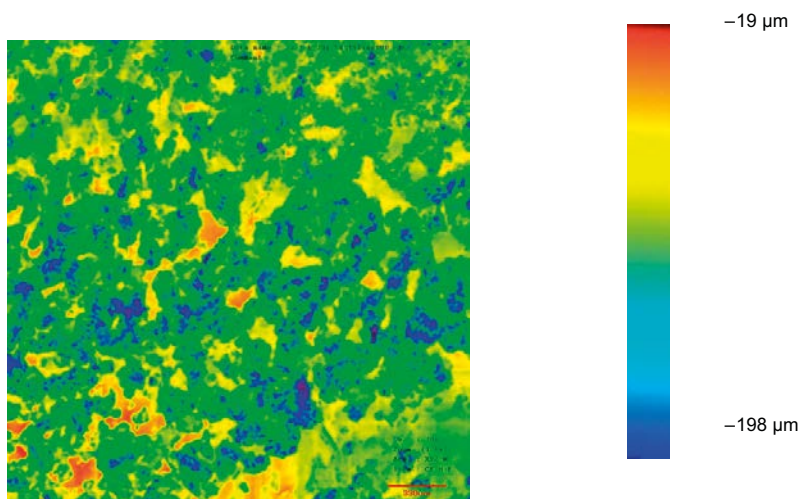

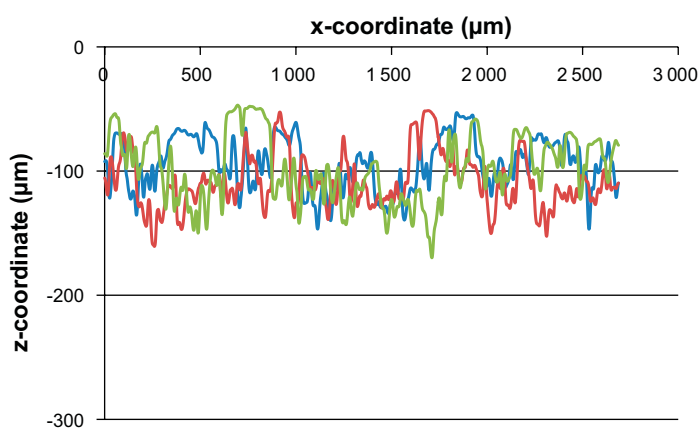**Figure 4-36.** *Weld (retreating) on copper material 52/3. The imaged size is 2.6 × 2.6 mm.*

Figure 4-37. *Depth profile from the original surface of a part of the copper surface after forced corrosion to an average depth of 0.1 mm. The different lines represent different parallel lines across the surface in Figure 4-36. Weld (retreating) material from sample 52/3*
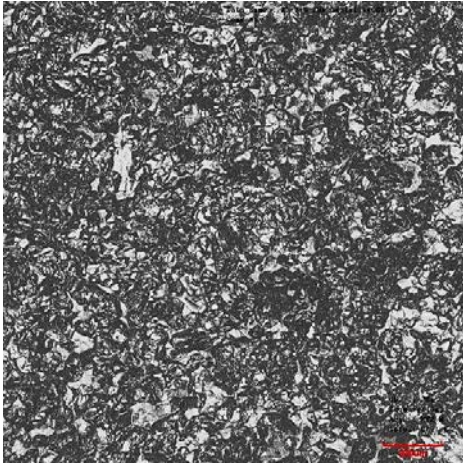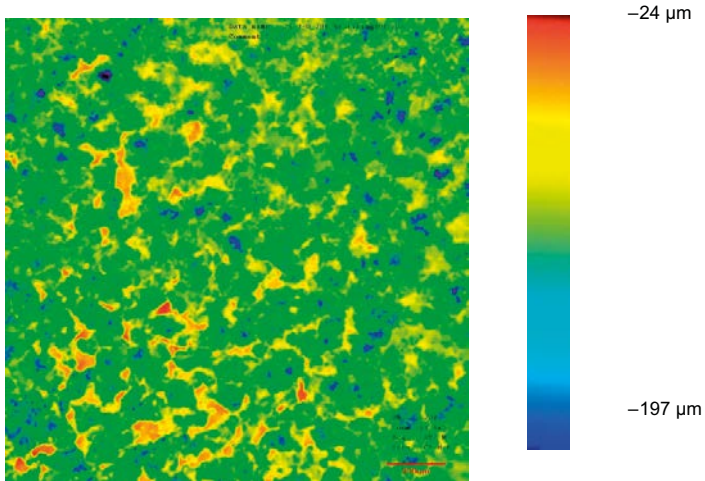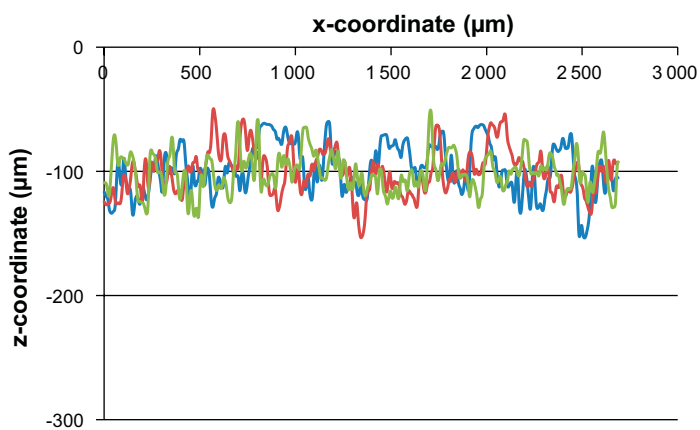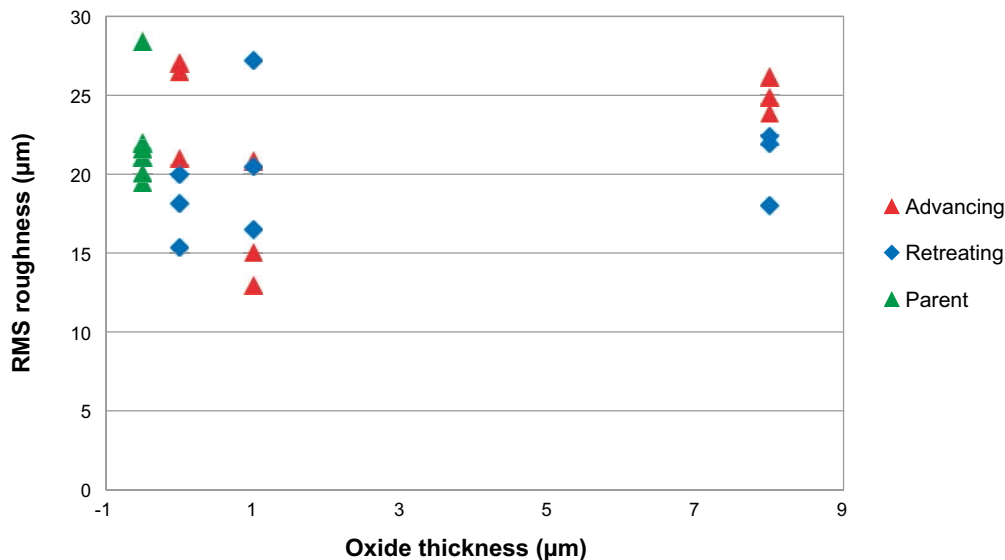
Figure 4-38. *The RMS roughness for the profiles shown in Figure 4-19, Figure 4-22, Figure 4-25, Figure 4-28, Figure 4-31, Figure 4-34 and Figure 4-37as a function of the oxide thickness. An arbitrary x-axis position of −0.5 μm have been used for the parent material.*

4.5 Discussion of corrosion properties

4.5.1 Dissolution of oxides

The dissolution rate of a continuous band of oxide, $Cu_2O(s)$ was studied theoretically, partly by analytical expressions and partly by finite element modeling. The results show that if there is a continuous band of oxide from the outer surface of the copper canister to the inner surface, the oxide in this band could dissolve in relatively short times. Table 4-3 shows that for conditions where the copper ion concentration is negligible at the outer canister surface, 1.0 M chloride and 10 mM total carbonate at pH 7 would give a maximum dissolution rate corresponding to perforation of the 5 cm canister wall in approximately 2 300 years. If the oxide band is wedge shaped so that it is wider at the outer surface of the canister than at the inner surface, the time to perforation could be about half as long as in the case of a linear band, see Figure 4-6.

The dissolution rate of oxide bands has a strong dependence on the chloride concentration in the water. Because the dominating form of the dissolved copper is $CuCl_2^-$, the solubility of the oxide increases approximately with the square of the chloride concentration. But because the oxide dissolution increases the local pH, the buffering capacity influences the solubility and thereby the maximum rate of dissolution. 1.0 M chloride and 10 mM total carbonate at pH 7 limits the local pH at the point of oxide dissolution to about 7.4 whereas 1 mM total carbonate at pH 7 gives a local pH at the point of oxide dissolution of about 8.1 with a much lower dissolution rate. The results from the analytical expressions in Section 4.1 agree well with the results from the numerical model in Section 4.2, for cases where comparison is possible.

The origin of the oxide bands would probably be flakes of surface oxide from the canister present before welding and introduced in the weld material during the friction stir weld operation. It seems very unlikely that the thickness of the oxide streaks would become larger than the thickness of the initial flake of oxide from the copper canister.

The thickness of the oxide band is likely to be of importance for the dissolution process. The analytical treatment as well as the numerical model considers a situation where there is liquid water in the gap so that there is an aqueous volume where copper ions can diffuse. If the bentonite is too dry to release liquid water this growth mode would not be operative. Possibly, fine grains of bentonite could enter the gap and enable ionic transport of copper. For thin oxide bands, corresponding to thin initial oxide layers, it is difficult to see how grains of bentonite could enter deep into the resulting narrow gap without liquid water.

4.5.2   Corrosion properties of welds

Figure 4-12a and b, show measured equilibrium potentials for the parent material from the lid. The estimated normal potentials differ by about 4 mV. The average value of 64 mV will serve as a measure of the properties of the parent material with which the properties of the welds can be compared. The difference of 4 mV in experimental results for the parent material will serve as a measure of the experimental spread in results.

Figure 4-12c and d and Figure 4-13 show that the apparent nobility of the welded materials for all three welds does not significantly differ from that of the parent material. This is in agreement with the results from Gubner and Andersson (2007) who studied the galvanic effects at open circuit potentials in aerated and deaerated solutions of 0.5 M NaCl at pH 6.5 but without addition of copper ions.

When forced to corrode to an average depth of 0.1 mm, the whole surface is corroded for all materials studied. No parts remain of the original surface. No part of any of the surfaces studied had corroded to more than double the average depth. The maximum depth of attack found is about 0.2 mm. No systematic difference between the welds and the parent material can be seen in the topography of the corroded surfaces, which is also verified by Figure 4-38. The slightly more even appearance of the surface in Figure 4-26 and Figure 4-27 is probably due to the precipitation of the solid corrosion product. It is likely that this compound, which was found to contain copper and sulfate, had formed locally because of local supersaturation caused by non-uniform convection. Thus the slightly more even appearance of the surface is probably related to the location in the electrochemical cell during forced corrosion and not related to any properties of the copper metal.

The weld material here was taken at some distance from the center of the weld, Figure 4-7. Bands have been observed in welds and then located close to the center of the weld, Figure 4-8. The present study cannot exclude the possibility that the corrosions properties at these bands differ from those of the parent material but at the distance from the center line where the test pieces where cut, the corrosion properties of the weld material cannot be distinguished from those of the parent material.

5 Summary and conclusions

5.1 Mechanical testing

A systematic study on the effect of initial oxide thickness prior to welding on the deformation behaviour of Cu-OFP has been made. The test methods consisted of metallography, hot tensile and creep testing. New specimen geometry with a 4 mm gauge length was designed for the mechanical tests in order to ensure that the area with an oxide streak would experience the highest load. For specimen preparation, metallographic methods were used to position the oxide streak perpendicular to the loading axis. In addition, tensile and creep tests were made for a reference material without a weld and cross-tension specimens using conventional creep specimen geometry.

The main conclusions of this study can be summarised as follows:

- Streaks of embedded oxide particles are clearly visible in macro etched specimens with initial oxide layer thickness equal to about 1 µm and higher. With an initial oxide layer thickness of 0.1 µm, no oxide streaks were visible.

- The hot tensile tests showed clearly less ductile behaviour for the specimens with initial oxide thickness of about 1 µm or higher.

- The ultimate tensile strength values for the specimens with visible oxide streaks (1 µm or higher) and ones with lower oxide content (0.1 µm and lower) are approximately equal. However, slightly lower values are measured for cross-welded specimens.

- Failure in the cross-weld tensile and creep test specimens of segment 3 with 0 µm initial oxide layer thickness occurs in the heat affected zone (HAZ). Also another area with necking can be identified along the specimen gauge length.

- The cross-weld tensile test specimens of segments 1 (~1 µm) and 2 (6–11 µm) show deformation behaviour similar to segment 3 at 75 °C but at 175 °C the ductility is clearly reduced.

- The creep tests also show significantly lower ductility for the specimens with initial oxide layer thickness of 1 µm or higher.

- The SEM-studies show that the fracture surfaces of the specimens with initial oxide layer thickness 1 µm or higher contain large amounts of oxide particles.

- The tensile and creep ductility of segments 3 (0 µm) and 6 (0.1 µm) are comparable with the reference specimen without a weld.

5.2 Corrosion

In the case of a continuous oxide streak extending through the 5 cm thick weld, chemical dissolution of the oxide (Cu_2O) can be relatively fast provided there is liquid water in contact with the canister. High chloride concentrations and high carbonate concentrations in the water increase the rate of dissolution. The worst case studied here, 1.0 M chloride, 10 mM carbonate at pH 7.0 with a wedge shaped continuous oxide band could perforate a 5 cm thick weld in little more than 1 000 years.

Even in the absence of a continuous oxide streak it is possible that small oxide particles become dispersed in copper metal during the welding process. The presence of oxide in the metal could conceivably affect the corrosion behavior of the metal. Electrochemical studies of metallic copper from the weld do not reveal any significant differences from the parent material taken from the lid of a welded canister. The apparent nobility of copper weld is not significantly different from that of the parent material. When forced to corrode to an average depth of 0.1 mm, the morphology of the surfaces from the weld is also similar to that of the parent material.

5.3   Overall Conclusions

The theoretical corrosion calculations as well as the experimental creep and tensile testing showed that embedded copper oxides can have a detrimental effect on the performance. If the oxide thickness is below 0.1 µm the creep and tensile ductility are comparable to the reference material. The derived minimum true strain from Jonsson et al. (2018) of 160 %, for a triaxiality T=0.33, is fulfilled for all tests with an oxide thickness of 0.1 µm and below. A true strain of 160 % corresponds to an area reduction of 80 % according to Equation 3-1 in Jonsson et al. (2018). For oxide thicknesses of 0.1 µm and below oxides are not detected by metallographic examinations. This indicates that also the corrosion properties (with respect to oxide inclusions) should be similar to the base material of the canister.

The absence of oxide particles cannot be directly inspected in a final production weld. Therefore it is necessary that the welding process is controlled in such a way that no oxides appear. This can be done by monitoring the oxygen level in the gas shield during welding and following a welding procedure for the welding operations. The procedure is practically demonstrated (for example with extraction of metallographic specimens) during qualification of the welding process.

Using these investigations a process window can be summarized in the following way. In order not to affect the tensile, creep or corrosion properties the welding has to be conducted in an inert atmosphere that produces a weld free from oxides according to, for example, ASTM B577-10 Standard Test Methods for Detection of Cuprous Oxide (Hydrogen Embrittlement Susceptibility) in Copper method B. The maximum allowed oxygen level in the gas shield will depend on the chosen weld temperature and possibly the joint geometry. The maximum allowed oxygen level will be defined during qualification of the welding process.

For the currently used configuration a gas level can be estimated using previous calculations (Björck 2015) which showed that an oxygen level of 100 at-ppm yielded a total oxide thickness below 50 nm which is fulfils the seen limit of 0.1 µm. This level can be maintained in the gas shield presented in a previous report (Björck et al. 2017).

Acknowledgment

References

SKB's (Svensk Kärnbränslehantering AB) publications can be found at www.skb.com/publications.
SKBdoc documents will be submitted upon request to document@skb.se.
Posiva's publications can be found at http://posiva.fi/en/databank.

Andersson H C M, Seitisleam F, Sandström R, 2007. Creep testing and creep loading experiments on friction stir welds in copper at 75 °C. SKB TR-07-08, Svensk Kärnbränslehantering AB.

Andersson-Östling H C M, Sandström R, 2011. Effect of loading rate on creep of phosphorous doped copper. SKB TR-11-09, Svensk Kärnbränslehantering AB.

ASTM, 2016a. ASTM B577-16: Standard test methods for the detection of cuprous oxide (hydrogen embrittlement susceptibility) in copper. West Conshohocken, PA: ASTM International.

ASTM, 2016b. ASTM F68-16: Standard specification for oxygen-free copper in wrought forms for electron devices. West Conshohocken, PA: ASTM International.

Björck M, 2015. Estimation of oxide growth on joint surfaces during FSW. SKBdoc 1402837 ver 1.0, Svensk Kärnbränslehantering AB.

Björck M, Elger R, 2013. Oxidation kinetics of copper at reduced oxygen partial pressures. SKBdoc 1410172 ver 1.0, Svensk Kärnbränslehantering AB.

Björck M, Tigerström M, Cederqvist L, Pehkonen H, Vuori L, Lahtonen K, Valden M, Purhonen T, 2017. Evaluation of a gas shield for friction stir welding of copper canisters. Posiva SKB Report 02, Posiva Oy, Svensk Kärnbränslehantering AB.

Cederqvist L, 2011. Friction stir welding of copper canisters using power and temperature control. PhD thesis. Lund University, Sweden.

Chen H-B, Yan K, Lin T, Chen S-B, Jiang C-Y, Zhao Y, 2006. The investigation of typical welding defects for 5456 aluminum alloy friction stir welds. Materials Science and Engineering A 433, 64−69.

Gubner R, Andersson U, 2007. Corrosion resistance of copper canister weld material. SKB TR-07-07, Svensk Kärnbränslehantering AB.

Högberg C-J, Karlsson O, Randelius M, Johansson A J, 2017. Surface morphology and elemental composition of copper canisters for disposal of spent nuclear fuel. SKB P-17-11, Svensk Kärnbränslehantering AB.

Jonsson M, Emilsson G, Emilsson L, 2018. Mechanical design analysis for the canister. Posiva SKB Report 04, Posiva Oy, Svensk Kärnbränslehantering AB.

Leroy P, Revil A, Coelho D, 2006. Diffusion of ionic species in bentonite. Journal of Colloid and Interface Science 296, 248−255.

Mannesson K, Andersson-Östling H C M, 2016. Stress application and the effect on creep of copper. SKB R-14-31, Svensk Kärnbränslehantering AB.

Mannesson K, Andersson-Östling H C M, Sandström R, 2013. Influence of local cold work in creep failure of phosphorous doped oxygen free copper. SKB R-13-32, Svensk Kärnbränslehantering AB.

Puigdomenech I, Taxén C, 2000. Thermodynamic data for copper. Implications for the corrosion of copper under repository conditions. SKB TR-00-13, Svensk Kärnbränslehantering AB.

Rantala J, Auerkari P, Laukkanen A, Andersson T, Saukkonen T, 2014. Material integrity of welded copper overpack. Annual report 2014. KYT2014/MICO, Research report VTT-R-00773-15, VTT Technical Research Center of Finland.

Savolainen K, 2012. Friction stir welding of copper and microstructure and properties of the welds. PhD thesis. Aalto University, Finland.

SKB, 2010. Design, production and initial state of the canister. SKB TR-10-14, Svensk Kärnbränslehantering AB.

SKB, 2011. Long-term safety for the final repository for spent nuclear fuel at Forsmark. Main report of the SR-Site project. SKB TR-11-01, Svensk Kärnbränslehantering AB.

SS-EN ISO 25239:2012. Friction stir welding – Aluminium. Stockholm: Swedish Standards Institute.

SS-EN ISO 21608:2012. Corrosion of metals and alloys – Test method for isothermal-exposure oxidation testing under high-temperature corrosion conditions for metallic materials. Stockholm: Swedish Standards Institute.

Stumm W, Morgan J, 1981. Aquatic chemistry: An introduction emphasizing chemical equilibria in natural waters. 2nd ed. New York: Wiley.

Taxén C, Sparr M, 2014. Corrosion properties of copper materials. SKB R-14-15, Svensk Kärnbränslehantering AB.

Wu R, 2011a. Processing line inclusion (PLI) and joint line hooking (JLH) in Cu-OFP friction stir weld – Part 1: Metallographic examinations. KIMAB-2011-111, Swerea KIMAB AB.

Wu R, 2011b. Processing line inclusion (PLI) and joint line hooking (JLH) in Cu-OFP friction stir weld – Part 2: Hot tensile and creep properties. KIMAB-2011-114, Swerea KIMAB AB.

Zhou C, Yang X, Luan G, 2006. Effect of oxide array on the fatigue property of friction stir welds. Scripta Materialia 54, 1515–1520.

Investigation of welded object

In order to validate the, by simulation, estimated oxide thicknesses one down travel sequence conducted without a gas shield was cut out and separated in order to determine the maximum oxide thickness occurring. Care was taken not to delaminate the oxide during sample preparation. Photographs of the samples with indicated analysis cross sections are given in Figure A-1.

The surface of the tube part displayed a thin layer of oxide, generally 0.5–1 µm. However, internal oxidation occurred down to approximately 5 µm (Figure A-3). In some instances shown in Figure A-2 and Figure A-3, the oxide layer thickness reached approximately 2.5 µm. The analysed weight percentage of oxygen was 5–8 wt-%. The oxygen content might be larger than indicated by the analysis since the thin layers analysed (in most cases below 1µm), will contain a signal from the copper matrix that reduce the oxygen signal.
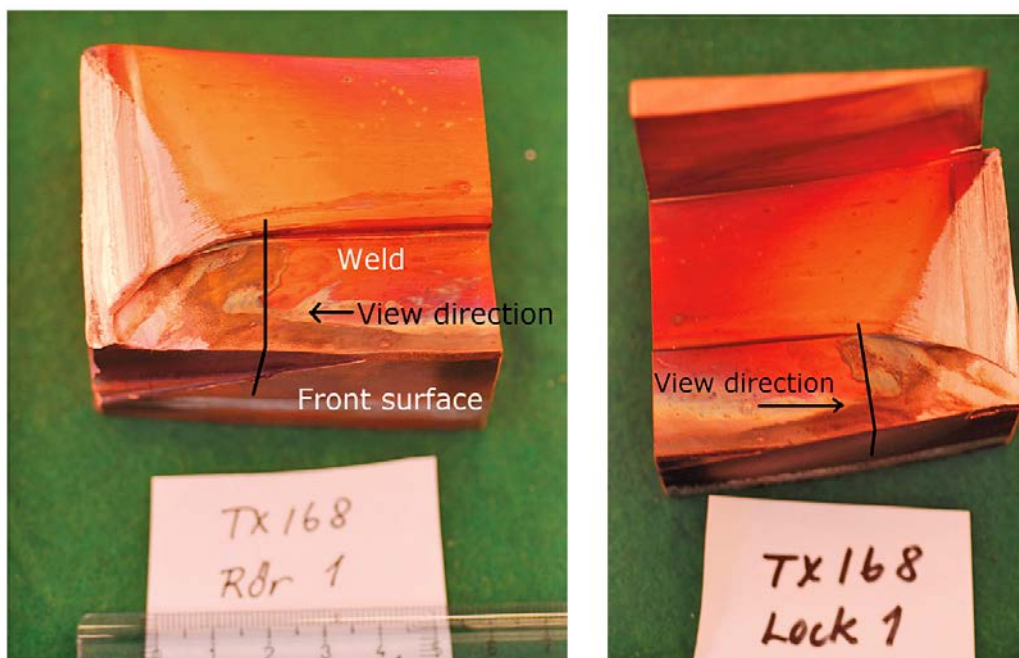

Figure A-1. Photographs of the two parts with cutting lines for the cross section analysis indicated. The view direction and denotation of SEM analysis are indicated in the image. Left: Tube part. Right: Lid part.
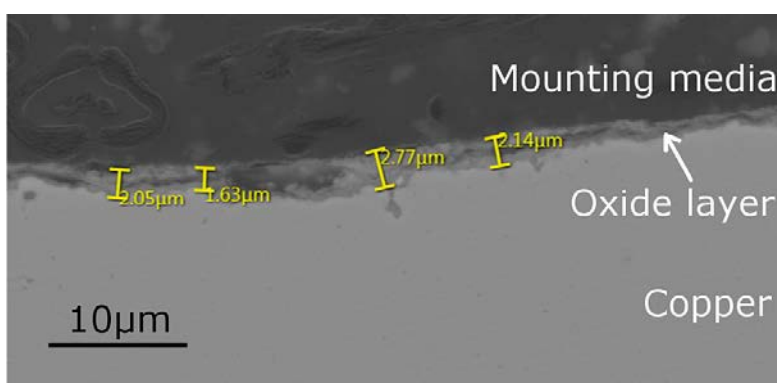

Figure A-2. Back-scattered electron image of the thickest part of the oxide, close to the front surface of the weld surface.
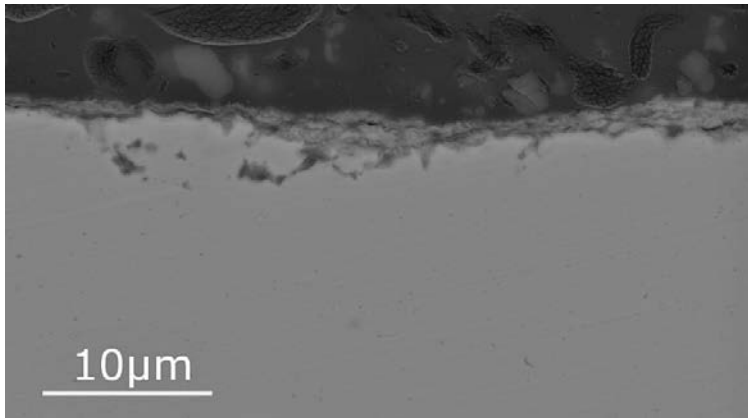
Figure A-3. Back-scattered electron image with internal oxidation in the tube's weld surface close to the front surface.
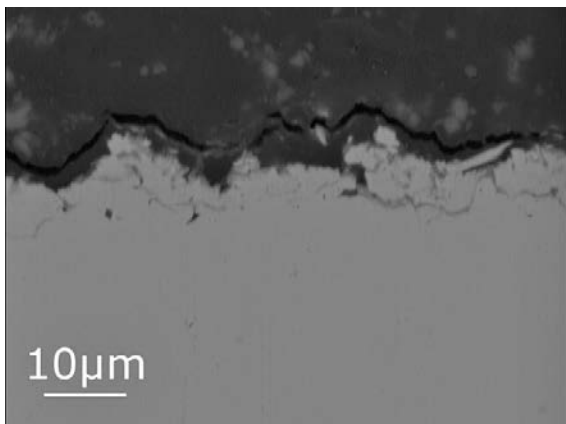

Figure A-4. Back-scattered electron image of the front surface of the weld. Internal oxidation was observed in addition to a thin oxide layer.

On the lid part, the cross section was taken as indicated in Figure A-1. The oxides observed were generally thinner, but in many cases, oxidation suggested to precede delamination was observed (Figure A-5 b) and c)). In Figure A-5 c), a thin oxide layer was observed in the bottom of the protrusions indicated in the image. Also, internal attacks as shown in Figure A-5 a) and Figure A-4 were observed in some instances. On the front surface of the sample, a thicker oxide structure shown in Figure A-6 was observed with a thickness of ~3 μm. The two layers shown in the image displayed equal oxygen/copper ratio (8 wt-% O/88 wt-% Cu). As discussed above, signal from oxygen might underestimate the content of oxygen.

The cause of the apparent internal oxidation was not investigated in this work. It could be due to the oxidation process, be due to previous machining operation as seen in corrosion experiments (Högberg et al. 2017) or from the welding process itself.

The maximum thickness of the oxide layer formed during the down travel sequence amount to 3 μm in the studied sample. This is in agreement with the simulations using a previously fitted oxidation model (Björck 2015) where the calculated oxide thickness was found to be 3 μm before the final passage. It was also seen that the maximum thickness occurs close to the front the surface of the weld and decays towards the root side of the weld. The simulated total thickness of the oxide after two passes was 4 μm on one surface. As the joint consists of two surfaces the total maximum expected thickness is 8 μm.
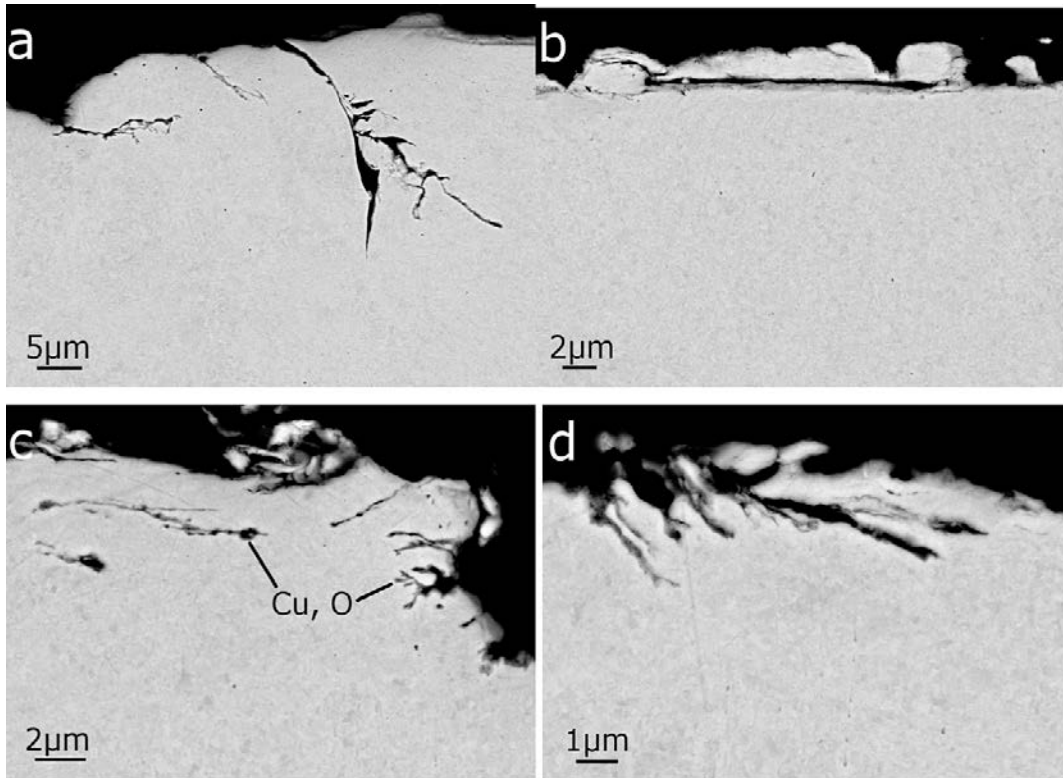
Figure A-5. *Back-scattered cross section images from the lid part of the weld. (a) Internal attack without oxides (b) Delaminated zone with oxide on the metal surface (c) Example of protrusions rich in oxygen as indicated (d) Example of internal oxidation. Observe the different magnifications.*
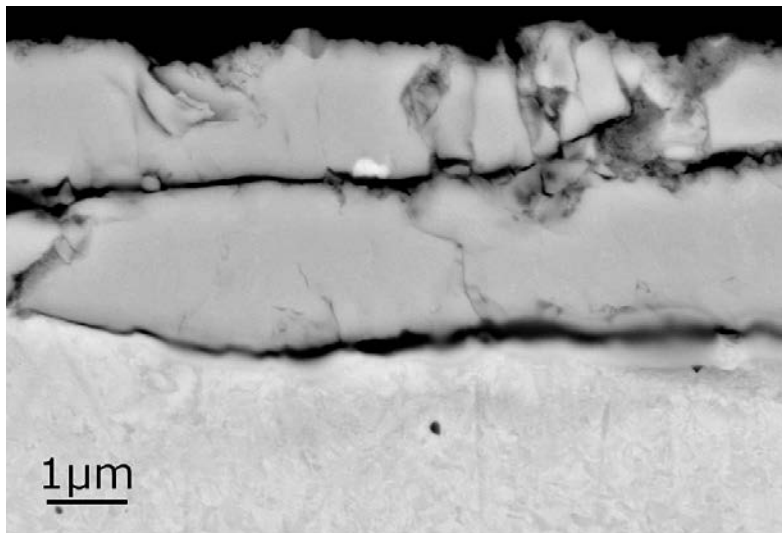

Figure A-6. *Back-scattered electron image of the front of the lid part of the weld.*

A CO-OPERATION REPORT BETWEEN SVENSK KÄRNBRÄNSLEHANTERING AB AND POSIVA OY

SKB's and Posiva's programmes both aim at the disposal of spent nuclear fuel based on the KBS-3 concept. Formal cooperation between the companies has been in effect since 2001. In 2014 the companies agreed on extended cooperation where SKB and Posiva share the vision "Operating optimised facilities in 2030". To further enhance the cooperation, Posiva and SKB started a series of joint reports in 2016, which includes this report.